



University of
BRISTOL

School of Chemistry

Characterising the Thermionic Behaviour
of Hydrogen Terminated, n- and p-doped
Diamond Films

by

Jonas Hiemstra

**This thesis is submitted in partial fulfilment of the requirements for the Honours Degree of
MSci Chemical Physics at the University of Bristol**

Submitted April 2024

Supervisors:

First assessor: Professor Paul May
Second assessor: Professor Neil Fox
Physical and Theoretical Chemistry

Word Count: 19,685
(excluding tables, figure captions, references, and appendix)

Statement of Limiting Factors

The initial aims of this project were to explore the effects of terminating the surfaces of doped diamond samples with various species. The hydrogen terminated samples that became the focus of this study were intended only to be confirmation that the samples deposited exhibited expected properties. The expected progression of the research intended to study samples that had been terminated with scandium for thermionic emission to supplement research completed by Zulkharnay. Another intended aim was to study nitrogen-based terminations using a nitrogen plasma in the front microwave reactor. Potential ideas were to adjust the temperatures, pressures, and nitrogen flow rates to analyse how these variables affect the type of N-based termination species formed. As is stated in the theory section of this study, an issue with nitrogen-based terminations is that various types often coexist resulting in uneven work functions and electron affinities. Therefore, if research could have discerned conditions that preferentially resulted in a majority of one type of N-termination, then that would be incredibly beneficial to the field.

However, these initial aims were not met as the reactor used to deposit the nitrogen-doped sample was not useable until late-November when the first NDD sample could be deposited. Additionally, the laser-etching system was not in working order, or in the lab, to etch the grating into the reverse side of the samples to prepare them for thermionic testing. Once the laser system was useable, the thermionic emission conversion simulator kit was block-booked by another faculty, which resulted in the breakage of a vital quartz component which was not repaired until mid-February.

SIMS spectra were also intended to be taken; however, this equipment also did not work until the final week of the project when thermionic testing was being completed. It could not have been taken before thermionic testing as SIMS is destructive to the sample and would alter the results collected.

The final challenge that could not be overcome was the delamination of the N-doped sample in the final two weeks of lab time. Another sample was deposited, however, the laser etching system then broke again (issues with the chiller), meaning that the sample could not be prepared for thermionic analysis in the time available.

Abstract

Diamond is an exciting material that offers possibilities for practical use in TEC devices as it can exhibit a so-called negative electron affinity (NEA) surface, which lowers the barrier to the generation of thermionic currents. This study aimed to examine hydrogen-terminated, doped diamond systems for their thermionic emission characteristics. In order to achieve this, the surfaces of a range of samples were characterised using Raman spectroscopy and scanning electron microscopy, before thermionic analysis was completed.

The samples used in this study were undoped diamond, boron-doped diamond (BDD), and nitrogen-doped diamond (NDD), all prepared and grown in the laboratory in Bristol using CVD. Additionally, three phosphorus-doped diamond samples (PDD) with various dopant concentrations, as supplied by the Institute of Physics of the Czech Academy of Sciences, were also analysed. Each grown sample was manually abraded, but all the samples had the backside laser-etched with a narrow grating in order to prepare for thermionic analysis. Prior to thermionic testing, each sample was freshly H-terminated to ensure full surface coverage.

Grain size analysis on SEM images found microdiamond character for the undoped sample, which exhibited a mean grain diameter of $0.2225 \pm 0.0167 \mu\text{m}$. The boron-doped sample was characterised as a nanodiamond material with a mean grain size of $0.094 \pm 0.0044 \mu\text{m}$. All the n-type samples (NDD and PDD, the latter with different concentrations) had an ultrananocrystalline (UNC) grain size with a mean grain diameter of less than $0.001 \mu\text{m}$. Generally, the thermionic emission characteristics of the UNC materials showed the best performance relative to undoped and boron-doped samples, which could initially be attributed to an increased number of grain boundaries.

Six characteristic Raman spectral peaks were observed for the samples. The expected diamond and graphite peaks were found at c. 1332 cm^{-1} and 1550 cm^{-1} , respectively, for all samples. Shifts were observed for both peaks with the diamond peak position being at c. 1338 cm^{-1} for the PDD samples. Other characteristic peaks determined were the nanodiamond peak at c. 1130 cm^{-1} and, for the NDD and PDD samples, the 'D' band at c. 1370 cm^{-1} . There were two additional peaks observed at 2900 cm^{-1} and $4200 - 4500 \text{ cm}^{-1}$ for the extended spectra of the NDD and PDD samples. These were unexpected but speculated to be caused by an interaction between the hydrogen termination, and the large, n-type dopants in the NDD and PDD samples. By running additional analyses, specifically through comparison of the Raman spectra before and after thermionic analysis, it was found that, indeed, these peaks displayed a strong relationship with the presence or absence of the hydrogen terminations. However, a negative relation appeared to exist between the dopant concentration and the peak intensity for the PDD diamond samples. An explanation for this could not be given.

Finally, all BDD and PDD samples were tested for thermionic emission. Only the PDD samples showed an emission at 'practical' temperatures below $750 \text{ }^\circ\text{C}$, with each sample showing a threshold temperature between $500 - 600 \text{ }^\circ\text{C}$ on the primary cycle. The highest emission current of 0.108 mA was observed for the 'intermediate' sample (N21136, c. $63\text{k dopants per cm}^2$) at $750 \text{ }^\circ\text{C}$. This corresponds to a calculated effective work function of 1.405 eV . The lowest emission current, and highest threshold temperatures and effective work function was found for the sample with the highest dopant concentration (N21139, c. $250\text{k dopants per cm}^2$): maximum emission of 0.0044 mA at $660 \text{ }^\circ\text{C}$; threshold temperature of $605 \text{ }^\circ\text{C}$; effective work function of 1.687 eV .

The data presented here show that an increase in the doping concentration does not result in a lower work function, or a higher emission current. The data showed an initial increase for increased dopant concentrations but appeared to show that higher doping concentrations are detrimental to the thermionic behaviour of the P-doped samples.

Acknowledgements

I would firstly like to thank Paul May for all the help and support he has provided, not just over the course of this project, but over the course of my entire degree as my personal tutor. He always ensured that, if needed, he was available for questions and advice about everything university related and beyond.

I would also like to thank Neil Fox and James Smith for providing help, insight, and the occasional “ah well” to problems around the lab, of which there were plenty throughout this year.

I would also specifically like to thank Ramiz for being the regular face around the lab that I could always ask for any advice if needed, ask for suggestions to weird observations on spectra, and for always being patient with the endless supply of broken equipment that seemed to plague the lab.

Finally, I would like to thank the entirety of the BUDGie group, especially my fellow undergraduates who made day-to-day life in the lab as enjoyable as they did.

Author Declaration

I declare that the work in this dissertation was carried out in accordance with the requirements of the University's Regulations and Code of Practice for Research Degree Programmes and that it has not been submitted for any other academic award. Except where indicated by specific reference in the text, the work is the candidate's own work. Work done in collaboration with, or with the assistance of, others, is indicated as such. Any views expressed in the dissertation are those of the author.

Signed: 

Date: 09/04/24

Table of Contents:

i.	List of Tables	
ii.	List of Figures	
iii.	List of Abbreviations and Symbols	
1.	Introduction	1
2.	Theoretical Background	3
2.1.	Fundamental Principles of Thermionic Emission	4
2.2.	Applications of Thermionic Emission	7
2.3.	Diamond	11
2.3.1.	Doping	13
2.4.	Surface Terminations	13
2.4.1.	Hydrogen Terminations	14
2.4.2.	Metals and Metal-Oxygen Terminations	14
2.4.2.1.	Group I and II metals	14
2.4.2.2.	Transition Metals	17
2.4.2.3.	Aluminium	17
2.4.2.4.	Scandium	18
2.4.3.	Metalloid Terminations	20
2.4.4.	Non-metal Terminations	20
2.4.4.1.	Oxygen, Hydroxyl, and Carboxyl	20
2.4.4.2.	Nitrogen and Amines	21
2.4.4.3.	Sulphur and Thiols	24
2.4.4.4.	Halides	24
2.4.4.5.	Aliphatics and Aromatics	24
2.5.	Concluding Remarks	25
3.	Methodology	26
3.1.	Samples	26
3.2.	Sample Preparation	26
3.2.1.	Manual Abrasion and Seeding	26
3.2.2.	Grating	27
3.3.	Experimental Growth Conditions	27

3.4. Characterisation	28
4. Results	30
4.1. Raman	30
4.2. SEM	37
4.3. TECsim	44
5. Discussion	46
6. Future Work	53
7. Conclusions	56
8. References	58
9. Appendix	65
9.1. CVD reactors CVD	65
9.1.1. Hot Filament CVD	65
9.1.2. Microwave plasma-assisted CVD	66
9.2. Characterisation Techniques	71
9.2.1. Scanning Electron Microscopy (SEM)	71
9.2.2. Raman Spectroscopy	72
9.2.3. Thermionic Emission Simulator Kit (TECsim)	73
9.2.4. Secondary Ion Mass Spectrometry (SIMS)	76
9.2.5. Photoelectron Spectroscopy	76
9.3. Additional Results, Analyses, and Raw Data	78
9.3.1. Raman Spectra	78
9.3.2. SEM	83
9.3.3. Grain Size Analysis	85
9.3.4. TECsim Spectra	87

List of Tables

Table 2.1: Experimental data for scandium terminated diamond.....	19
Table 3.1: Table of all samples analysed.....	26
Table 3.2: Growth conditions for samples.....	28
Table 4.1: Estimated mean grain size for each sample.....	38
Table 4.2: Hydrogen termination conditions for individual samples.....	44
Table 4.3: Thermionic Emission characteristics for the PDD samples.....	45
Table 5.1: Common peaks seen in the Raman spectra of CVD diamond.....	47

List of Figures

Figure 2.1: Schematic energy diagrams of various types of semiconductor systems.....	4
Figure 2.2: EF-PEEM work function map for AlO-terminated diamond.....	5
Figure 2.3: A schematic of a thermionic energy converter.....	7
Figure 2.4: Simplified energy diagram of a TEC.....	10
Figure 2.5: Schematic of the simplified deposition process of diamond onto a substrate.....	12
Figure 2.6: Simulations of diamond surface reconstructions.....	16
Figure 2.7: Periodic table with each element's electronegativity values.....	16
Figure 2.8: Optimised Sc-terminated (100) bare diamond surfaces.....	19
Figure 2.9: O-terminations on (100) and (111) diamond.....	22
Figure 2.10: Simulated structure of C-N-C imine terminations at 1 ML coverage.....	23
Figure 3.1: Mo substrate before and after laser etching.....	27
Figure 3.2: Temperature profile for all thermionic testing cycles.....	29
Figure 4.1: Static Raman spectra for an undoped diamond sample with labelled peaks.....	31
Figure 4.2: Static Raman spectra for a BDD (B1) sample with labelled peaks.....	32
Figure 4.3: Static Raman spectra for a NDD (N5) sample with labelled peaks.....	34
Figure 4.4: Static Raman spectra for a PDD sample (N21134) with labelled peaks.....	35
Figure 4.5: Extended Raman spectra for the PDD samples pre-TECsim analysis.....	36

Figure 4.6: Extended Raman spectra for the PDD samples post-TECsim analysis.....	36
Figure 4.7: Raman spectra for a PDD sample (N21139) before and after TECsim analysis.....	37
Figure 4.8: SEM images of a manually abraded N-doped sample (N4).....	39
Figure 4.9: SEM images of a manually abraded P-doped sample (N21134).....	40
Figure 4.10: SEM images of a manually abraded B-doped sample (B1).....	41
Figure 4.11: SEM images of a manually abraded N-doped sample (N5).....	42
Figure 4.12: SEM images of a manually abraded undoped sample.....	43
Figure 4.13: Thermionic emission cycles between 300 – 750 °C for a PDD sample (N21136).....	45
Figure 6.1: A depth profile of a NDD sample from a calibrated SIMS detector.....	53
Figure 6.2: A heat map of the work function across a bare PDD surface.....	54

List of Abbreviations and Symbols

Abbreviations

CRT	Cathode Ray Tube
OLED	Organic Light Emitting Diode
SEM	Scanning Electron Microscopy
TEM	Tunnelling Electron Microscopy
TEC	Thermionic Energy Converter
VB	Valence Band
CB	Conduction Band
NEA	Negative Electron Affinity
PEA	Positive Electron Affinity
EA	Electron Affinity
VBM	Valence Band Maximum
EF-PEEM	Energy Filtered Photoemission Electron Spectroscopy
BDD	Boron-doped Diamond
NCD	Nanocrystalline Diamond

HV	High Vacuum
UHV	Ultra-high Vacuum
PETE	Photo-enhanced Thermionic Emission
HPHT	High Pressure High Temperature
CVD	Chemical Vapour Deposition
HF	Hot Filament
MW	Microwave
HFCVD	Hot Filament Chemical Vapour Deposition
MWCVD	Microwave Chemical Vapour Deposition
DFT	Density Functional Theory
ML	Monolayer
UPS	Ultraviolet Photoelectron Spectroscopy
RF	Radio Frequency
MFC	Mass Flow Controller
SCCM	Standard Cubic Centimetre per Minute
UNC	Ultrananocrystalline
SIMS	Secondary Ion Mass Spectrometry
XPS	X-ray photoelectron Spectroscopy
PEEM	Photoemission Electron spectroscopy

Physical Constants

A_R	Richardson Constant	$9 \times 10^{-5} \text{ A.m}^{-2}.\text{K}^{-2}$
k_B	Boltzmann Constant	$8.6173303 \times 10^{-5} \text{ eV.K}^{-1}$
m	Electron Mass	$9.10938356 \times 10^{-31} \text{ kg}$
e	Electronic Charge	$1.6 \times 10^{-19} \text{ C}$
h	Planck Constant	$4.1356692 \times 10^{-15} \text{ eV}$

Symbols

φ	Work Function
E_F	Fermi Level
E_{vac}	Vacuum Level
χ	Electron Affinity
E_{CBM}	Conduction Band Minimum Energy
J	Thermionic Emission Current
T	Temperature
η_{Carnot}	Carnot Efficiency
η	Maximum Efficiency
T_E	Temperature of the Emitter
T_C	Temperature of the Collector
V_{EC}	Potential Difference between the Emitter and Collector
V_W	Energy Loss due to Electrode/Wire Connection
R	Energy Losses due to Black Body Radiation
H	Energy losses due to Thermal Conduction
φ_C	Collector Work Function
φ_E	Emitter Work Function
P	Power Output
E_{sc}	Energy Barrier due to Space Charge Effects

1. Introduction

Modern technologies play an increasingly powerful role in, for example, increasing the speed of data processing or the efficiency of sustainable energy use.^{1, 2} Many advancements in these areas now hinge on the improved control of the properties of existing and new materials that are used to create or facilitate them. One of these properties, which is the subject of the research presented in this dissertation, is the controlled emission of electrons from a material. Applications that make use of this material property range from emissive flat-panel displays to high-power microwave amplifiers, and also characterisation methods such as scanning electron microscopy (SEM) make use of this electron emission.³⁻¹⁰ More specifically on these applications, Cathode Ray Tube (CRT) displays use electron guns to fire electrons at a phosphorus-coated screen to produce pixels, and, similarly, Field Emission displays also rely on emission of electrons to generate images. Modern Organic Light Emitting Diode (OLED) displays, which do not directly emit electrons, still rely on the controlled flow of electrons through organic compounds to produce light, colour, and images. Apart from visual displays, control of the electron emission rate is also vital for characterisation methods such as SEM and transmission electron microscopy (TEM) as both require an electron beam to interact with the studied material. Importantly, electron emission is also applied in apparatuses that employ microwave amplification. In vacuum electron devices specifically, electrons emitted from a cathode are accelerated through arrays of electrodes to amplify the microwave signals. Finally, an application where emission of electrons is vital, and which is directly relevant for the study reported here, is in the process of Thermionic Energy Conversion (TEC). TEC devices convert heat into electric current in a way that is not dissimilar to how photovoltaic cells convert light into electric current.

To improve the efficiency of such novel applications, research involves enhancing ways to control the rate of electron emission from materials. To achieve this, and this will be explained in more detail in the theoretical background sections below, research focus is on decreasing or removing the emission barriers that electrons need to overcome at elevated, material-specific temperatures, with a view to lowering these threshold temperatures. This is achieved through the tuning of the work function. The work function is defined as the difference in energy between the Fermi level and the vacuum level. The Fermi level (E_F) is the highest energy that an electron can possess in a semiconductor at a specific temperature. At absolute zero, the Fermi level is equal to the Fermi energy. Another important term in this context, which will also be explained in more detail below, is the band gap of a material. This band gap mainly determines the potential emission barrier, defined as the difference in energy between the valence band (VB) and the conduction band (CB). The band gap for most semiconducting materials, along with the magnitude of the work function, is in the order of several eV (e.g., 1.11 eV for Silicon (Si), 5.47 eV for diamond),¹¹ and this means that normally temperatures exceeding 1500 K are required to promote electrons from the Fermi energy to vacuum or to the CB for further emission. Unfortunately, for everyday applications this is unfeasibly high, which makes it one of the key drivers for research in this field. Particularly the reduction of the temperature at which electron emission occurs, the previously mentioned threshold temperature, is looked at. One specific way in which this could be achieved is through the creation of an 'alternative' emission pathway.¹²

Most semiconducting materials exhibit a positive electron affinity (PEA), which is when the Fermi level lies in the band gap, whilst the vacuum level is higher in energy than the Conduction Band Minimum (CBM). This means that at normal operating temperatures, the VB is at least partially occupied, and the CB is unoccupied but also that any electron promoted into the CB will still have a further barrier to overcome to be emitted to vacuum. This additional barrier is defined as the electron affinity (EA) and as the name suggests, for a PEA material, this will be positive. However, for some materials, such

as diamond, an alternative and potentially very useful emission pathway is possible if the conduction band minimum (CBM) lies higher than the vacuum energy (E_{vac}). Emission can then occur when the electrons are promoted into the CB, as there would be no further emission barrier to overcome for electrons to be emitted.¹³ This interesting phenomenon is known as a negative electron affinity (NEA), and an NEA surface on a material such as artificial diamond can thus theoretically be used practically in electronic applications. Research focuses therefore on creating such mid-band gap states, which can be achieved and further enhanced by doping diamond surfaces with e.g. boron, phosphorus, nitrogen, or terminating the surface with species such as hydrogen. By using suitable dopants or surface terminations, the introduction of mid-band-gap donor levels and band bending (explained in Section 2) have been shown to produce very small barriers to emission.^{12, 14-18} For diamond, this means that through the heating of an appropriately doped and terminated sample, emission can be induced at temperatures significantly lower than those seen for metals and most other semiconductors.

The objective of this study is to examine how different types of doping of prepared diamond films affect the electron affinity and thermionic emission characteristics. This study aims to characterise seven hydrogen-terminated, doped diamond systems before analysing the thermionic emission properties of each sample. The samples studied are undoped diamond, boron-doped diamond (BDD), nitrogen-doped diamond (NDD), and phosphorus-doped diamond (PDD), all terminated using hydrogen. The undoped, BDD and NDD samples were prepared and grown in the laboratory in Bristol, and the PDD samples were supplied by the Institute of Physics of the Czech Academy of Sciences. These latter samples were grown with varying dopant concentrations, which allowed for the assessment and evaluation of the effects of dopant concentration on the thermionic emission properties.

Before the presentation and analysis of results, and details about sample preparation and the laboratory equipment that was used, the following section will first cover the theoretical background of thermionic emission, TEC devices, artificial diamond growth, p-type and n-type doping, and the surface termination of diamond.

2. Theoretical background

Whilst finding practical routes to improve electron emission and to lower threshold temperatures has proven challenging, the theory behind controlling the rate of electron emission from materials is reasonably straightforward. Figure 2.1a shows a schematic of an undoped, intrinsic semiconductor system and the relationship between the Fermi level, electron affinity, and the work function. Most materials currently used in electronics (silicon, for example) exhibit energy structures such as this. However, in next-generation electronics, attempts are made to exploit the previously mentioned alternative electron emission pathways to thermionic emission (see Section 2.1 below). As stated above, these are offered by materials with a negative electron affinity (NEA). Figure 2.1b shows the energy characteristics of such so-called ‘true’ NEA materials: they have ultra-wide bandgaps and vacuum levels that are below the CBM. Recent research has focused on such materials, with specific attention to diamond, AlGaN, AlN, and cubic boron nitride.^{19, 20} This alternative pathway is possible because any electrons excited into the CB can be emitted with no further barrier, resulting in electrons with kinetic energies of several eV. The kinetic energies of the emitted electrons are usually of a similar magnitude to the NEA of the surface. In practice however, electron excitation may be complicated by a phenomenon called band bending. Although band bending is not a physical effect, it represents the energy offset that occurs at a boundary due to a difference in the surface charges. In a p-type material, the Fermi level is “pinned” near the valence band maximum (VBM), whilst the CB and VB are simultaneously pulled downwards at the surface (Figure 2.1c & 2.1d). If the CBM remains above the vacuum level, even with the downward band bending, then it will still be a “true” NEA (Figure 2.1c). If the bending causes the CBM to drop below the vacuum level, an “effective” NEA is produced (Figure 2.1d). In this case, any electrons that are promoted will theoretically have enough energy to be emitted to vacuum. However, emission only occurs by tunnelling, which is a phenomenon where the electron passes into vacuum by jumping ‘through’ through the potential barrier. Some electrons may get trapped behind the small potential barrier, meaning that an effective NEA has a lower emission rate than a true NEA. An n-type material has a reversed situation. The Fermi level is “pinned” just below the CBM, and the bands bend upwards (Figure 2.1e).

The electron affinity (EA) is defined mathematically by:

$$\chi = E_{\text{vac}} - E_{\text{CBM}} \quad (1)$$

From a non-excited state, the total energy needed to emit an electron is therefore given by:

$$\varphi = \chi + E_{\text{F}} \quad (2)$$

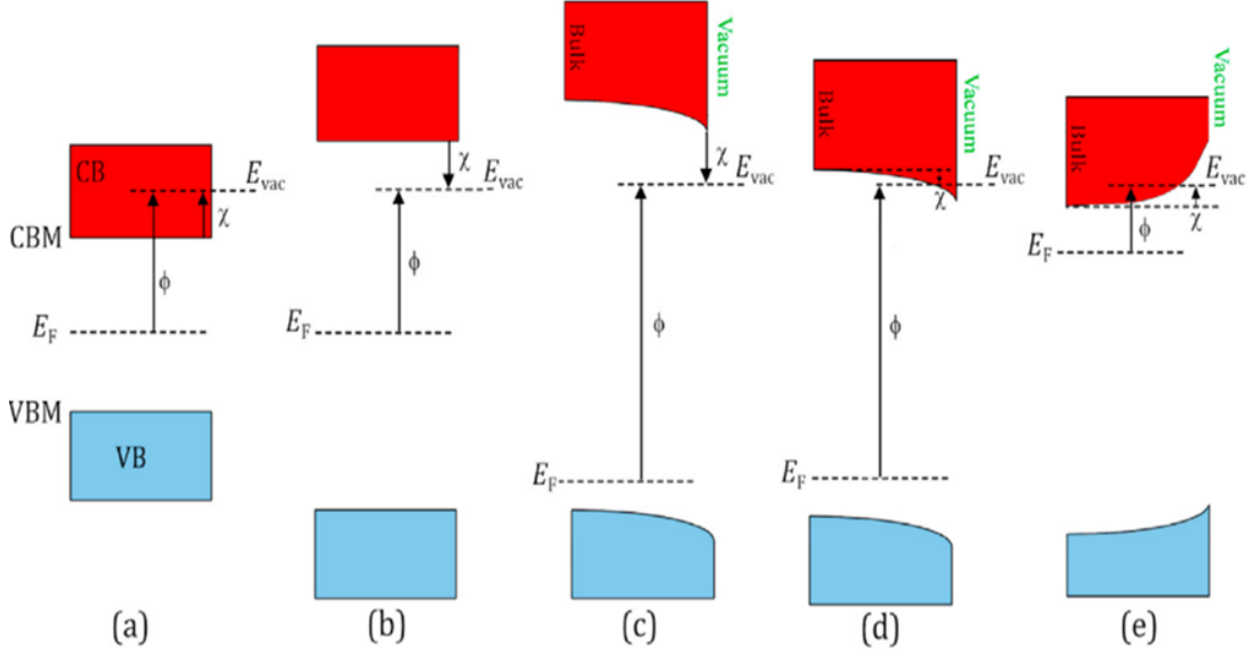


Figure 2.1: Schematic diagram showing the relationship between the electron affinity, χ , and the work function, ϕ , in relation to a fixed vacuum energy level, E_{vac} , for various semiconductor materials, VB is the valence band and VBM is its corresponding maximum energy. CB and CBM are the conduction band and its minimum energy, respectively. The Fermi level (E_F) position depends on whether the material is p- or n-doped: **(a)** PEA for an undoped material, **(b)** true NEA for an undoped material, **(c)** true NEA in a p-doped material, downward band bending is illustrated on the material surface interface, **(d)** effective NEA in a p-doped material where the downward band bending brings the CBM below the vacuum level, and **(e)** PEA in an n-doped material where the upwards band bending at the interface brings the CBM above the vacuum level. Diagram adapted from James et al. [12]

2.1. Fundamental Principles of Thermionic Emission

Thermionic emission is the emission of electrons from a surface that occurs when the emitter is heated (usually taking place in vacuum). Thermionic emission was first studied in 1901 by Richardson and is simplified to be described by the Richardson-Dushman equation:^{21, 22}

$$J(T) = A_R T^2 \exp\left(-\frac{\phi}{k_B T}\right) \quad (3)$$

where J is the emission current density as a function of the material temperature, A_R is the Richardson constant, T is the absolute temperature of the emitting material, ϕ is the work function, and k_B is the Boltzmann constant. The work function has a crucial effect on the emission of a material. Until recently, studies have focused on the work functions of metals and found that metals that typically have work functions with magnitudes between 3 eV and 5 eV have minimum temperatures at which thermionic emission occurs (with emission current densities usable for electronic applications ($>1 \text{ A cm}^{-2}$)) that exceed 1500 K.^{23, 24} These temperatures are not suitable for many applications as they tend to require specialist equipment, and need a large amount of energy. Therefore, the development of thermionic emission devices has been delayed for decades. More recently it was

found that materials that can exhibit NEA, such as diamond, temperatures of c. 800 °C can achieve the same current densities (from Equations 2 and 3). This of course is a much more practical temperature for electronic applications and resulted in a new surge of interest in thermionic emission.

The Richardson constant was originally proven to be a “universal” constant, although the dimensionless multiplier of 4π was not identified.²² The Richardson constant has since been theoretically derived for metals as:²⁵

$$\frac{4\pi m k_B^2 e}{h^3} = 120.2 \text{ A cm}^{-2} \text{ K}^{-2} \quad (4)$$

where m and e are the mass and charge of an electron, respectively, and h is the Planck constant. Both the derivation of the Richardson-Dushman equation and the Richardson constant of metals assumes a uniform work function and temperature across the surface. This model also uses a Maxwell-Boltzmann distribution of electron energies, which only applies at high temperatures. Due to these assumptions, the actual value of A_R often differs from the value predicted by the Richardson-Dushman equation. The calculated Richardson constant is therefore often multiplied by an experimentally determined correction factor. However, the simplicity of Equation 3 means that it is still widely used. Tables exist for the Richardson-Dushman constants of common materials, such as the one found in reference [12].¹²

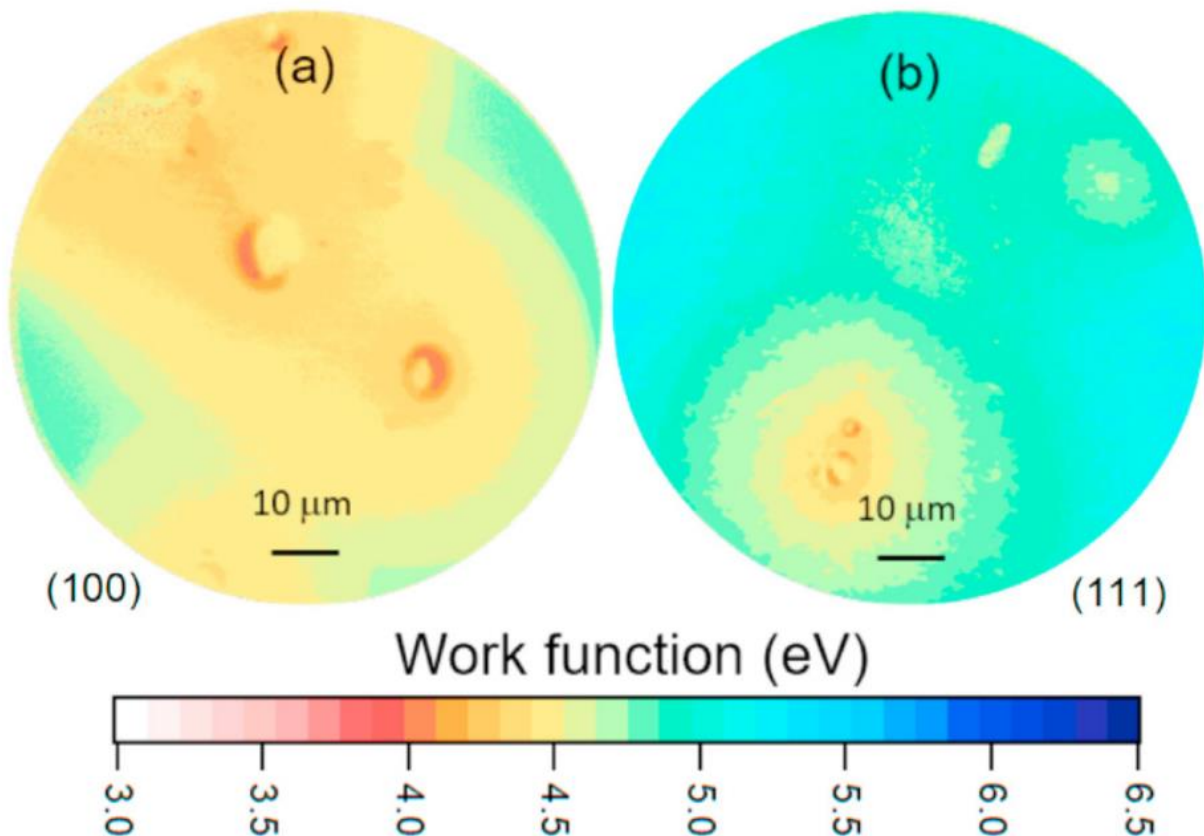


Figure 2.2: EF-PEEM images showing the work function across (100) and (111) diamond surfaces terminated with AlO. There are areas present, due to incomplete coverage, which have a different work function to much of the surface. Image from James (2020). [26]

The Richardson-Dushman equation is limited in its applicability to doped diamond due to assumptions that were made while deriving it. As stated, constant work function and temperature is assumed across the surface. James (2020) showed that for the deposition of diamond, terminated by AlO, the work function is not uniform across the whole surface (Figure 2.2).²⁶ For bulk metals, this assumption may hold true, but for any system which involves deposition, there can thus be discontinuities in the surface coverage. While little work specifically with diamond surfaces has been done, that is measuring thermionic emission and the effect of its surface morphology on the uniformity of the thermionic emission, work has been done on the effects of the morphology on the field emission of diamond.²⁷ In this situation, an applied electric field will be concentrated at any distinguished features on a surface such as points or edges. This lowers the effective barrier of emission. This phenomenon has led to research into the development of microstructured surfaces.²⁸ ²⁹ For diamond applications, nanoscale graphitic inclusions dominate the effects of surface features in lowering the local work function (see also below). Due to such inclusions, field emission from doped diamond surfaces is believed to originate from the grain boundaries of the deposited diamond.^{27, 30} These inclusions therefore change the work function of the surface, which will not always be accounted for.

The Richardson-Dushman equation further relies on a Maxwell-Boltzmann distribution for the electron energies, which only applies at high energies. While the Maxwell-Boltzmann distribution is not appropriate for characterising energies at lower temperatures, for systems with depositions or coatings, this model simply does not work. There have been several studies on doped and undoped diamond at elevated temperatures. Robinson et al. used a hemispherical energy analyser to study boron-doped diamond (BDD), which is also studied here, and found that emission occurred from multiple regions with varying work functions.³¹ Interestingly, the relative peak intensities shifted indicating that the surface morphology varied with temperature. A residual gas analysis suggested that the hydrogen termination was desorbing from the diamond resulting in uneven coverage, and hence, uneven work functions. Similarly, Uppireddi et al. examined nanocrystalline diamond (NCD) and fitted a free electron model to the measured emissions between 700 °C and 900 °C.³² The work function was found to vary across the surface, due to unstable surface chemistry at high temperatures. It demonstrated that the surface itself is often not stable when temperature regions where the Maxwell-Boltzmann distributions theoretically apply, start being approached. In recent work, thermionic emission currents were remodelled under alternative conditions.^{33, 34} A non-equilibrium Green's function approach was utilised that, unlike in Richardson's work, did not require semi-classical approximations or simplifications of the electronic structure of the materials. This method calculates the emission current using Fermi-Dirac statistics from an effective mass description.³⁴ Both studies found that the Richardson-Dushman equation overestimated the emissions for many materials, most noticeably for materials with a low, or negative, electron affinity. Given that it is preferable for thermionic emission applications to have materials with a minimal electron affinity, Musho et al. developed an equation that links the work function, electron affinity, and Richardson's constant that can aid in identifying Richardson's parameters; useful for experimental characterisation of metals.³⁴ Another study, by Olawole and De, into modelling thermionic emission from carbon nanotubes, used a modified version of the Richardson-Dushman equation that considered the thermal expansion of the lattice, and the change of the chemical potential with temperature in the material.³⁵ This slight increase in complexity yielded a good experimental agreement for work function, Fermi energy, and the linear thermal expansion coefficients. Such studies have shown that the Richardson-Dushman equation can be improved substantially using modelling and through consideration of the thermal effects on the materials.

2.2. Applications of Thermionic Emission

One of the most common applications of thermionic emission is in Thermionic Energy Converter (TEC) devices, and these can be employed for the generation of energy from heat. Figure 2.3 shows a basic schematic of a TEC device. In its simplest form, the structure consists of an emitter and a collector connected electrically by some load. The emitter and collector are separated by a vacuum gap which ensures that the emitted electrons reach the collector.³⁶⁻³⁸ In TECs, the cathode (emitter) and the anode (collector) are heated and cooled, respectively, to create a temperature gradient across the gap. The difference in work function between the electrodes results in a potential difference across the gap. The connection of the two electrodes results in a current, and hence, the conversion of heat into electricity; all in an entirely static system. A comprehensive review of TEC devices can be found in references [39 - 41].³⁹⁻⁴¹

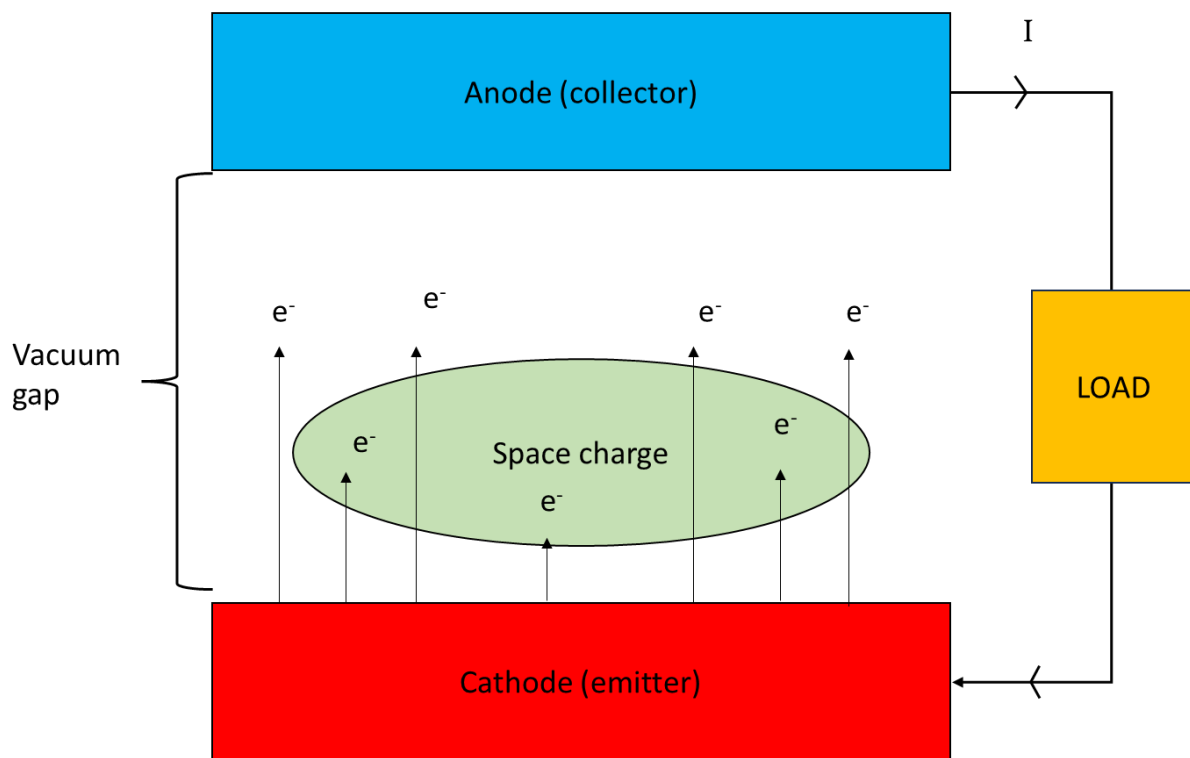


Figure 2.3: A simplified schematic of a thermionic energy converter. Adapted from [12].

It is commonly accepted that having a high- or ultra-high vacuum (HV or UHV) in the gap between the electrodes helps the emitted electrons to reach the collector. Additionally, this has a secondary benefit of thermally insulating the two electrodes from each other, which maximises the efficiency of the device. The efficiency of a TEC can be measured using a Carnot efficiency (η_{Carnot}), if TECs are modelled as simple heat engines.³⁸

The maximum efficiency (η) is in this case given by:

$$\eta_{\text{Carnot}} = 1 - \frac{T_E}{T_C} \quad (5)$$

where T_E and T_C are the respective temperatures of the emitter and the collector. However, another method to estimate the maximum efficiency is to consider the total useful power output divided by the total power output:⁴²

$$\eta = \frac{J(V_{\text{EC}} - V_{\text{W}})}{R + H + J_{\text{E}}(V_{\text{E}} + 2k_{\text{B}}T_{\text{E}})} \quad (6)$$

Where J is the emission current density from the emitter, V_{EC} is the potential difference between the electrodes, V_{W} is the loss of energy from connection of room temperature wires to the electrodes, and R and H are the losses due to black-body radiation and thermal conduction, respectively.

To ensure that there is a forward bias on the electrodes, the collector work function, φ_{C} , needs to be at least 1 eV smaller in magnitude than the emitter work function, φ_{E} ,³⁷ remembering that the emitter work function should be minimised to reduce the potential emission barrier. According to the Richardson-Dushman equation (Equation 3), an emitter with a higher work function will require a higher thermal input to achieve the same emission current densities as one with a lower work function.

However, the power density of the TEC is proportional to the difference between the work functions of the electrodes:

$$P(T) = A_{\text{R}}T_{\text{E}}^2 \exp\left(-\frac{\varphi_{\text{E}}}{k_{\text{B}}T_{\text{E}}}\right)(\varphi_{\text{E}} - \varphi_{\text{C}}) \quad (7)$$

where the maximum power output is given by the condition: $\varphi_{\text{E}} = \varphi_{\text{C}} + k_{\text{B}}T_{\text{E}}$.⁴³

As $k_{\text{B}}T_{\text{E}}$ is small (~ 0.1 eV), this equation suggests that for maximum device power, the work functions of the electrodes should be similar. However, the efficiency is maximised when the difference between the magnitudes of the emitter and collector work functions is ≥ 1 eV. This leads to a trade-off between maximum power and efficiency. Despite this, it has been shown that efficiencies of more than 30% are theoretically possible.^{42, 44} Zeng managed to achieve corresponding Carnot efficiencies of 50% using an adapted thermionic method that uses vacuum thermionic emission and tunnelling to lower the work function.⁴⁵

There are still several challenges that need to be addressed before TECs can be used for everyday applications. Interestingly however, TECs have already been used by the former Soviet Union since 1987 to generate power as part of the 5 kW TOPAZ nuclear reactors,³⁹ and have since also been considered for use in space travel missions to image the Sun and Mercury,⁴⁶ and for various other applications for energy generation and waste heat scavenging.^{12, 17, 18, 40, 47-49}

The main challenges that the use of diamond could help overcome are related to the electrodes. The design of TECs requires that both the back of the emitter (where the light is absorbed) and the surface of the collector absorb as much light as possible. The emitters and supports must therefore be efficient thermal conductors to reduce dissipating the heat as it travels to the emitter surface. Optimising this thermal conductivity can be achieved by depositing a thin layer of diamond onto the emitter substrate (usually molybdenum (Mo) or Si). Furthermore, diamond can be 'patterned' into

microstructures such as needles to maximise the light absorption at the surface,^{29, 50} as such “black diamond” layers absorb ~98% of the full spectrum of solar light.⁵¹ This means that the diamond layer improves both the thermal conduction to the emitter surface, and the amount of light absorbed by the substrate. A drawback of this however is that any additional layer/interface will result in heat losses, which cannot be ignored when calculating the device’s efficiency.⁵² Similar to the emitter, the collector needs to be as efficient as possible at electron absorption. This can also be achieved by a nano-structured surface.⁵³ Moreover, the collector needs to be cooled to prevent “reverse emission” as it will start to emit electrons itself if heated, as it has a lower work function than the emitter. Reverse emission will be a detriment to the efficiency of the TEC.

Another widespread problem with TECs is the production of a space-charge (Figure 2.3). This is the accumulation of an “electron cloud” in the gap between the electrodes. It occurs if the emitted electrons have insufficient energy to reach the collector or are not absorbed. These electrons are then attracted back to the emitter and collect in the gap. This negatively charged cloud then hinders further emission by creating an additional energy barrier to emission, shown as an additional barrier, E_{SC} , in Figure 2.4. The methods studied to reduce the effect of the space charge includes filling the gap with low pressure gases that interact with the electron cloud, partially neutralising it.^{18, 42, 54, 55} However, adding any gas to the system will introduce another source of collector heating; convection. Another attempted method to reduce space-charge is to decrease the distance between the electrodes, hence decreasing the kinetic energy that the electrons need to cross. For optimal device performance, this distance is a few micrometres.⁵⁶ In this situation, a diamond electrode with NEA is well-suited as the CBM lies above the vacuum level; reducing the effect of the barrier caused by a space-charge. A third method studied extensively is by applying a forward bias to the TEC cell (in favour of the collector).¹⁶ This is the favoured method for most thermionic testing as the amount of bias can be changed during experiment, if required.

This can be achieved by electric or magnetic fields, or by applying a voltage. Finally, research by Croot et al. found that by using a β -emitting collector, composed of ^{63}Ni with ^{58}Ni as a control, the observed current increased by a factor of 2.7 when compared to H-terminated diamond.⁵⁷ It is still unclear exactly why this reduces the space charge as theoretically, the β particles should also become trapped in a cloud near the cathode.

As was touched upon earlier, the surface morphology or texture of the electrodes also affects the emission rate. For diamond applications, nanoscale graphitic inclusions dominate the effects of surface features in lowering the local work function. Whilst the exact mechanics are still unclear, field emission from the electrodes is believed to originate mainly from the grain boundaries between inclusions and the deposited diamond.^{27, 30} Figure 2.2 shows the work function map for AlO-terminated diamond onto (100) and (111) surfaces respectively. Lower work functions can be observed for features of the surface. In this figure, (100) and (111) simply refer to the orientation of the diamond lattice growth.

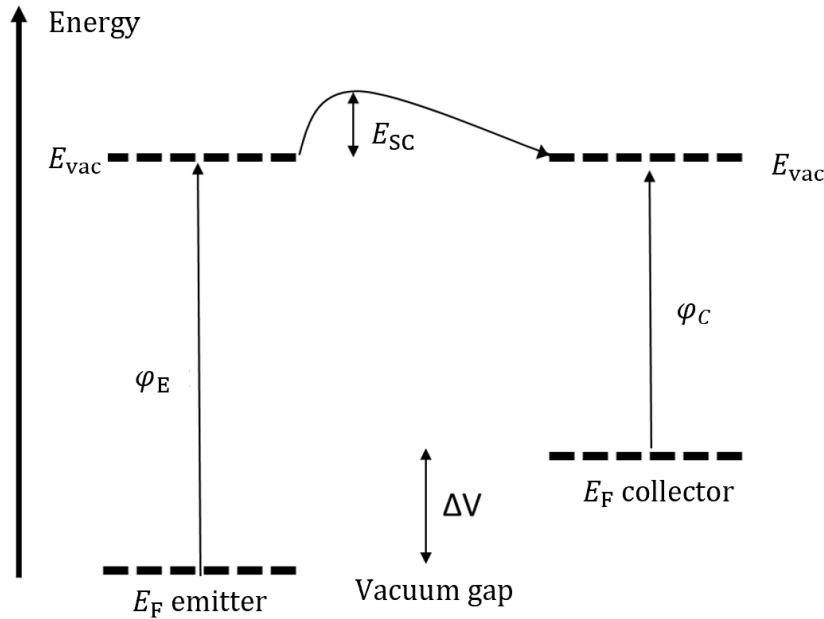


Figure 2.4: Simplified energy diagram of a TEC with the additional energy barrier due to the space charge, E_{SC} . It is possible that this barrier is higher than the vacuum energy, E_{vac} . The respective Fermi levels, E_F , for the emitter and collector are labelled, as well as the voltage, ΔV , that would be produced by the device. φ_E and φ_C are the work functions for the emitter and collector, respectively.

Several methods have been proposed to improve TEC devices, with one of the more common ones known as photo-enhanced thermionic emission (PETE). In this case, photon absorption is used to supplement the thermal energy to aid in promoting the electrons into the CB. A study by Elfimchev et al. showed that despite there not being a significant improvement at the normal temperatures for thermionic emission (i.e. thermal energy is sufficient), the rate of electron emission increased by several orders of magnitude at lower temperatures.⁵⁸ Most PETE devices require that light hits the surface of the emitter directly, which can be achieved by using a transparent collector.⁵⁹⁻⁶¹ Diamond is transparent to solar radiation, so in order to be used as an electrode in solar applications, an intrinsic diamond substrate has to be coated in p-type “black diamond” on the absorption surface, and a H-terminated layer on the emission surface.⁶² This would suggest that diamond is well suited to PETE applications, however, the cost and complexity of such solutions might mean that it never becomes feasible for commercial use.

Radiation can also be used to aid the emission of electrons. Using waste radioactive graphite sources to create ^{14}C methane for CVD deposition, a layer of ^{14}C diamond can be deposited onto a TEC emitter. When heated, this radioactive layer will emit electrons along with the thermionically emitted electrons thus increasing the total emission. This differs from the method described by Croot et al. as in this situation the β source is deposited onto the emitter, rather than being used as a collector.⁵⁷ This concept has been applied to “betavoltaic batteries”, which use the β layer, but no substrate. Other designs have also been suggested,^{63, 64} and it is thought that such devices would be able to produce “trickle” power for thousands of years but would only produce a few μW per cell. Due to this low output, they would have to be connected in series to create usable powers. One way of achieving this could be to use them in charging capacitors for short bursts of high powers.

2.3. Diamond

For reasons outlined above, manufactured diamond has held a promising position in material science, and it is also the focus in the present study. Of course, diamonds are commonly known as precious gemstones but, since the development of various deposition techniques that allow diamonds to be manufactured, they have also become the subject of research focusing on electrical applications.⁶⁵⁻⁶⁷ Diamonds are naturally formed under extreme temperatures and pressures so, in a method called high-pressure high-temperature (HPHT) deposition, attempts are made to recreate such natural conditions.^{68, 69} In this method, graphite is compressed to thousands of atmospheres in the presence of a metal catalyst, and heated to temperatures in surplus of 2000 K, until diamond crystallises.⁷⁰ The main drawbacks of the HPHT method are the high costs and the limitations on the growth size. Typically, one would not be able to grow single crystals larger than a few millimetres. These limitations mean that for practical electronic applications, an alternative deposition method is required. A good candidate is Chemical Vapour Deposition (CVD), which is a gas phase deposition technique that deposits carbon atoms, one at a time, onto a surface to form diamond, an sp^3 carbon structure.⁷¹ This is the preferred method for much modern research but, until the late 1960s, the deposition rate of this method was slow, because graphite, an sp^2 carbon structure, was co-deposited along with the diamond. It was not until Angus et al. showed that by adding atomic hydrogen into the gas chamber, the graphite was preferentially etched during deposition, thus improving the deposition rate of the diamond.^{72, 73} Consequently, it was quickly discovered that through the use of CVD, diamonds could also be grown on non-diamond substrates.^{74, 75} All these discoveries culminated in the early 1980s in the construction of “Hot Filament (HF)” and “Microwave Plasma (MW)” CVD reactors.⁷⁶⁻⁷⁸

Recent research has found that diamond can be both etched, and grown, on patterned surfaces.^{61, 79, 80} Both etching and growing can be employed to create diamond nanostructures ranging from nanowires to foams. It also holds great potential for electrochemical applications due to diamond's large bandgap of 5.47 eV, which can be tuned by doping with elements such as boron to get n-type diamond or, nitrogen or phosphorus to get p-type diamond.⁸¹ In the last decade, diamond has also started to be studied for photocatalytic applications and research suggests that the surface morphology and composition also play a role in its electronic characteristics. Such properties, along with the ability of diamond to be terminated with different species, make diamond exciting for electronic applications.

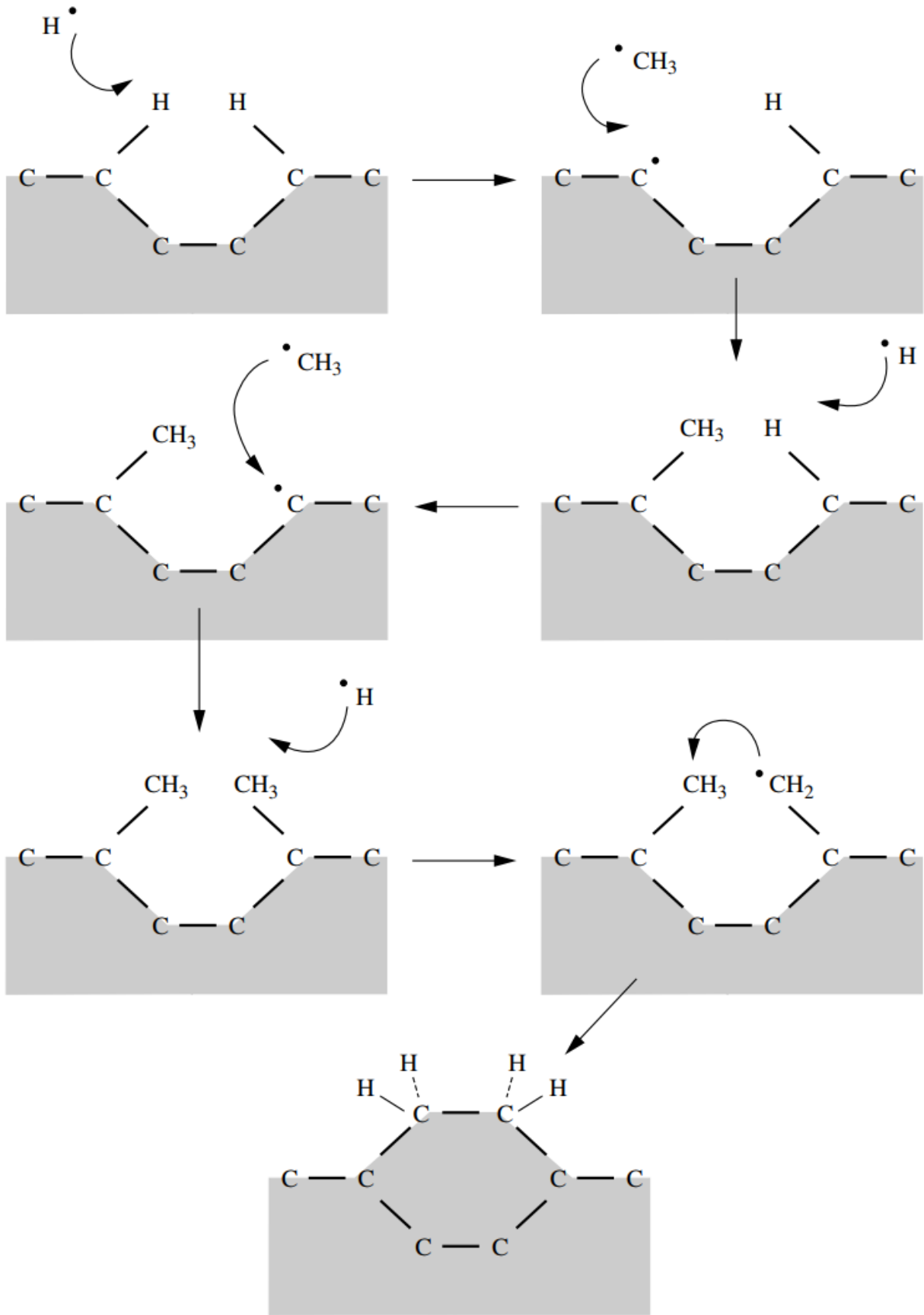


Figure 2.5: Schematic of the deposition process of diamond onto a substrate. Schematic by Professor Paul May.⁷⁰

2.3.1. Doping

The present study looks at the effects of introducing a range of dopants to diamond surfaces. Introducing dopants into the diamond lattice allows for the tuning of the work function, and thus the controlling of the emission energies of the diamond. In general, it may be expected that n-type dopants reduce the work function, whereas p-type dopants will increase it. However, a p-type semiconductor can be useful for thermionic emission applications if there is a large degree of band bending and a large NEA. In this situation the emission energies can still be sufficiently small to be practical.^{15-18, 44, 82, 83}

For N- and P-doped diamond, the work function has been shown to increase when compared to undoped (111) diamond. In the case of the (100) diamond, the N-doped system was computationally shown to decrease, however.⁸³ Despite this, a significant increase in the electron affinity was demonstrated in computational studies by Larsson et al. (2020). Undoped H-terminated (100) and (111) diamond surfaces showed EAs of -0.9 eV and -1.0 eV, respectively, whilst the H-terminated N-doped (100) and (111) surfaces showed EAs of 3.4 eV and 4.3 eV and the H-terminated P-doped systems had EAs of 2.9 eV and 4.2 eV, respectively. This corresponds to large, positive work functions in the range of 4-5 eV. Previous work by Suzuki (2009) had found that N-doped, nanocrystalline diamond had a work function of 1.99 eV,⁸² and another study by Koeck (2011) found a work function of 1.44 eV for nitrogen-doped films.¹⁸ In the same experimental study, Koeck found a work function of 1.18 eV for PDD.¹⁸ All these experimental results were significantly lower than the computationally established values of 4.0 eV and 4.9 eV for (100) and (111) PDD.⁸³ On the other hand, the p-type BDD theoretically resulted in an NEA. This was also shown by the computational work by Larsson, who found EAs of -0.6 eV and -0.3 eV for (100) and (111) diamond, respectively.⁸³ This corresponds to work functions of 3.4 eV and 3.2 eV. Experimental work by Paxton in 2012 found a work function that was slightly higher at 4.43 eV.⁸⁴ It is noted here that for the purpose of this study only hydrogen surface terminations are of direct relevance. While the initial idea for this study was to compare hydrogen- and scandium-terminated samples, a series of equipment failures meant that, unfortunately, only hydrogen-terminated samples could be produced and tested. For the sake of completeness however, it was decided to review a more comprehensive set of termination species in the following section.

2.4. Surface Terminations

During CVD growth, carbon atoms on the surface cannot bond in the same way as carbon atoms in the bulk.⁷⁰ The surface atoms are highly reactive due to the free radicals that are produced during the deposition. Figure 2.5 shows a simplified schematic of this deposition process.⁷⁰ Due to the high surface energies, the atoms can migrate out of the crystal sites to reduce the overall energy.²⁶ This process, known as surface reconstruction, can affect the arrangement of atoms within multiple layers into the surface. To counteract this process and to ensure homogeneity of the diamond bulk, surface carbons are terminated with atoms of a different species. Changing the surface termination species can affect the electronic and surface structure of the diamond, as well as the reactivity of the surface.

For CVD diamond, (100) and (111) are the predominant surface growth directions, of which the (111) direction is also the natural cleavage plane of diamond.⁸⁵ Both growth directions, with their preferred surface reconstructions, are shown in Figure 2.6. These surface reconstructions are, in both cases, the

(2x1) reconstructions, where C=C dimers are formed parallel to the surface. Both surface reconstructions have a slight PEA.⁸⁶ Figure 2.6d shows growth directions where the structures zigzag perpendicular to the surface; these reconstructions are known as Pandey chains.⁸⁷

The electronegativity of a termination species affects the magnitude of the NEA. Theoretically, the larger the electronegativity, the more positive the resulting surface's electron affinity will be. Figure 2.7 shows the periodic table with the relative electronegativities of all the elements indicated. For a diamond surface to form an NEA, the element used for termination must have a relative electronegativity of less than 2.6. In other words, not all elements are suitable for termination. In the following review, those elements that are commonly used for diamond termination will be discussed.

2.4.1. Hydrogen Terminations

Hydrogenation of diamond can be achieved simply through any method that involves subjection to a high-temperature hydrogen gas.⁸⁸⁻⁹⁰ Due to the hydrogen-rich reaction conditions of CVD, hydrogen termination occurs as the standard, but it is guaranteed by only introducing hydrogen into the reaction chamber for the final few minutes of the growth. For the (100) surface, hydrogenation results in the surface reconstruction, whereas for the (111) structure generally no surface reconstruction occurs. Hydrogen termination has been experimentally shown to give diamond an electron affinity of between -0.7 eV and -1.3 eV for both the (100) and (111) surfaces.^{86, 91-94} Computational studies using Density Functional Theory (DFT) calculations have predicted values of approximately -2 eV.⁹⁵⁻⁹⁷ Emission from H-terminated diamond starts below 600 °C, with the emission current density increasing with increasing temperatures (see Equation 3). Unfortunately, above 700 °C most of the hydrogen layer will desorb from the surface. This corresponds to an adsorption energy of approximately -4 eV per atom, consistent with DFT calculations. This upper temperature obviously limits the usefulness of H-terminated diamond for thermionic emission applications as it restricts the maximum emission current density. Further research has shown that there is a decrease in the peak emission current as the temperature is cycled. This decrease was even seen for cathodes operating at low temperatures of around 600 °C, and therefore, low emission currents.⁵⁷ As the number of cycles increases, the threshold temperature for thermionic emission also increases, meaning that after several cycles, a higher temperature is needed for thermionic emission. H-terminated diamond has also been shown to emit electrons under UV radiation. The electrons released in this process are highly reductive and have been shown to break down highly stable molecules, such as N₂ into NH₃. This creates new possibilities in finding catalysts for use in industry.^{98, 99} However, oxidation at the electrode surface tends to remove the NEA at the surface, which necessitates alternatively terminated surfaces.

2.4.2. Metals and Metal-Oxygen Terminations

2.4.2.1. Group I and II metals

H-terminated diamond's instability at thermionic emission operating temperatures has created the need for alternate terminations. Figure 2.7 shows that the group I and II elements are a lot less electronegative than hydrogen so should theoretically result in large NEAs.¹² Work has been done for

various small metals such as Na, K, Li, and Cs. Their field emission behaviour was also studied and shown to be an order of magnitude larger than H-terminated diamond.⁵ However, most of the work on group I and II metals has been done on combined metal-oxygen terminations as the increased bond strength results in higher thermal stabilities. Usually, metal-oxygen terminations are studied up to one monolayer (ML) coverage. The electron affinities of the metal and metal-oxygen terminations are often similar in magnitude however, despite the addition of the electronegative oxygen. This is due to the metal being completely ionised and, at least partially, oxidised. Consequently, the metal-oxygen-diamond surfaces are also assumed to be air stable.¹⁰⁰ Caesium-oxygen terminations showed promise as a thermionic emitter as they exhibit a NEA,¹⁰¹ however, later research showed that it would desorb from the surface above c. 440°C.¹⁰²⁻¹⁰⁴ It is air-stable and capable of emission however.¹⁰¹⁻¹⁰⁶ Comparison to other group I metals indicates that a species' electropositivity is not the only factor that determines the magnitudes of the NEA and the work function. Instead, research shows that lighter elements have a much higher thermal stability,^{102, 107, 108} suggested to be due to the smaller termination species size and metal-oxygen bond length achieving higher coverage, in turn resulting in a larger surface dipole. Indeed, larger atoms will have a higher steric hindrance as they tend to be further away from the surface. Hence, the thermal stability is inversely related to the size of the group I element, as smaller elements form a better ionic bond and thus have a stronger dipole-dipole interaction.

Li-O diamond systems also receive lots of attention. Computational work has indicated that these systems will have a similar thermal stability to H-terminated diamond, but with a negative electron affinity as low as -3.50 eV, particularly for the (111) surfaces.^{107, 109} Experimentally, both thick- and thin-film processes have been used on (100) diamond. While the thick film method is cheap and easy, it is hard to reproduce and typically led to an inconsistent NEA across the surface. It was shown however, that by increasing the annealing temperature and/or deposition thickness, a resultant decrease of the work function was seen.^{12, 101, 110} Additionally, a transition from a PEA to NEA was observed at an annealing temperature of above 600 °C. Further experimental work showed a secondary-electron yield improvement of two orders of magnitude compared to an O-terminated surface.^{26, 109, 111} Finally, lithium-oxygen surfaces were found to be a "true" NEA, as confirmed by photo-electron yield spectroscopy, and air-stable, thus not undergoing surface transfer doping.¹²

From Group II, magnesium has been studied in detail. It shows similar adsorption energies and electron affinities to lithium at only 0.5 ML coverage.¹¹²⁻¹¹⁴ Using the thin film method on (100) diamond, it was shown to form a large NEA of -2.0 eV.^{113, 114} After annealing, the electron affinity did increase up to -0.9 eV, however. An advantage of magnesium is that Mg-surfaces are much simpler to manufacture than Li surfaces, as Mg is more reactive with the oxidised diamond. The one drawback is that despite being air and water stable, Mg-O terminations adsorb water vapour, among other atmospheric species.¹¹³ This results in a reduction of the NEA, although it can be almost entirely recovered using a vacuum anneal.¹²

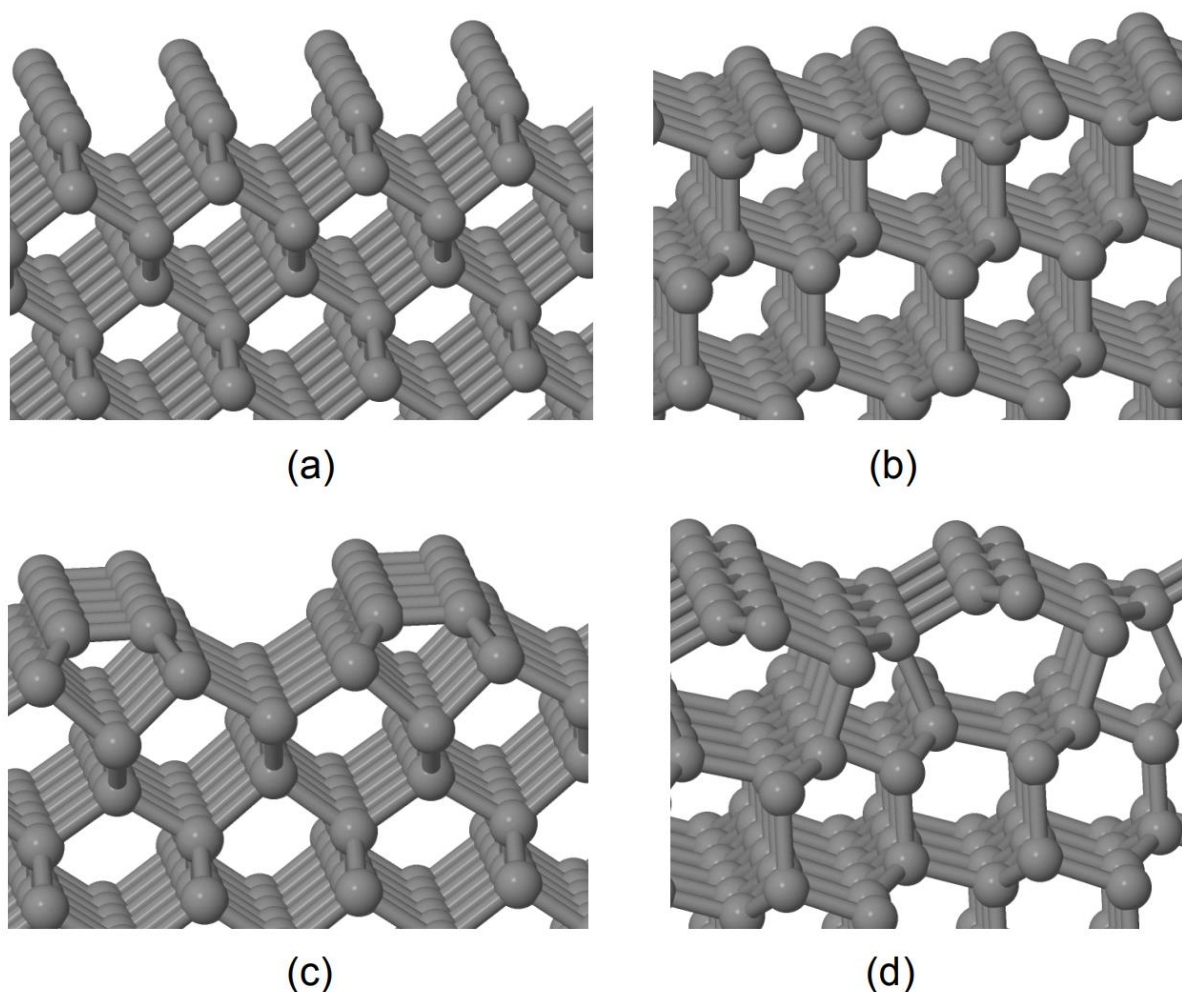


Figure 2.6: Simulations by James (2020) showing the (1x1) bare **(a)** (100) and **(b)** (111) diamond surfaces, and the (2x1) reconstructed **(c)** (100) and **(d)** (111) surfaces respectively. [26]

Electronegativity																	He				
H 2.2																B 2.0	C 2.6	N 3.0	O 3.4	F 4.0	Ne -
Li 1.0	Be 1.6														Al 1.6	Si 1.9	P 2.2	S 2.6	Cl 3.2	Ar -	
Na 0.9	Mg 1.3														Ga 1.8	Ge 2.0	As 2.2	Se 2.6	Br 3.0	Kr -	
K 0.8	Ca 1.0	Sc 1.4	Ti 1.5	V 1.6	Cr 1.7	Mn 1.6	Fe 1.8	Co 1.9	Ni 1.9	Cu 1.9	Zn 1.7	In 1.8	Sn 2.0	Sb 2.1	Te 2.1	I 2.7	Xe 2.6				
Rb 0.8	Sr 1.0	Y 1.2	Zr 1.3	Nb 1.6	Mo 2.2	Tc 2.1	Ru 2.2	Rh 2.3	Pd 2.2	Ag 1.9	Cd 1.7	Tl 1.8	Pb 1.8	Bi 1.9	Po 2.0	At 2.2	Rn -				
Cs 0.8	Ba 0.9	La 1.1	Hf 1.3	Ta 1.5	W 1.7	Re 1.9	Os 2.2	Ir 2.2	Pt 2.2	Au 2.4	Hg 1.9	Nh -	Fl -	Mc -	Lv -	Ts -	Og -				
Fr 0.7	Ra 0.9	Ac 1.1	Rf -	Db -	Sg -	Bh -	Hs -	Mt -	Ds -	Rg -	Cn -	Nh -	Fl -	Mc -	Lv -	Ts -	Og -				

Figure 2.7: Periodic table with each element's electronegativity values. [120] For an NEA surface to occur, the electronegativity value needs to be less than 2.6.

2.4.2.2. Transition Metals

The transition metals, specifically in the first row, are more electropositive than hydrogen so have also been investigated for the formation of NEA surfaces.^{97, 102, 115-120} Studies of thin metal layers onto bare diamond surfaces found that all metal layers studied showed characteristics of NEA surfaces when analysed using UV photoelectron spectroscopy (UPS).¹¹⁵⁻¹¹⁸ These works mainly focused on titanium, cobalt, nickel, copper, and zirconium. A titanium layer on a bare diamond surface was found to remain stable for temperatures up to 950 °C.¹²¹ In accordance with Equation 3, this means the emission current densities are doubled relative to a H-terminated samples, primarily due to the larger operating temperature range. Zr-terminated samples behaved similarly.¹⁵ As may be expected, the magnitudes of the NEA were found to be dependent on the transition metal used, and on the thickness of the deposited layer.

Metal-oxygen terminations have also been studied for transition metals. Cobalt and copper layers were deposited onto oxidised BDD, but these both exhibited a PEA. Zr-O-termination did result in an NEA, however.¹²² Vanadium deposited onto oxidised BDD lowered the work function to 3.8 eV, after deposition and annealing at 650 °C.¹²³ This corresponds to a small NEA of -0.47 eV. This same study also deposited vanadium onto oxidised N-doped diamond, discovering that no NEA was formed. In another study, chromium and titanium were deposited onto oxidised BDD using a thick film method.¹²⁴ The Ti-O- and Cr-O-diamond surfaces both formed stable surfaces up to the annealing temperature of 650 °C and formed an “effective” NEA and a “true” NEA, respectively. The annealing of the sample resulted in the work functions for both metals decreasing from 4.33 eV to 3.53 eV, and gave NEA values of -0.37 eV for the chromium system, and -0.54 eV for the titanium.¹²⁴ This corroborates theoretical calculations predicting high stabilities and NEAs for many transition metals.¹²¹ However, other research has shown that the electron affinity is still highly dependent on the adsorption site.^{119, 125}

NEAs are predicted for Ti, Ni, and Cu for both metal-diamond and metal-oxygen terminations. Vanadium and zirconium are only expected to form NEAs for the metal-diamond and metal-oxygen terminations, respectively.²⁶ The adsorption of carbide-forming transition metals, such as Ti and V, show larger adsorption energies, and consequently larger negative electron affinities. This is most probably due to the increased strength of the metal-carbon bonds formed.^{119, 126} These studies also show that the transition metals generally have much larger adsorption energies than H-terminated surfaces. They also demonstrate that NEAs are formed, but they tend to be less negative than the ones formed with group I or II metals.

2.4.2.3. Aluminium

Previous studies have predicted that aluminium will bond strongly to oxidised, nitrogenated, and bare diamond surfaces.¹²⁷⁻¹³⁵ Work by Lurie and Wilson discovered that aluminium deposition results in a surface reconfiguration to form a so-called (2x2) reconstruction.¹³⁰ This work also confirmed that aluminium forms a carbide, but that this occurred above 1000 °C, thus finding a window of c. 800 – 1000 °C where thermionic emission is probable. Aluminium deposited on O-terminated BDD and annealing at 650 °C resulted in a NEA of -0.42 eV and a corresponding work function of 3.61 eV.¹²⁴ Computational work was carried out on this, both by Beattie and James.^{26, 136} The study by Beattie

found that AlO-terminated diamond had NEAs of -2 eV to -3 eV for samples of (100) and (111) diamond in the Al₂O₃ configuration, respectively. A less negative NEA was found for higher ML coverages. The adsorption energy onto the bare diamond was found to be slightly exothermic with respect to the bulk. James completed similar computational work that built on a previous study where the electron affinities of the bare-, hydrogen-, and oxygen-terminated diamond surfaces were found to be 0.5 eV, -1.3 eV, and 1.7 eV respectively.⁸⁶ James used DFT to calculate the electronic properties of aluminium deposited onto bare, oxygen- and hydrogen-terminated (100) and (111) surfaces.²⁶ It was found that the most negative electron affinities occurred when oxidised diamond was used, as predicted by the bond dissociation energies, especially on ketone O-terminated diamond for (100) surfaces. Increased adsorption energies with respect to H-terminated diamond were shown to occur, suggesting that the studied systems had increased thermal stability compared to H-terminated diamond. However, these samples still had less negative EAs than equivalent systems using group I and II metals.¹³⁷ The computational results found by James for Al on oxidised diamond were consistent with experimental results from other studies.¹³⁶ Slightly more negative electron affinities were found but the same trends of increasing surface coverage resulting in decreasing adsorption energies and more positive electron affinities were observed. For the AlO-terminated surfaces, the largest NEA was found at 0.25 ML coverage. Bare diamond was also studied by James, and it was found that despite the larger NEAs, the decreased thermal stability relative to oxidised systems, made it less interesting for thermionic applications. Al deposition onto N-terminated diamond was also analysed but this showed extremely low adsorption energies, with (111) surfaces showing no adsorption at all. On the (100) surfaces, only a small NEA was discovered at 1 ML coverage.

2.4.2.4. Scandium

Scandium (Sc) is a brand-new metal for potential use in diamond surface terminations. A substantial proportion of the work with this metal, both experimental and computational, was carried out by the Bristol Diamond Group (at time of writing). An ab initio study of scandium terminations on (100) diamond looked at coverages of up to one ML of Sc on bare, oxygenated, and nitrogenated surfaces.¹³⁸ The structures of these bare surfaces were modelled using DFT (Figure 2.8), and found that the largest NEA values occurred at 0.25 ML coverage with magnitudes of -3.73 eV, -3.02 eV, and -1.75 eV for the oxygenated, bare, and nitrogenated surfaces, respectively. Importantly, these results predicted a thermally stable surface, making them very promising for thermionic emission applications. Similar computational work was also carried out by Zulkharnay,¹³⁹ who also studied (111) surfaces. Zulkharnay also experimentally studied Sc-terminated diamond, using Sc-terminations with 0.25 ML coverage for both (100) and (111) surfaces.^{139, 140} The samples were created by desorbing hydrogen from a diamond surface at high temperatures to create bare diamond surface. Next, Sc deposition was performed using electron-beam evaporation from a pure Sc rod at room temperature to achieve the desired ML coverage. Finally, the samples were thermally annealed in temperatures up to 900 °C, to chemically bond the scandium to the surface. Measurements were then taken under UHV. The resultant electron affinity values were -1.45 eV and -1.13 eV for the (100) and (111) surfaces, respectively, and can be seen in Table 2.1 with their corresponding work functions.

Table 2.1: Experimental data for scandium terminated diamond. φ and χ are the work function and electron affinity, respectively. Table adapted from work by Zulkarnay.¹³⁹

Termination	Surface	ML Coverage	φ / eV	χ / eV
C _d – H	(100)	1	3.49	-1.28
C _d – H	(111)	1	3.62	-0.96
C _d	(100)	-	4.94	0.53
C _d	(111)	-	5.03	0.68
C _d – Sc (deposited at RT)	(100)	0.25	4.33	-0.56
C _d – Sc (deposited at RT)	(111)	0.25	4.59	-0.24
C _d – Sc (after annealing at 900 °C)	(100)	0.25	3.22	-1.45
C _d – Sc (after annealing at 900 °C)	(111)	0.25	3.52	-1.13

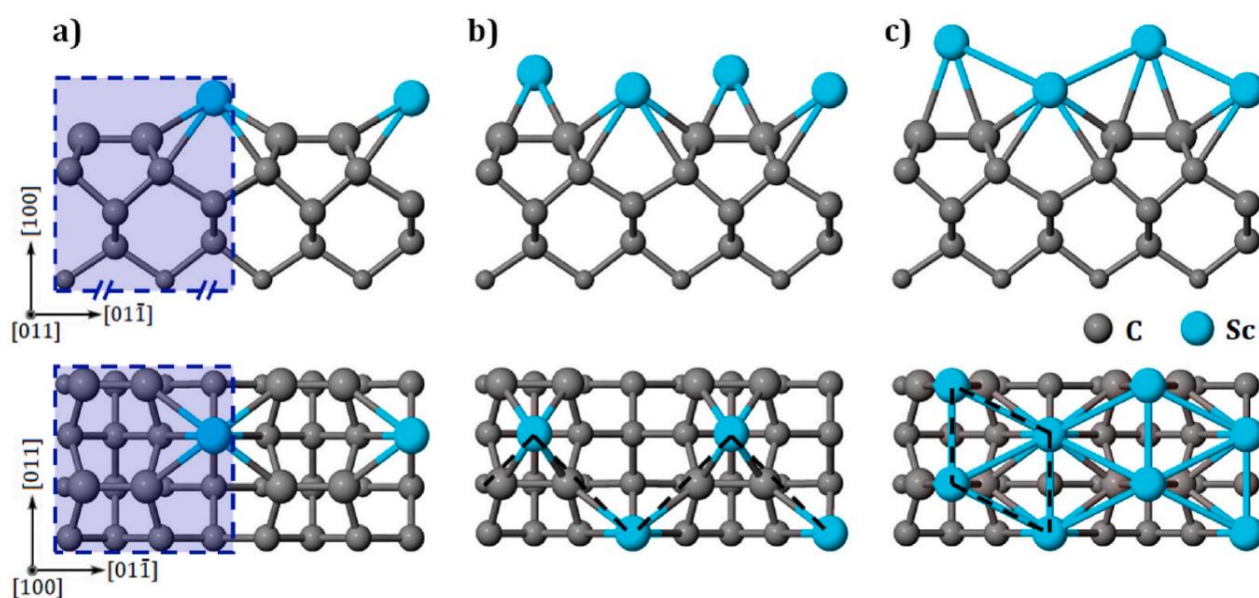


Figure 2.8: Side and top views of the Sc-terminated (100) bare diamond surfaces. All structures have been optimised for (a) – (c) 0.25, 0.5, and 1 ML coverage, respectively. The dashed blue box represents the (2x2) unit cell for 0.25 ML. The black dashed line is the 4 x 2 supercell in the zigzag and rhombus arrangement for the 0.5 ML and 1 ML coverages, respectively. These structures were computed by Zulkarnay. [138]

2.4.3. Metalloid Terminations

Experimental work on silicon has shown that it exhibits small NEAs when used to terminate (100) diamond.¹⁴¹⁻¹⁴³ When deposited, it results in a surface reconstruction of the (3x1) form, where carbon trimer chains are formed. An in-depth look at this type of surface reconstruction can be found in reference [144].¹⁴⁴ The termination is ordered if the silicon is deposited under vacuum and then annealed at high temperatures. This ordered surface has an NEA of -0.86 eV,¹⁴² and while not stable in air, can be further oxidised without losing its NEA.^{109, 141, 143} To my knowledge, no work has been carried out on the electron emission of silicon terminations at the time of writing this review. Earlier research has found however, that Si-terminated diamond has a potential for surface transfer doping when MoO₃ is used as the acceptor.¹⁰⁹

Germanium is deposited onto (100) diamond in a similar fashion to silicon, resulting in the same surface reconstruction.¹⁴⁵ However, germanium-termination becomes saturated at approximately 0.63 ML coverage. Ge-terminated diamond has an experimentally measured NEA of - 0.71 eV, slightly less negative than the Si-terminated surfaces.

2.4.4. Non-metal Terminations

2.4.4.1. Oxygen, Hydroxyl, and Carboxyl

Oxygen terminations have been widely studied both experimentally and theoretically. Theoretical studies have found positive electron affinities, and large ionization potentials, for O-terminated surfaces.^{91, 95, 96, 146} The two most common O-terminations are the “ketone” arrangement and the “ether” arrangement (Figures 2.9 (a) and (b)). For the more stable “ether” arrangement, a PEA of 2.6 eV was found through computational methods.⁹⁶ For (111) diamond surfaces, a theoretical study found that the maximum monolayer coverage was 0.5 ML due to steric hindrance at larger coverages.¹⁴⁷ This was disputed by Zheng et al. however,¹⁴⁸ leading to work by Loh et al. confirming that full ML coverage is possible experimentally by irradiating the sample with atomic oxygen at high temperatures.¹⁴⁹

Maier et al. experimentally created O-terminated surfaces to confirm the computational predictions for the electron affinities.⁸⁶ They found that the experimental PEA was lower than expected at 1.70 eV. They attributed this to residual hydrogen termination on the surface, which was unavoidable due to their use of an acid wash. As such, this electron affinity is said to be a “lower limit.” Shi et al. investigated O-terminated diamond for use in testing seawater salinity.¹⁵⁰ They used an O-terminated BDD electrode which showed a high sensitivity, due to its high potential window, and a good stability in sea water.

Oxidised diamond surfaces, due to their PEAs, have limited functionality outside of electrodes. They do provide a route to stabilise metal-terminations, however.¹⁰⁷ Due to the PEA of the oxidised diamond, a more electropositive metal is needed to achieve an NEA. Metals can bond with O-terminated diamond in multiple ways. They all share the characteristic partial oxidation of the metal, due to the metal-oxygen bond at the surface. Therefore, the metal’s tendency to oxidise further is reduced, resulting in a more air-stable surface. As stated, the O- termination can adopt a “ketone” or “ether” form. Both will allow the formation of MO-terminations. The relative proportions of the “ether”, “ketone” and hydroxyl groups on the surface depend on the oxidation methods used.¹²⁵ In

order for the metal to bond, a carbon-oxygen bond needs to break, potentially resulting in a surface reconstruction.

Hydroxyl-terminated diamond surfaces can be considered as metal-O-terminations with a hydrogen in the place of the metal.¹² The (100) hydroxyl-terminated surface has been modelled theoretically but no exact geometry was reported.^{96, 151} This led to computational work by Sque et al. where they attached -OH groups to the reconstructed (100) surface and used DFT to calculate relaxations from varying starting conditions.⁹⁷ Hydroxyl-terminated surfaces were theoretically found to be significantly more stable than the purely oxygenated surfaces, and the (100) hydroxyl surfaces were expected to find a small NEA. The exact magnitude of the electron affinity is currently debated as various theoretical studies have found values between -2.13 eV and -0.4 eV for the undoped (100) surface.^{83, 96, 97, 152, 153} Work by Larsson found an electron affinity of 0.3 eV for the undoped hydroxyl-terminated (111) surface.⁸³ As may be expected, they found that there is a large variation in these values depending on whether the sample is p- or n-type. The study found that boron doping resulted in electron affinities becoming more positive relative to undoped species, regardless of what the surface termination was. Similar results were found for the N- and P-doped samples, although it is noted that in case of nitrogen and phosphorus, the doping removed the possibility of PETE using visible light.

Experimental work by Yoshida et al. has shown that it is possible to create atomically flat (111) hydroxyl-terminated surfaces by annealing H-terminated diamond at temperatures greater than 500 °C in the presence of water vapour.¹⁵⁴ Yoshida et al. did not manage to demonstrate an NEA experimentally however, so could not confirm the theoretical NEA values. Carboxyl (-COOH) terminations are also possible but have not had as much coverage in the literature. It was shown to be possible by Falina et al. through anodisation oxidation in a Carmody buffer solution of a neutral pH,¹⁵⁵ and through the oxidation of nano- or nanocrystalline diamonds.^{100, 156} In the case of the latter two, this is due to the presence of exposed carbon, such as methyl groups, on the surface. It was later shown that it was energetically preferable to terminate both (100) and (111) surfaces with up to 0.5 ML coverage.¹⁵⁷ As expected however, the lowest carboxyl coverage, of 6.25%, resulted in the most desirable adsorption energies. Both hydroxyl- and carboxyl-terminated diamond have potential applications for drug delivery, biosensors, and bioimaging due to their ability to form amide bonds with amines in biomolecules.^{158, 159}

2.4.4.2. Nitrogen and Amines

Amine-terminations have been shown to be both theoretically and experimentally possible for both (100) and (111) surfaces. Most studies have focused on selective formation of primary amines (-NH₂), where 10-20% surface coverage is usually possible.¹⁶⁰⁻¹⁶² By introducing a 96:4 N:H mixture into the RF plasma at 5x10⁻³ Pa during the nitridation process, the substrate surface was shown to be "cleaned" by terminating any residual "dangling" bonds to form an amine terminated surface.¹⁵⁵ Tian and Larsson subsequently showed that it was possible to achieve 100% coverage with NH₂ species on both (100) and (111) surfaces.¹⁵⁷ However, while full coverage was possible, it was not found to be the most ideal adsorption situation. For the (111) and (100) surfaces, 6.25% and 43.75% coverage were found to be ideal, respectively. These amine-terminated surfaces can be functionalised using biomolecules with a similar mechanism to carboxyl-terminated surfaces. Amine-terminated diamond has also been shown to be better suited for catalytic breakdown of stable molecules than carboxyl-

terminated diamond, as it does not oxidise over time. This is because amine-terminated surfaces become protonated when immersed into HCl, resulting in primarily ammonium ($-\text{NH}_3^+$) groups.^{163, 164} It was found that both the amine and ammonium terminated surfaces show NEAs.¹⁶⁴

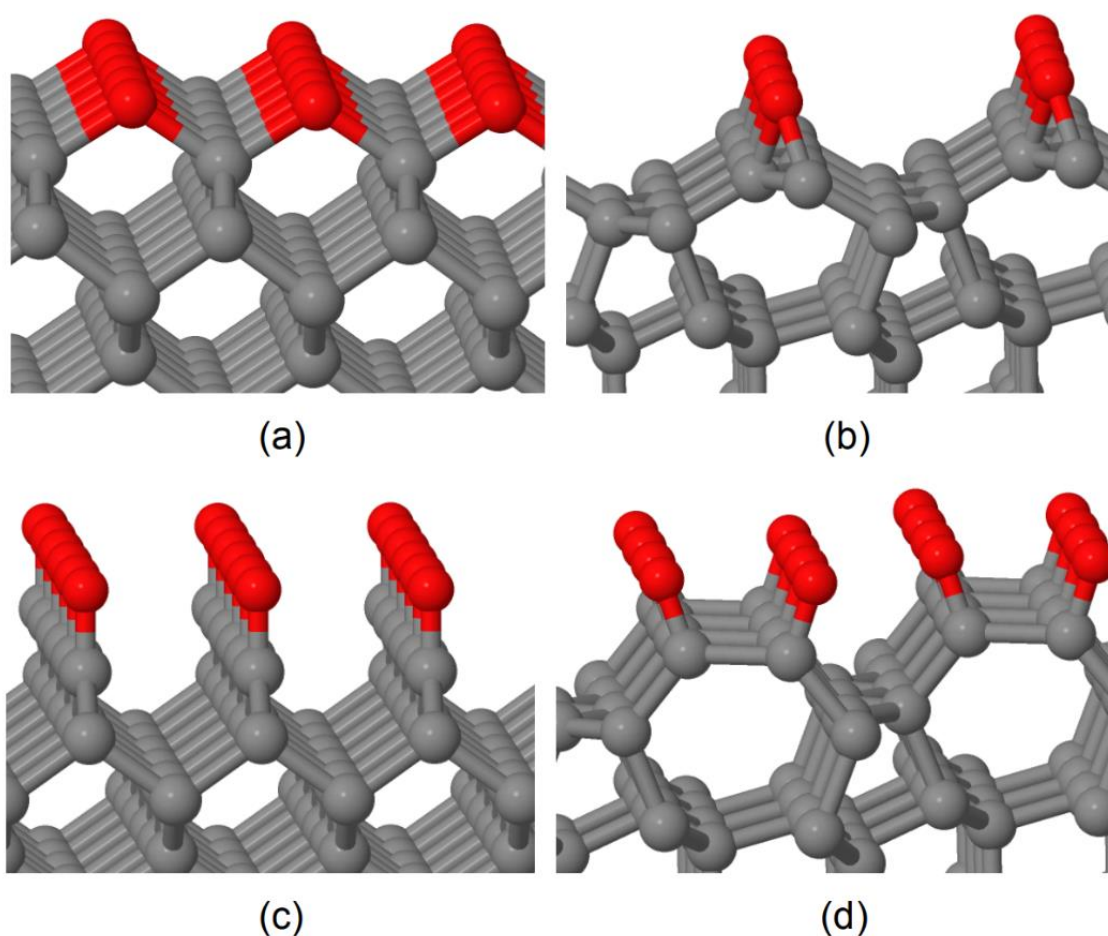


Figure 2.9: Simulations showing the ether-type **(a)** (100) and **(b)** (111) surfaces, and the ketone-type **(c)** (100) and **(d)** (111) surface O-terminations. Simulations by James. [26]

Theoretical calculations showed NEA values of -0.8 eV and -0.7 eV on undoped (100) and (111) amine-terminated species respectively, although these values changed significantly upon doping.⁸³ Finally, calculations by Fogarty reported a slightly larger range of -0.9 eV to -2.3 eV on (100) with varying surface coverage.¹⁶⁵ While RF and MW plasmas are one method of producing amine-terminated species, they can also be produced by reaction of chlorinated diamond with specific N-based species.¹⁶⁶

It is also possible to form a M-N-diamond structure in a similar fashion to the method that is used for the M-O-diamond structures. If the metal is sufficiently electropositive, the overall surface can still form a net NEA. One of the few studied examples is titanium. TiN-terminations have been theoretically shown to have comparable adsorption energies to amine-terminated surfaces but are significantly more stable.¹⁶⁵ The calculated electron affinities range from -1.7 eV to +1.8 eV meaning that at present no definitive NEA or PEA has been demonstrated for TiN-diamond surfaces. However, this potential remains for other metals that are currently untested. In theory, purely nitrogenated

surfaces, containing only N and C, have been calculated to have large PEAs between 3.2 eV and 4.7 eV but with low stabilities.^{121, 165} This is consistent with experimental work^{167, 168} In experimental studies, N-termination on both (100) and (111) surfaces can be achieved through radio or microwave plasma sources.^{49, 58} The type of N-termination achieved depends on the plasma temperature and pressure.¹⁶³ Adjustment of the plasma conditions can result in both primary (-NH₂) or secondary (C-NH-C) amine terminations, cyanide (C≡N), or imine (C=NH or C-N-C) terminations. A simulation of a C-N-C imine termination is shown in Figure 2.10.¹⁶⁹ Work by Chandran and Hoffman studied N-termination using an RF plasma in ultra-high vacuum. They found that after annealing this nitrogenated surface at 1000 °C, the surface nitrogen concentration was nearly equal to the surface atomic density of the (100) diamond substrate. Further analysis also showed that exposure to atomic hydrogen resulted in reformation of H-terminated diamond. While this early work could not find a quantitative value for the electron affinity, it did correctly predict a PEA with downward band bending for N-terminated surfaces. A later study looked at using this method for (111) diamond and found that the amount of nitrogen incorporation on the (111) surface was lower than for (100) surfaces under the same conditions.^{170, 171} Attrash et al. found that for (100) surfaces, some of the incorporated nitrogen was stable up to annealing of 1000 °C. This suggests a thermally stable, and ordered, nitrogen-terminated surface.

As computational studies found that surfaces grown would consist primarily of single substituted C-N terminations while some C-H bonds remained, Koch et al. and Yeh et al. then aimed to confirm their experimental results using a MW plasma and a pure nitrogen gas, in contrast to previous papers where nitrogen was introduced into a C/H gas mixture.^{161, 162} Other methods had attempted to reduce the surface damage associated with RF methods, but this resulted in mixed N-based termination species. The main benefit of these mixed samples is that they had little nitrogen loss at ambient temperatures.

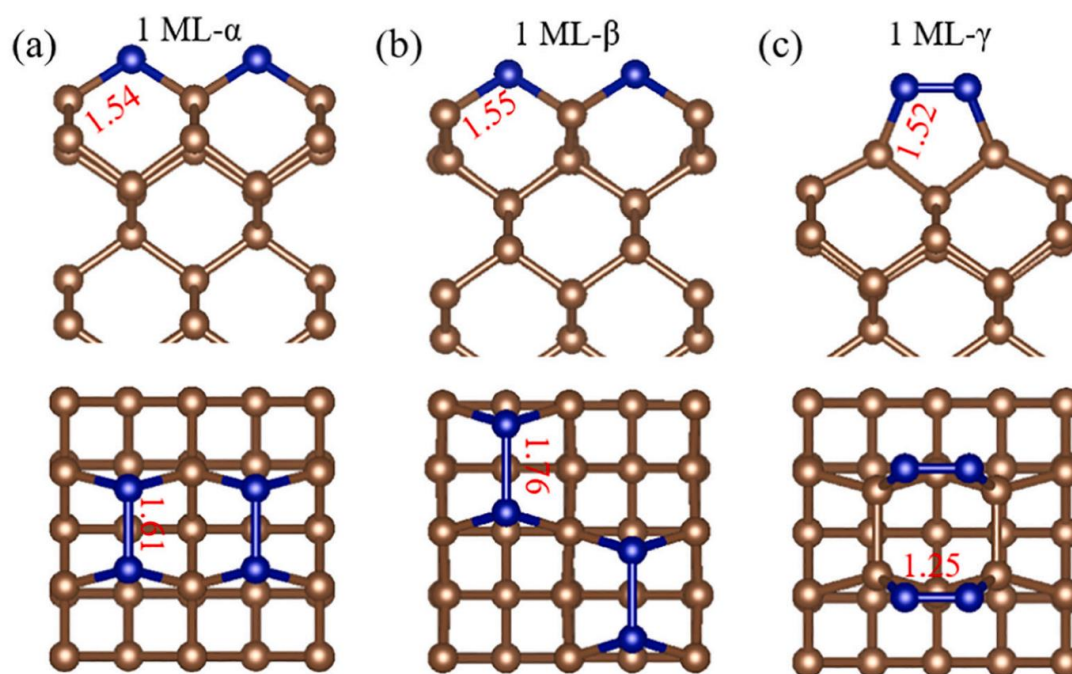


Figure 2.10: Simulated structure of C-N-C imine terminations at 1 ML coverage. Graphic by Gong et al. [169]

2.4.4.3. Sulphur and Thiol

Sulphur will bond to diamond as a thiol (C-SH) group. This has been achieved in two separate ways. UV radiation can be used to ionise H₂S gas to deposit thiol-terminated diamond,¹⁷² or hydroxyl-terminated nanodiamond can be reacted with thiourea in acidic conditions.¹⁷³ Simply using UV radiation and sulphur with H-terminated diamond results in both thiol and thiocarbonyl (C=S) groups.¹⁷⁴ Despite the inconsistent termination groups, both are promising for biomedical applications as all sulphur-containing groups can bind gold nanoparticles to their surface.^{173, 174}

2.4.4.4. Halides

Halides preferentially terminate onto the reconstructed (100) surface,¹²⁶ and onto the (111) surface without reconstruction.¹⁷⁵ Studies have been carried out for terminations with fluorine, chlorine, and bromine. Fluorination is straightforward, as any deposition involving fluorine-based gases or plasmas will result in fluorine termination. In many cases however, the surface was roughened beforehand. The use of SF₆ plasma, or thermally inducing the dissociation of XeF₂, have been demonstrated to form a monolayer on (100) diamond with minimal surface damage.^{176, 177} As can be seen in Figure 2.7, fluorine is the most electronegative element, and therefore would theoretically form the highest PEA when used for termination of diamond. This has been experimentally measured to be 2.56 eV for F-terminated BDD.¹⁷⁷ Typically, fluorinated surfaces are not associated with electronic applications due to these high PEAs. However, research has shown that fluorination of diamond hinders hydrogen evolution on BDD electrodes,¹⁷⁸ which could improve the electrodes' lifetime, function, and potential window. For biological applications, it can reduce the degree of non-specific binding in biosensors and,¹⁷⁹ in the case of F-terminated nanodiamond, may also be used for bioimaging.^{180, 181} Chlorination of diamond can be achieved by ionising chlorine gas using UV light.⁵ It was found that shorter irradiation times and lower pressures resulted in maximised surface coverage.¹⁷² However, it has been shown theoretically that full monolayer coverage is not achievable with chlorine through this method.^{126, 175} Similarly, bromine has been theoretically shown not to be stable above ~0.25 ML coverage.¹⁸² Therefore, Cl- and Br- terminations have been primarily used as an intermediate for further terminations. Amine and thiol terminations have been experimentally produced through a photochemical reaction of bromine- and chlorine-terminated diamond.^{172, 183} Further, by using a Grignard reaction, a wide range of aliphatic terminations can also be achieved.^{184, 185}

2.4.4.5. Aliphatics and Aromatics

Using UV light, many alkyl and aromatic groups can be directly bonded to the surface of the diamond film. This has been shown for functionalised alkenes with various halide, nitrogen- and oxygen-based groups.¹⁸⁶ It was also demonstrated that electrochemically active groups can be attached covalently to diamond.¹⁸⁷⁻¹⁹⁰ Aromatics can be attached to diamond through the reduction of diazonium salts, first shown by Kuo et al. who used nitrophenyl and trifluoromethylphenyl to attach to BDD.¹⁹¹ This technique has since been adapted to allow a large range of functional aryl species to be added to diamond surfaces. These functionalised aryl and aromatic species can be used to make biosensors or bioelectronics.

For both aliphatic and aromatics, radical anionic species are created through electron injection. For alkenes this is through the absorption of UV and the emission of high energy electrons,¹⁹² whereas

diazonium salts easily form anionic species if a small bias is applied at a BDD electrode, producing nitrogen gas.¹⁹³ The inclusion of -COOH or -NH₂ groups allow the attachment of biological molecules; either through a direct reaction, or alternatively, by employing a crosslinking species.¹⁹⁴⁻¹⁹⁸ Even fullerenes can be attached to diamond through Suzuki coupling of bromine-based groups.¹⁹⁹ Similarly, conjugated aromatic species are applied to dye-sensitised solar cells.²⁰⁰ A so-called the Diels-Alder reaction can be used to create a clean diamond surface of C=C dimers. This reaction has been used to attach aromatic groups to nanodiamond.²⁰¹ For example, a diene such as 1,3-butadiene, can be attached that enhances secondary electron emission as this surface possesses a greater NEA than H-terminated diamond.²⁰²

2.5. Concluding remarks

This review of relevant literature has provided the necessary theoretical background of the thermionic emission process as well as a detailed coverage of dopants used on manufactured diamond and a discussion of diamond surface terminations with various species, along with some discussion of their potential uses in thermionic emission devices. Particular focus in current research, and indeed also in this dissertation study, is on termination with hydrogen due to the electrical properties shown both computationally and experimentally. Hydrogen terminations have been experimentally shown to give undoped diamond an electron affinity with a magnitude between -0.7 eV and -1.3 eV for both the (100) and (111) surfaces.^{86, 91-94} Computational studies using Density Functional Theory (DFT) models have predicted that values of approximately -2 eV should theoretically be possible.⁹⁵⁻⁹⁷ This should correspond to electron emission from H-terminated diamond starting below 600 °C, with the emission current density increasing with temperature, until, unfortunately, till c. 700 °C, when most of the hydrogen layer will desorb from the surface. Further research has indicated that there can be a decrease in the peak emission current as the temperature is cycled.⁵⁷ As the number of cycles increases, the threshold temperature for thermionic emission also increases meaning that, after several cycles, a higher temperature is needed for thermionic emission to occur. By using suitable dopants when depositing the diamond, further control of the electrical properties should be possible, increasing the feasibility of diamond use in TEC devices for energy generation. Therefore, this study will aim to establish if this also applies to doped diamond samples. Specifically, the objectives of the present study are to characterise the doped diamond surfaces using various characterisation techniques, examine how different types (undoped, BDD, PDD, NDD), and different concentrations of doping (for the PDD samples) of prepared H-terminated diamond films affect the thermionic emission characteristics, and determine the effective work function of the samples through the use of the Richardson-Dushman equation.

3. Methodology

3.1. Samples

To investigate if and how the thermionic emission characteristics of hydrogen-terminated diamond change when different types and different concentrations of dopant are used, the following were prepared: one undoped diamond sample, three phosphorus-doped diamond (PDD) samples, two nitrogen-doped diamond (NDD) samples, and one boron-doped diamond (BDD) sample (see Table 3.1). The PDD samples, with varying phosphorus concentrations (see Table 3.1), were supplied by the Institute of Physics of the Czech Academy of Sciences as large wafers (12" diameter). They were cut into squares to fit the 10 x 10 mm molybdenum substrates that were used in this study. The undoped, NDD, and BDD samples were all grown in the Bristol laboratory using CVD. The undoped and NDD samples were deposited on the molybdenum substrates using a homebuilt, 2.45 GHz ASTeX-type MWCVD reactor,²⁰³ powered by a 2 kW Sairem Power Supply. The BDD sample was grown in a homebuilt HFCVD reactor. In this reactor, the gaseous species are activated using resistive filaments that are heated using high currents and voltages.^{203, 204} Detailed descriptions of both HFCVD and MWCVD reactors can be found in in sections 9.1.1. and 9.1.2., respectively.

Table 3.1: Sample specifications.

Sample Name	Dopant	Dopants per cm ²	Deposition Method
N4	Nitrogen	Unspecified	MWCVD
N5	Nitrogen	Unspecified	MWCVD
N21134	Phosphorus	c. 16k	Supplied
N21136	Phosphorus	c. 63k	Supplied
N21139	Phosphorus	c. 250k	Supplied
B1	Boron	Unspecified	HFCVD
Undoped	N/A	N/A	MWCVD

3.2. Substrate preparation

3.2.1. Manual abrasion and seeding

Preparation of the molybdenum substrate is critical for successful diamond deposition. The initiation of diamond growth can sometimes be slow, particularly if there are no carbon-containing species to propagate from. Substrates are therefore often "seeded", which involves the implantation of carbon or microdiamond into the top few layers of a substrate. There are several methods to do this but in this study manual abrasion was used as the used substrate samples were not atomically flat, and because molybdenum as a material is too hard for effective seeding using other techniques.²⁰³ Manual abrasion is a simple but time-consuming procedure. For each abrasion, two molybdenum samples were cleaned with methanol and then dried. A small amount of microdiamond powder (1 - 3 μm in diameter, supplied by Van Moppes) was then deposited onto one of the samples. The other sample was subsequently placed on top with the polished surfaces facing each other with the microdiamonds in between. The two molybdenum samples were then rubbed together to scratch the surface and to embed the microdiamonds. This type of abrasion/seeding increases the nucleation of the diamond in two ways: by implantation of microdiamonds in the substrate surface, and by texture-

roughening of the substrate surface through scratching. The scratching of the surface increases the number of sites (or facets) where diamond can start growing from. There is a possible downside with this method in that it can result in “boulder-like” structures on the surface if microdiamond particles remain on the abraded surface (see Figure 4.8).

3.2.2. Grating

The use of the thermionic emission simulator (TECsim; see sections 4.3 and 9.2.3) also required the laser-etching of a vertical “grating” into the back of the substrates (before and after shown in Figure 3.1). This grating, needed to improve the absorption of the laser light in the TECsim analysis, was achieved using an Alpha 532 laser system (Oxford Lasers Ltd.; wavelength of 542 nm, maximum power of 5 W at 10 kHz; pulse duration of 10 - 15 ns). The grating separation was programmed at 10.6 μm to match the amplitude of the TECsim laser. Further details of the procedure can be found in reference [205].²⁰⁵

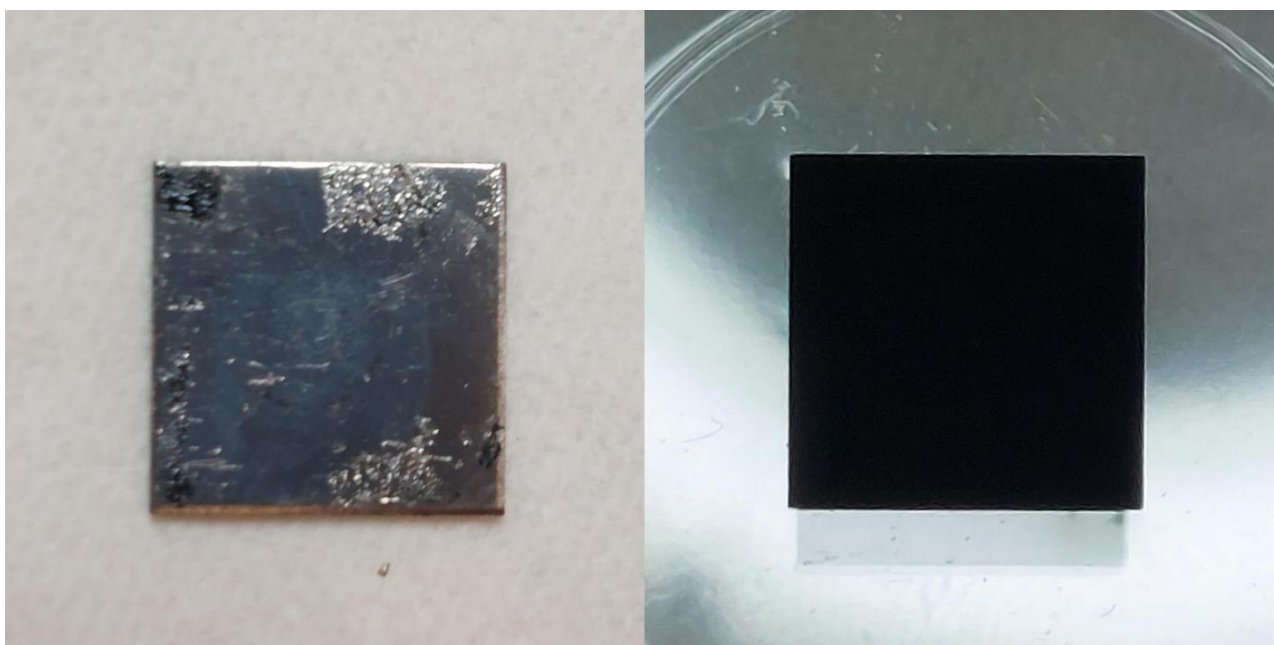


Figure 3.1: Reverse side of the 10 x 10 mm molybdenum substrate **(left)** before and **(right)** after laser etching. The sample on the left appears ‘dirty’ due to glue residue remaining on the back of the substrate after a layer of masking tape had been removed prior to diamond deposition. The surface on the **(right)** appears black due to the small grating separation.

3.3. Experimental Growth Conditions

In this study, only the undoped, BDD, and NDD samples required deposition as the three PDD samples were supplied by the Institute of Physics of the Czech Academy of Sciences and ready-to-use. Each of the other samples was grown on a carefully prepared 10 x 10 mm molybdenum substrate. The growth conditions for the undoped and NDD samples, deposited in the MWCVD reactor, and the BDD samples, deposited in the HFCVD reactor, can be found in Table 3.2. The gas concentrations (in standard cubic centimetres per minute; sccm) were controlled using so-called mass flow controllers (MFCs). In the case of the BDD sample, no boron-based species were used as a residual doping

method was used to keep the dopant concentration relatively low. Whilst the quality of the undoped and BDD samples was generally very good, the film quality for the NDD samples was mixed, and some of the samples that were prepared (N1, N2, and N3; not listed in Table 3.1) could only be used to tune and adjust the final and optimal growth conditions of the NDD diamond film. Consequently, only samples N4 and N5 were included for further analysis. Some attempts to make NDD samples resulted in “boulder-like” inclusions on the surface, or incomplete coverage. SEM images of sample N4 provide a good example of why the samples with such “boulders” were discarded for thermionic emission analysis, see below: Figure 4.8). Sample N5, which exhibited delamination before it could be tested for thermionic emission, was expected to show interesting emission characteristics, which is why it was included for both Raman and SEM analysis, but again excluded for thermionic analysis (see Sections in 9.2 for detailed information about the methods).

Table 3.2: Growth conditions for the **(left)** undoped and nitrogen-doped samples deposited in the MWCVD reactor and **(right)** the boron-doped samples in the HFCVD reactor.

MWCVD Growth Conditions		HFCVD Growth conditions	
Microwave Input Power (W)	1050	Filament Power (W)	255
Microwave frequency (GHz)	2.45	Filament Material	Tantalum
Gas pressure (Torr)	150	Filament length (mm)	70
H ₂ flow (sccm)	300	Heater power (W)	16
CH ₄ flow (sccm)	12.5	Gas pressure (Torr)	20.29 Torr
N ₂ flow (sccm) (NDD only)	4.0	H ₂ flow (sccm)	200
Spacer wire thickness (mm)	8	CH ₄ flow (sccm)	2.00
Growth area (mm ²)	10 x 10	Growth area (mm ²)	10 x 10
Growth rate (μm h ⁻¹)	2 - 5	Growth rate (μm h ⁻¹)	0.5

3.4. Characterisation

Three techniques were employed in the characterisation of the samples. First, *Raman spectroscopy* was used to analyse and identify structures in the top few atom layers of the diamond samples, and to determine the type of crystallinity. The type of crystallinity can be indicated by the presence of a specific peak present only for nanodiamond samples. In this study, a Renishaw 2000 Raman spectrometer (laser wavelength of 514 nm) was used to create the spectra (static and extended scans, see below). In simple terms, the Raman spectrometry method involves laser light incident on the sample surface, interacting with the molecular bonds of the surface species. This interaction results in a shift in the wavelength of the reflected and refracted laser light. The resultant spectra were analysed using Originlab™ software,²⁰⁶ which allowed the characteristic peaks to be assigned specific (literature) values, as well as the characterisation of the surface structure. Whereas Raman spectroscopy can also be used to obtain quantitative information about the peaks, for example, the full-width half-maximum (FWHM), the main focus of this study was on the position of the peaks in order to characterise the surface of the diamond film. The Raman spectra were therefore used here to identify the nature of the characteristic peaks only. Further details on Raman spectroscopy can be found in Section 9.2.2.

The second technique, *scanning electron microscopy (SEM)*, was used to visually corroborate the surface character and structure suggested by the Raman spectral analysis. In simple terms, this technique involves an electron beam targeting the diamond sample using an array of electromagnetic

lenses. Upon hitting the diamond surface, the electrons scatter and result in the release of secondary electrons, which are then 'collected' in a detector and used to reconstruct the characteristics of the surface. The image is built point-by-point by measuring the positions and the intensities of the secondary electrons. The resulting 2D SEM image has a resolution of c. 50 nm. These high-resolution images could then be analysed using Image J software to describe the diamond surface characteristics and to determine the mean grain size.²⁰⁷ More information about SEM can be found in Section 9.2.1.

To determine if thermionic emission occurred in any of the samples, they were analysed in the home-built *Thermionic Emission Converter simulator (TECsim)*, which is the third and final characterisation method used in this study. The simulator makes use of an infrared CO₂ laser (wavelength 10.6 μm , maximum power 40 W; Synrad FSV40KFD, Firestar) to heat the diamond samples, and to induce the thermionic emission current. The collector in the TECsim is cylindrical (10 mm diameter) and made of tungsten, although other materials and sizes can also be used.¹³⁹ The sample/collector system in the TECsim is connected to a DC power supply (HY3003D) and an ammeter (Keithley Model 2750), which is capable of measuring emission currents with an accuracy of $\pm 0.01 \mu\text{A}$. For the diamond samples in this study, a saw-toothed cycle was used to measure the thermionic current between 300 °C and 750 °C (applied negative (forward) bias of approximately 25 V; see Figure 3.2).

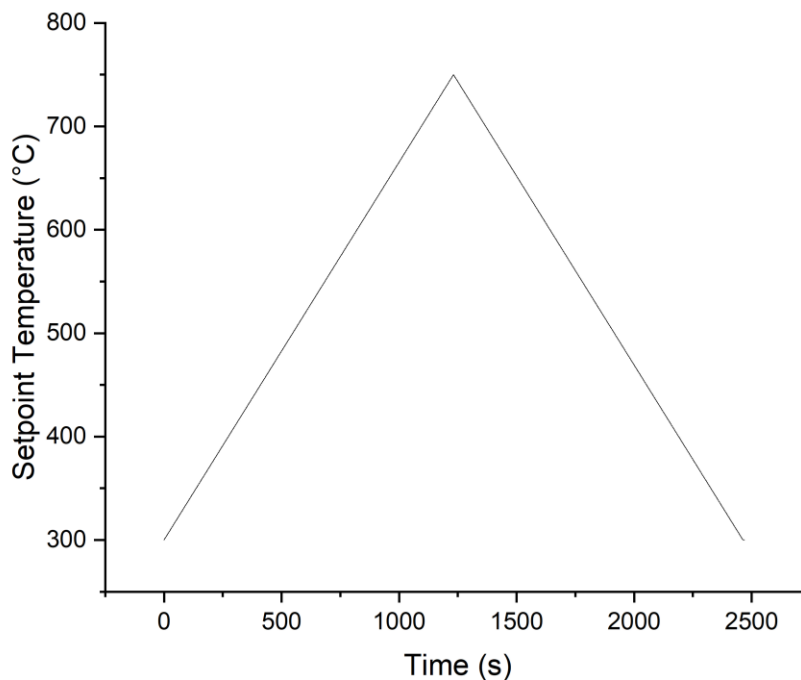


Figure 3.2: The saw-tooth temperature cycle used for all thermionic test analyses. The graph shows the duration of the cycle in which the system reaches its peak temperature of 750°C after c. 20 minutes.

4. Results

4.1. Raman Spectroscopy

Two Raman spectra were taken for all samples initially: a static scan for Raman shifts between 600 and 2000 cm^{-1} , and an extended scan for Raman shifts between 100 and 5000 cm^{-1} . The range of the static scan was chosen so that it was centred around the expected diamond peak at 1332 cm^{-1} ,²⁰⁸ and that it would also capture another expected peak for all samples, the so-called 'G' band at c. 1550 cm^{-1} .²⁰⁹ The extended scan was chosen to capture any peaks outside the range of the static spectrum, but particularly in the higher values, i.e. above 2000 cm^{-1} . All major spectral peaks identified were assigned using Originlab™.²⁰⁶

Figure 4.1 shows the static and extended spectra for the undoped sample. The two peaks found for this sample, a sharply defined **X** and a broad and less distinctive **Y**, are the spectral peaks that correlate with literature values for diamond and graphitic grain boundaries respectively.^{208, 209} These peaks needed to be identified early to allow for characterisation of the doped species. In the static spectrum, there is a distinctive trough at c. 1680 cm^{-1} , which is due to equipment error. It is suspected that one of the internal mirrors is slightly misaligned/has an error which results in light being refracted incorrectly. It can be observed on every Raman spectra taken in this study but will be further ignored. The apparent peaks near the end of the extended spectrum for the undoped sample (at c. 3900 cm^{-1} and 4800 cm^{-1}) can be explained by the lack of sample thickness. It is proposed that they are caused by the light penetrating through the diamond layer onto the molybdenum substrate. This then results in extreme, incorrect oscillations in the measured intensities. In the extended spectrum, the start of the baseline is abrupt, and this can be seen in all extended spectra for all samples. This is an artificial effect that can be attributed to the equipment. It is noted that the units for the signal on the vertical axis in this, and all other diagrams, are arbitrary, i.e., spectral intensity is unitless.

Figure 4.2 shows the spectrum for BDD, the boron-doped sample (B1). The X and Y peaks are present again, but no other meaningful peaks could be identified for this sample. While the diamond peak **X** is as distinctive as in the undoped sample, the 'G' band peak **Y** in the BDD sample is a lot less pronounced. A little experiment was run for this sample to investigate the influence that overhead lighting in the laboratory may have on the spectral output. A small peak was observed at c. 3050 cm^{-1} with the light on, which disappeared when the lights were switched off (position **Z** in Figure 4.2(bottom)). To avoid this interference, all other spectra were taken in the dark.

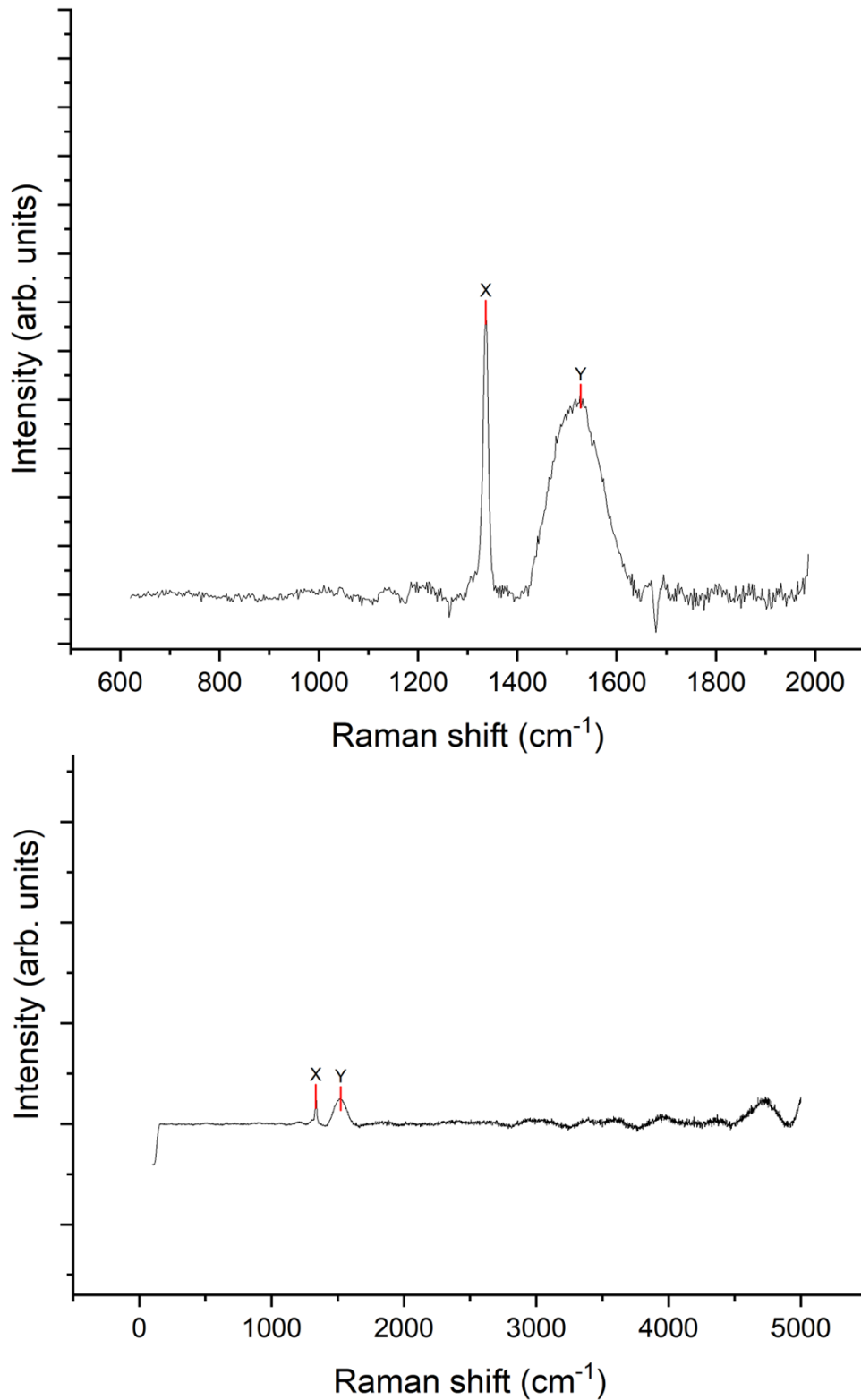


Figure 4.1: (top) Static Raman spectrum and **(bottom)** extended Raman spectrum for the undoped diamond sample. **X** – diamond peak at 1332 cm⁻¹ and **Y** – ‘G’ band at 1550 cm⁻¹. Note the dip at 1680 cm⁻¹ in the static spectrum **(top)**(explained above). The peaks observed on the far right of the spectrum are not of note as they are simply caused by interactions with the molybdenum substrate through the diamond layer.

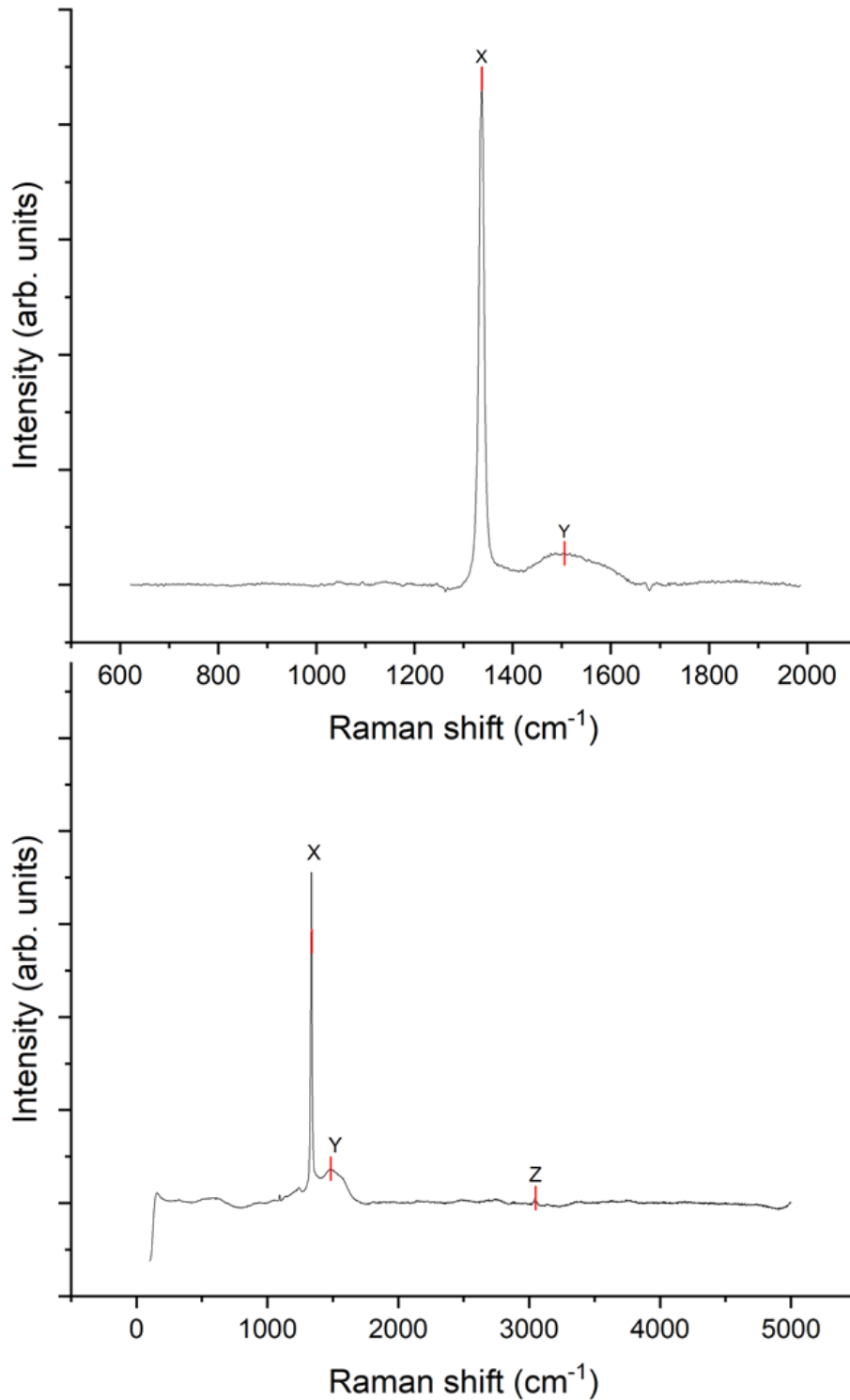


Figure 4.2: (top) Static Raman spectrum and **(bottom)** extended Raman spectrum for the BDD sample (B1). **X** – diamond peak at 1332 cm⁻¹, and **Y** – ‘G’ band at 1520 cm⁻¹. **Z** in the extended spectrum shows the position of the small peak that was distinctive in the spectrum run when the overhead lighting in the laboratory was switched on. The spectrum displayed here is when the lights were switched off.

Figures 4.3 and 4.4 show the spectra for the nitrogen-doped (NDD) sample (N5) and phosphorus-doped (PDD) sample (N21134), respectively. The diamond (**X**) and 'G' band (**Y**) peaks are again present and distinctive. In Figure 4.4, the graphitic peak (**Y**) is higher than the diamond peak (**X**). This indicates a high coverage of graphitic, sp^2 carbon on the surface. However, the intensity of peak **Y** on a Raman spectra is increased by a factor of 50, when compared to the actual surface coverage. Hence, despite the large intensity of the **Y** peak, the actual surface coverage is lower. The static spectra for both NDD and PDD samples exhibit peaks at approximately 1150 cm^{-1} (labelled **A**), $1370 - 1450\text{ cm}^{-1}$ (labelled **B**), as well as peaks at around 2900 cm^{-1} (Peak **C**), and in the range $4200 - 4500\text{ cm}^{-1}$ (Peak **D**) which were not seen for the undoped or BDD samples. In the NDD spectrum, the peaks **A** and **B** are narrow, high, and sharply defined, whereas in the BDD spectrum, they are less distinctive. An interesting observation was that the NDD and PDD samples showed larger wavelength shifts than the BDD and undoped diamond samples. The BDD sample also showed less noise than the NDD and PDD samples, due to the thicker diamond layer on the sample.

The broad peaks labelled **C** and **D** on the NDD and PDD spectra were unexpected. In order to determine their nature, the extended spectra of the three H-terminated PDD samples were overlaid to assess if the phosphorus doping concentration (see Table 3.1) played a role in the peak intensity (Figure 4.5). The **C** peak appears to be highest for the lower two doping concentrations, while the effect for the **D** peak is less straightforward. Here the lowest and highest doping concentrations seem to have resulted in a lower peak intensity. All in all, the middle concentration sample N21136 (c. 63k dopants per cm^2) seems to have resulted in the most pronounced signals. Another interesting observation is that there are shifts in the position of the peaks. While the values of the two lower dopant concentration samples are relatively close, the highest dopant concentration sample N21139 (c. 250k dopants per cm^2) occurs $200 - 300\text{ cm}^{-1}$ 'later'. To investigate the **C** and **D** peaks further, the Raman spectra of the PDD samples were repeated after thermionic testing as it is a well-documented phenomenon that surface hydrogen desorbs from a diamond surface at temperatures exceeding $700\text{ }^\circ\text{C}$.^{31, 210-213} Therefore, after thermionic testing there should be less hydrogen species on the surface, meaning a reduction in the intensities of peaks **C** and **D** will be seen. Theoretically, the amount of desorption seen should be consistent for all samples allowing for a more accurate determination of the relationship between the doping concentration and the intensity of the **C** and **D** peaks. Figure 4.6, which shows the overlaid spectra for the post-thermionic emission spectra, shows a clear negative trend in the intensity of the **C** peak's intensity with respect to the dopant concentration. The **D** peak was no longer observed for any sample after thermionic analysis had occurred, indicating that the **D** peak especially was dependent on the hydrogen termination. For both the peaks, a clear reduction was seen from before thermionic analysis, however. The trends for the peak positions were the same as occurred for the samples before thermionic analysis. The **C** peak position for the samples N21134 (c. 16k dopants per cm^2) and N21136 (c. 63k dopants per cm^2) occurred at the same shift, whereas for the sample N21139 (c. 250k dopants per cm^2) occurred at a higher shift.

Finally, the spectra obtained for each individual PDD sample was compared before and after thermionic emission. Figure 4.7 shows the example spectra for one of the samples (N21139) as each sample showed a similar trend. The further spectra can be found in Section 9.3.1. One of the key observations is that the **X** and **Y** peaks before thermionic analysis have a larger separation than after thermionic analysis (peaks **X*** and **Y***). Other than this, the overall shape of the combined peaks in the range $1100 - 1600\text{ cm}^{-1}$ remains largely the same. Again, it can be seen that the peaks at **C** and **D** are significantly lower in magnitude.

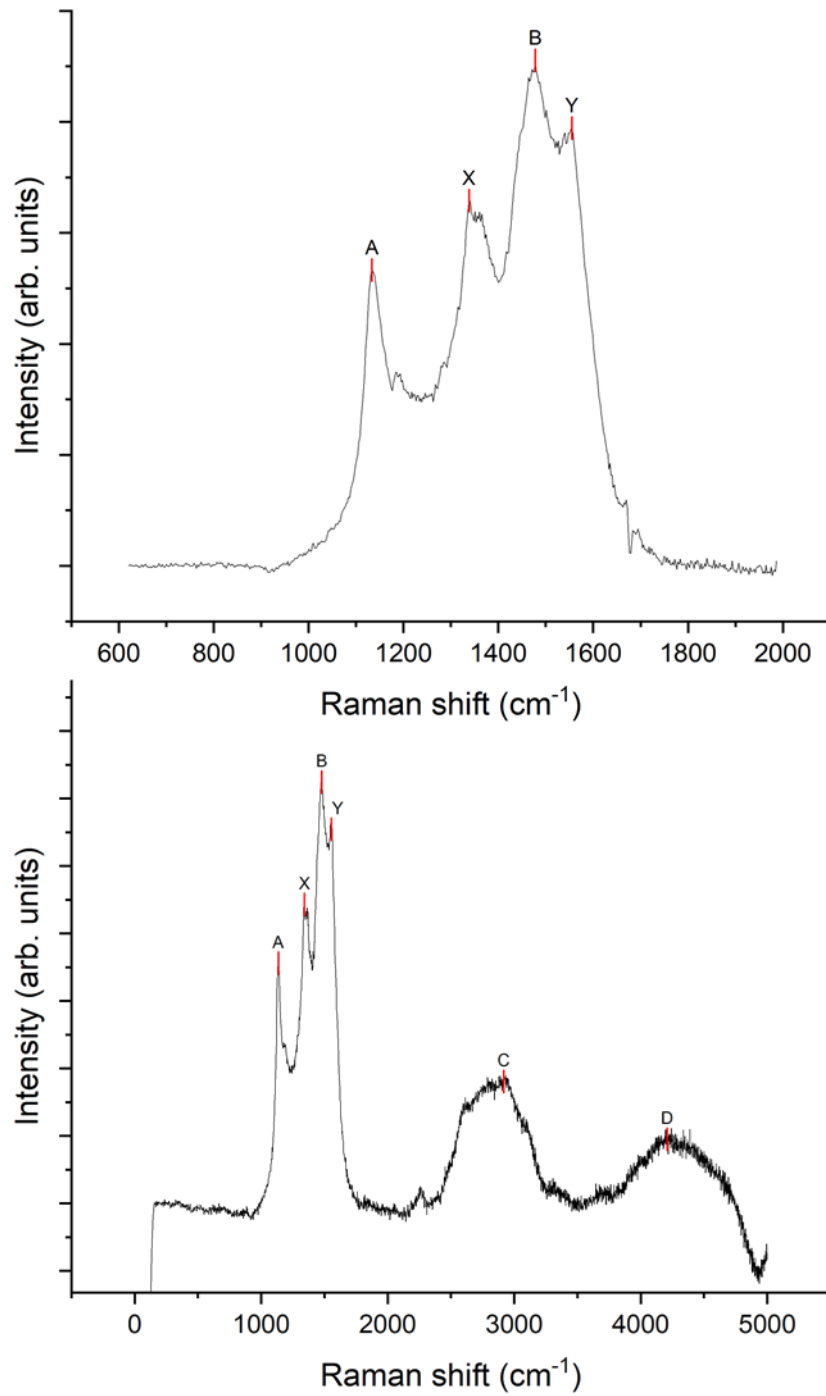


Figure 4.3: (top) Static Raman spectrum and **(bottom)** extended Raman spectrum for the NDD sample (N5). **X** – diamond peak at 1332 cm^{-1} and **Y** – ‘G’ band at 1550 cm^{-1} . Characteristic peaks were also identified at 1150 cm^{-1} (**A**), 1440 cm^{-1} (**B**), 2900 cm^{-1} (**C**), and 4200 cm^{-1} (**D**). For details, see main text.

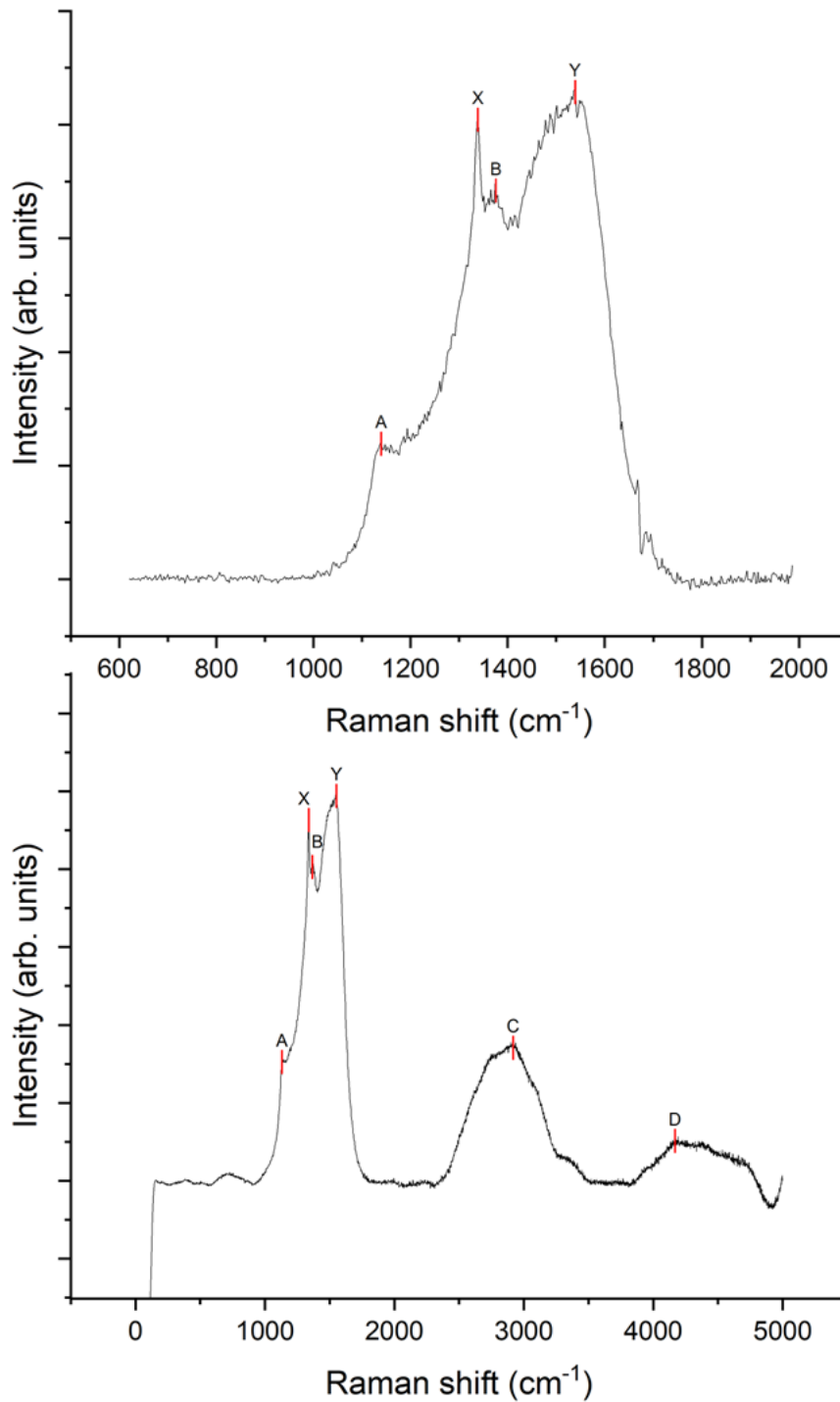


Figure 4.4: (top) Static Raman spectrum and (bottom) extended Raman spectrum for a PDD sample (N21134). X – diamond peak at c. 1338 cm^{-1} and Y – ‘G’ band at 1540 cm^{-1} . Characteristic peaks were also identified at 1150 cm^{-1} (A), 1340 cm^{-1} (B), 2900 cm^{-1} (C), and 4200 cm^{-1} (D). For details, see main text.

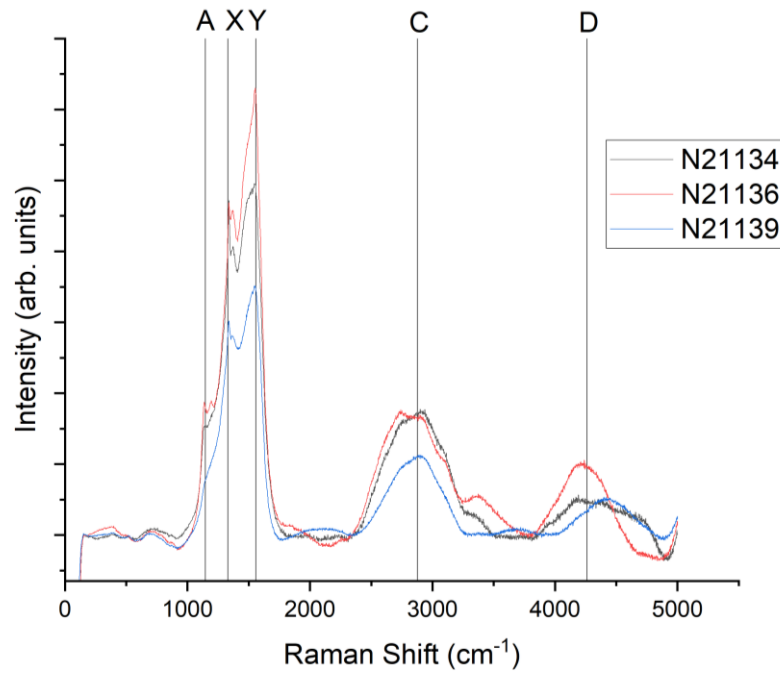


Figure 4.5: Extended Raman spectra for the PDD samples pre-TECsim analysis. **X** – the diamond peak at c. 1338 cm^{-1} and **Y** – the ‘G’ band at 1540 cm^{-1} . The peaks labelled **A**, **C**, and **D** occur at 1130 cm^{-1} , in the range 2800 - 2900 cm^{-1} , and 4100 - 4500 cm^{-1} , respectively. In general, the intensity of the peaks for N21136 were higher than for the other samples and occurred at shorter wavelength shifts. Further details in the main text.

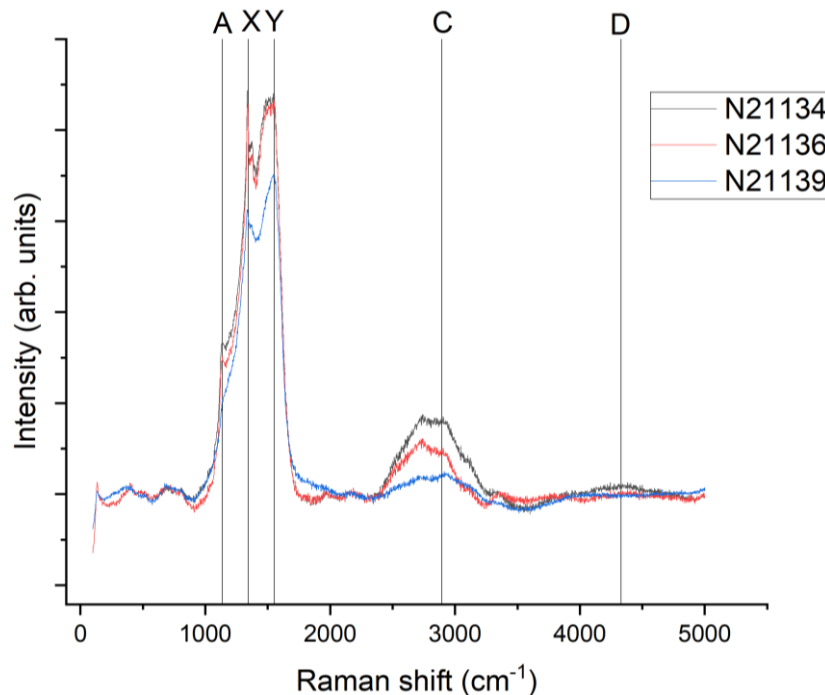


Figure 4.6: Extended Raman spectra for the PDD samples post-TECsim analysis. **X** – the diamond peak at c. 1338 cm^{-1} and **Y** – the ‘G’ band at 1540 cm^{-1} . The peaks labelled **A**, **C**, and **D** occur at 1130 cm^{-1} , in the range 2700 - 2900 cm^{-1} , and 4100 - 4500 cm^{-1} , respectively. The peaks at **C** show a negative trend with regards to the dopant concentration. Note that no peaks are observed at **D** post-thermionic emission analysis that were observed before testing.

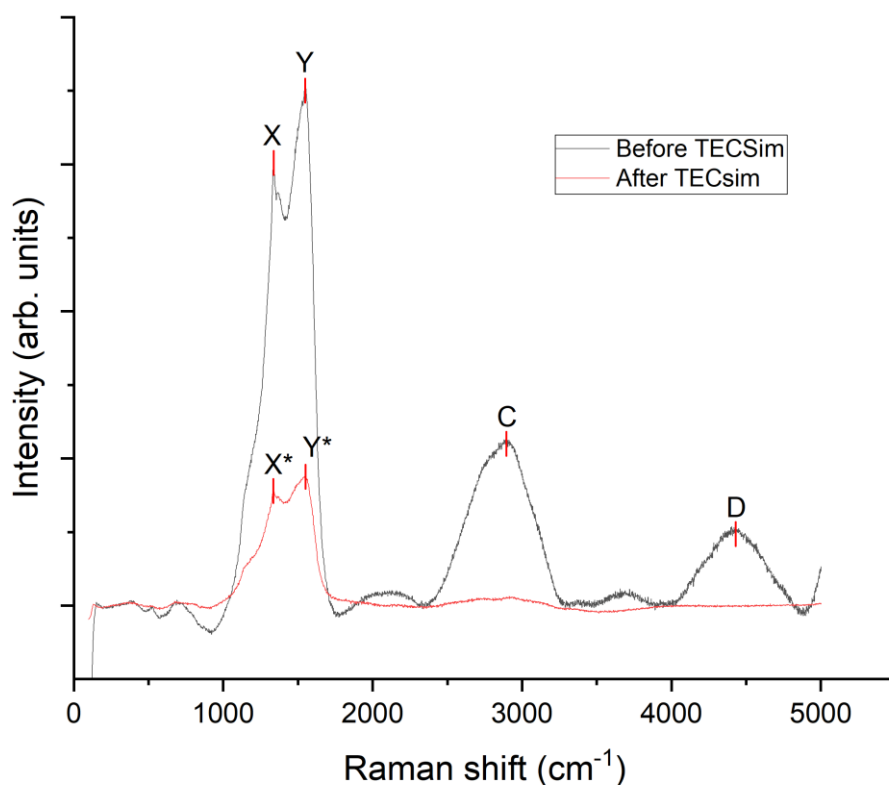


Figure 4.7: Extended Raman spectra for a PDD sample (N21139) before and after TECsim analysis.

X* and **Y*** are defined as the **X** and **Y** peaks for the sample after thermionic emission. It can be observed that the separation between **X*** and **Y*** is smaller than that between **X** and **Y**. The peaks observed at **C** and **D** are significantly lower in magnitude, with the peak at **D** disappearing completely.

4.2. SEM imaging

For each of the samples, SEM images were taken at x500 and x5000 magnifications. The main objectives of these visual representations of the sample surfaces were to corroborate any observations in the Raman spectra and to quantitatively determine the average grain size of the surface grains. Table 4.1 shows the measured, calculated and estimated average grain sizes for each of the analysed samples. The boron-doped and undoped samples were analysed using accurate measuring techniques in ImageJ, whereas the PDD and NDD samples needed to be estimated using a more rudimentary “intercept” technique, due a much smaller grain size. The intercept technique estimates the average grain size by counting the number of grain boundaries along a line of known distance. Using ImageJ, the method relies on creating a black and white “contrast” style image of the sample that highlights the grain boundaries (see Figures 9.22 and 9.23 for the undoped and BDD samples). The software then calculates the mean diameter plus errors (± 1 standard deviation). The mean areas were also calculated but are not of specific interest for this study. (See Section 9.3.3.)

Table 4.1: Estimated mean grain size for each sample.

Sample	Average diameter (μm)	Error (μm)	Diamond character
Undoped	0.2225	0.0167	Microdiamond
BDD (B1)	0.0941	0.0044	Nanodiamond
NDD (N5)	<0.0010	not given	Ultrananocrystalline diamond
PDD (N21134)	<0.0010	not given	Ultrananocrystalline diamond
PDD (N21136)	<0.0010	not given	Ultrananocrystalline diamond
PDD (N21139)	<0.0010	not given	Ultrananocrystalline diamond

Figure 4.8 shows the images of the sample N4, which was not analysed using Raman or subsequent thermionic emission analysis due to the presence of many “boulder-like” structures on the surface due to insufficient cleaning after the manual abrasion of the substrate. The presence of these boulders (arrowed in Figure 4.8) made the sample unusable for thermionic emission simulations. The SEM images for each type of dopant (boron, nitrogen, and phosphorus) as well as undoped diamond are shown in Figures 4.8 – 4.12. The most notable result from the SEM analyses is that the grains in the NDD and PDD samples are significantly smaller in size than those in the BDD and undoped samples. The SEM analyses also provide visual evidence in relation to the sharpness and intensity of the A, X and Y peaks as identified in the Raman spectra. Specifically, Figures 4.9 and 4.11 show the small grain sizes that are indicated in the Raman spectra for the NDD and PDD samples. Figure 4.9 (PDD sample N21139) shows the striations of the molybdenum substrate in the diamond indicating that the layer is a maximum of 1 μm thick. Figure 4.9 also shows a boulder-like feature as seen for N4 (Figure 4.8); however, a singular feature as can be seen for N5 will not significantly affect the thermionic emission characteristics upon testing. A feature can also be seen for the PDD sample (Figure 4.9) but this again would not be expected to affect the thermionic emission properties.

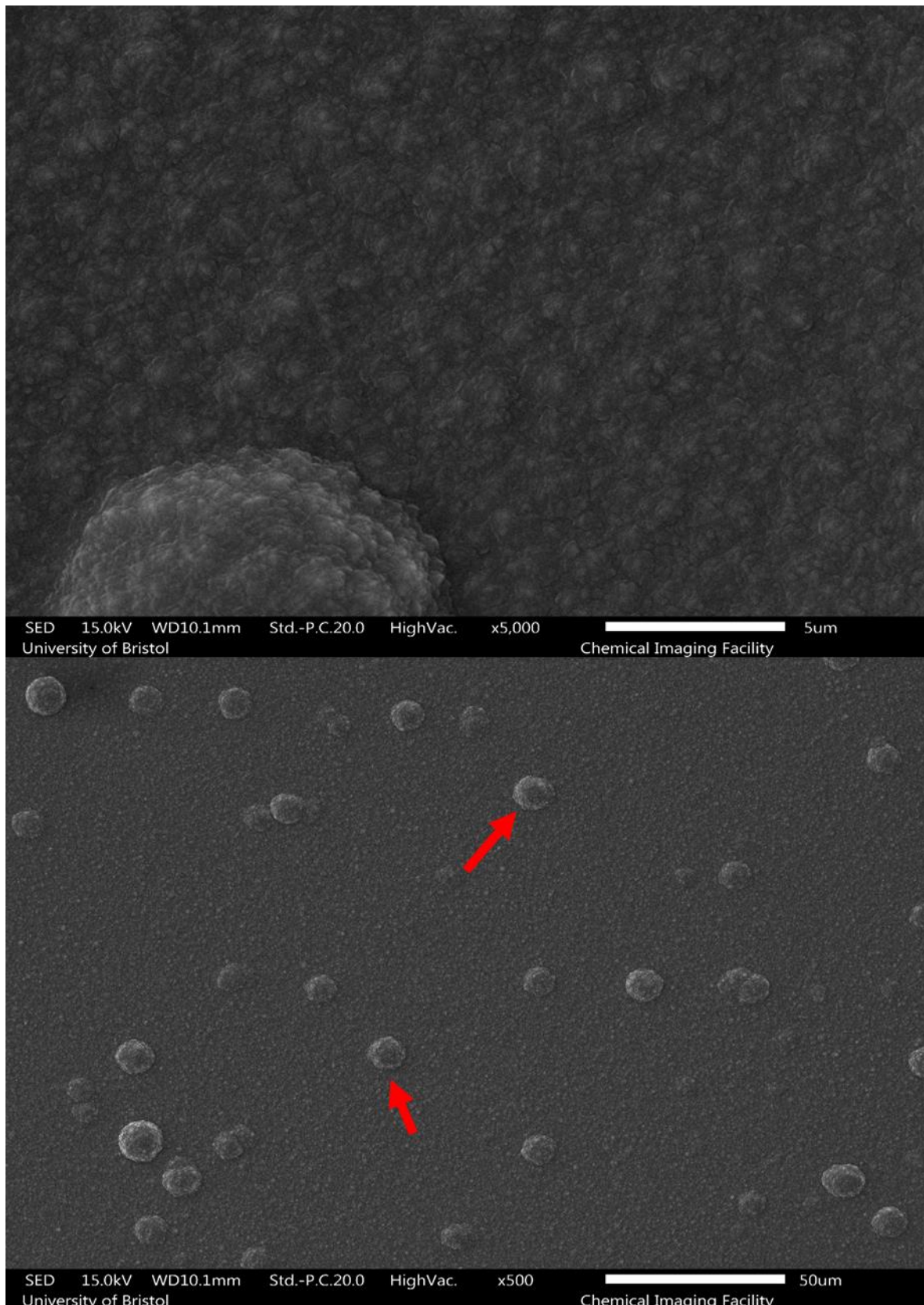


Figure 4.8: SEM images of a manually abraded N-doped sample (N4) at **(top)** x5000 magnification and **(bottom)** x500 magnification. The indicated boulder-like structures on the surface (approx. 5 μm in diameter) are due to insufficient cleaning post-abrasion and make the sample unusable for thermionic emission testing.

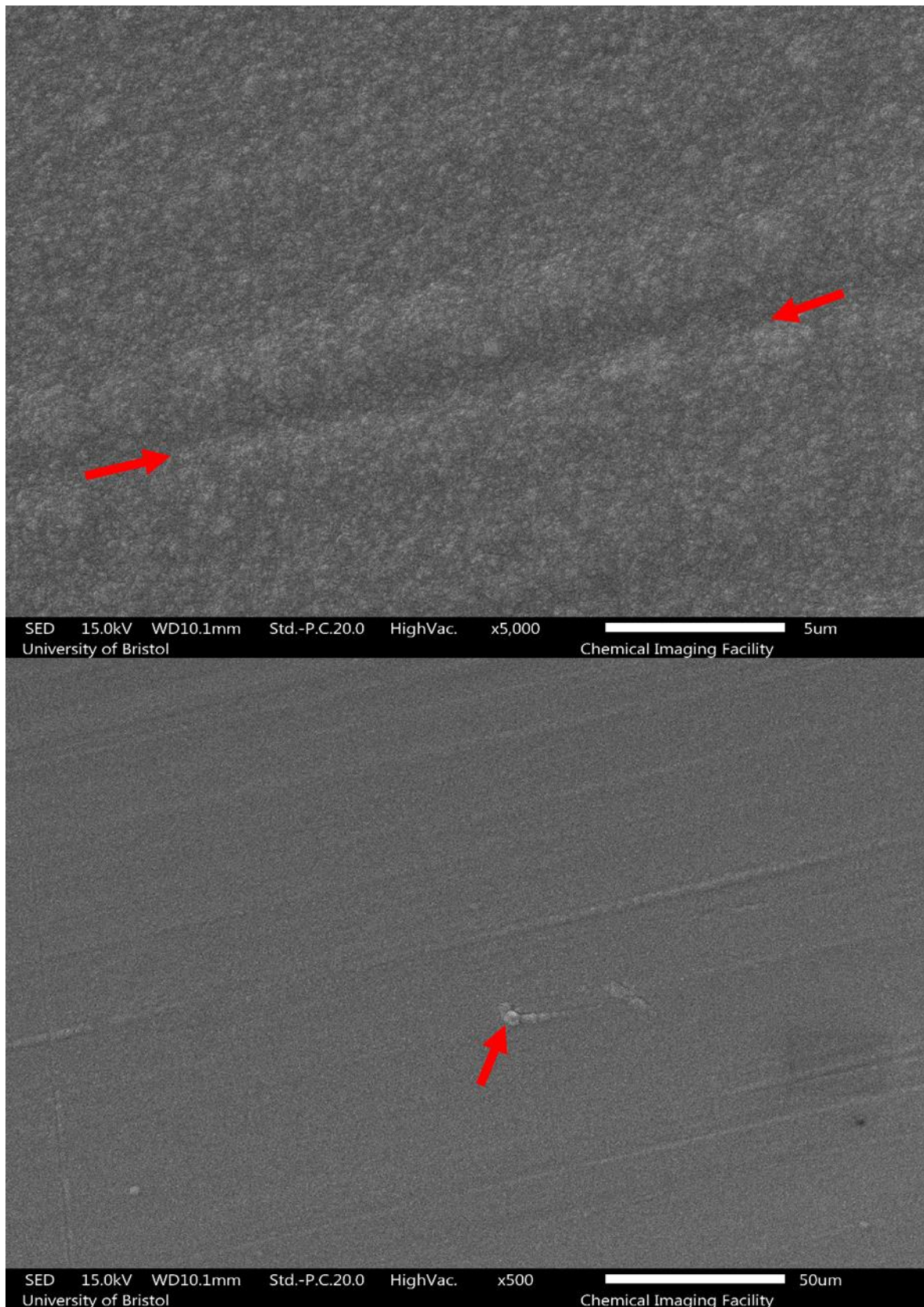


Figure 4.9: SEM images of a manually abraded P-doped sample (N21134) at **(top)** x5000 magnification and **(bottom)** x500 magnification. Striations **(bottom, arrowed)** can be seen through the diamond layer suggesting that the film thickness is c. 1 μm maximum.

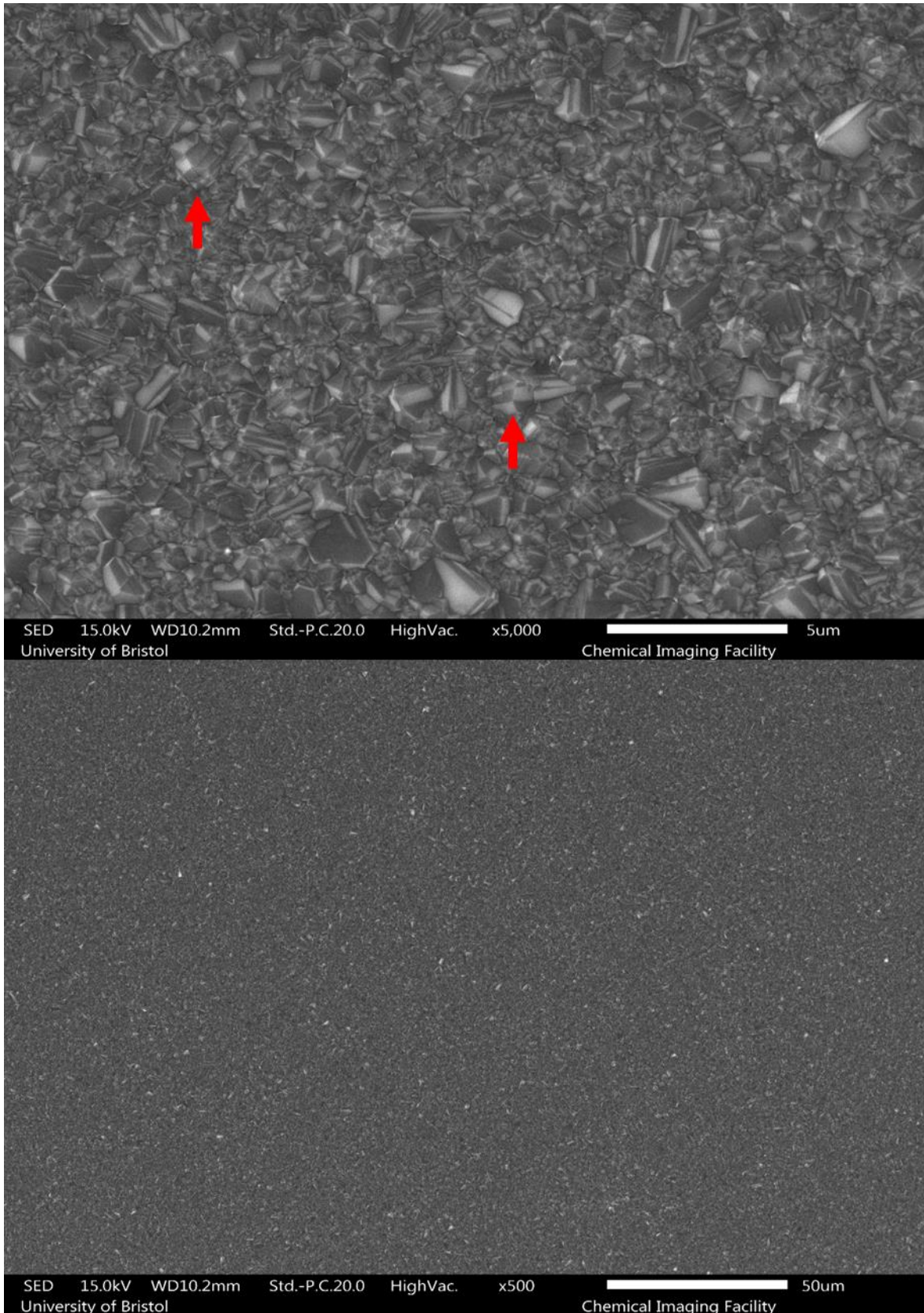


Figure 4.10: SEM images of a manually abraded B-doped sample (B1) at **(top)** x5000 magnification and **(bottom)** x500 magnification. Some diamond grains **(arrowed)** showed jagged faces (seen through lighter and darker areas), with differing orientations and growth directions.

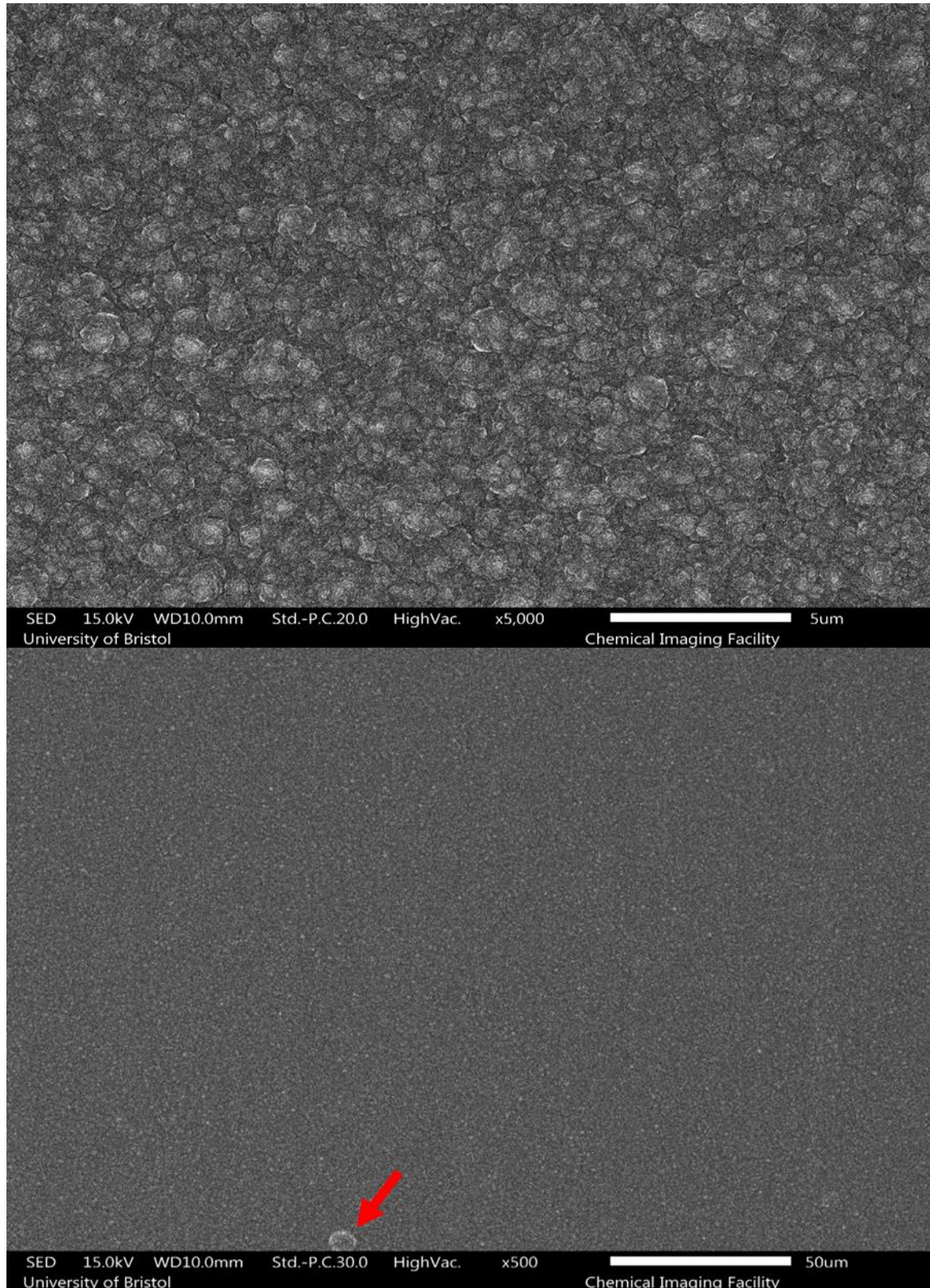


Figure 4.11: SEM images of a manually abraded N-doped sample (N5) at **(top)** x5000 magnification and **(bottom)** x500 magnification. From **(top)** the ultra-nanocrystalline (UNC) nature of the sample, established through the ImageJ measurements (see also Table 4.1), can be observed. The singular boulder **(bottom, arrowed)** is due to improper cleaning post-abrasion. A singular boulder as shown will not affect the thermionic emission seen significantly.

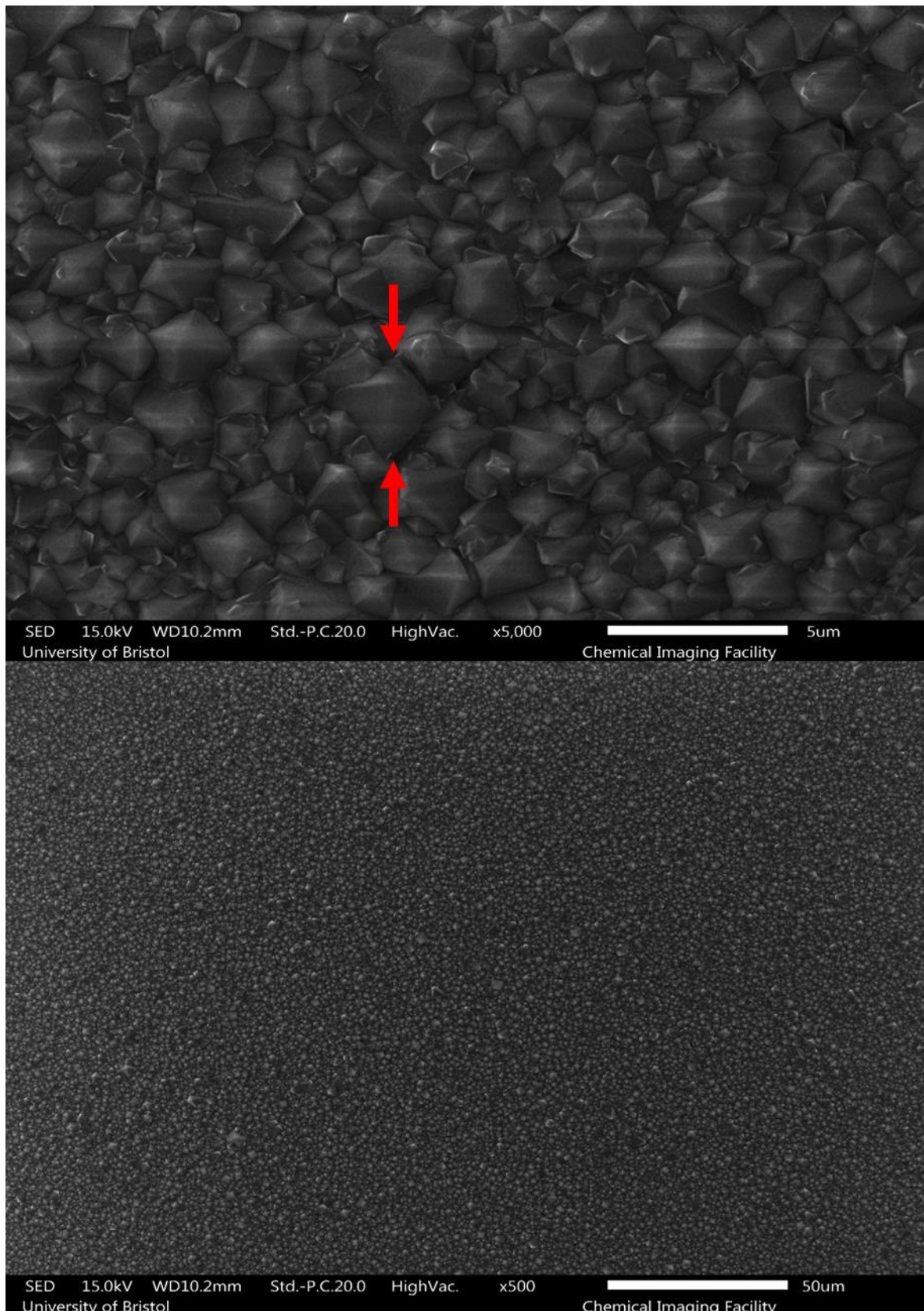


Figure 4.12: SEM images of a manually abraded undoped sample (standard) at **(top)** x5000 magnification and **(bottom)** x500 magnification. In the **(top)** image, the micro-sized grains of the sample, as determined through measurements (see Table 4.1) can be observed. One such grain (arrowed) can be seen to have a diameter of approximately 2 μm .

4.3. TECsim

Prior to the thermionic emission analysis, each sample was hydrogen terminated using the MWCVD reactor. The growth conditions for a 3-step hydrogen termination are shown in Table 4.2.

Table 4.2: Hydrogen termination conditions for individual samples.

Step	Chamber conditions	Temperature (°C)	Time (minutes)
1	Power = 1.30 kW Pressure = 120 torr H ₂ flow = 300 sccm	~880	2
2	Power = 0.70 kW Pressure = 70 torr H ₂ flow = 300 sccm	~550	2
3	Power = N/A Pressure = 34 torr H ₂ flow = 300 sccm	No heating	2

Once a sample was H-terminated, it was loaded into the TECsim (further information in Section 9.2.4). Figure 4.13 shows an example current-temperature cycle for the PDD samples tested. The BDD sample did not show an emission current below a temperature of 750 °C, which may be expected for a p-type semiconductor. No data could be collected for the NDD sample as the diamond layer delaminated during the hydrogen termination process. However, it may be speculated that the threshold temperature would be similar to that of the PDD samples, albeit with a slightly lower emission current. The three PDD samples showed different emission currents at various threshold temperatures, details of which can be found in Table 4.3. The key observation that can be made is that, for the data collected, that the sample with the intermediate doping concentration (N21136, c. 63k dopants per cm²) showed the highest emission current, and lowest threshold temperature, out of the three PDD samples. It is noted however that both the lowest and highest concentration samples did not exhibit peak emission due to lost data and short circuiting, respectively. It would be expected that the lowest doped sample (N21134, c. 16k dopants per cm²) would display a lower threshold temperature, and higher thermionic current than measured, whereas the highest doped sample (N21139, c. 250k dopants per cm²) would only display a higher thermionic current than measured. The effective work functions were calculated using the Richardson-Dushman equation (Equation 3) and the Richardson constant of diamond ($9 \times 10^5 \text{ Am}^{-2}\text{K}^{-2}$) from the measured emission currents.²¹⁴ It is noted that the calculated work function are effective work functions as the effects of space charge cannot be neglected. The errors for the effective work functions were calculated through partial derivative error propagation of the errors in the currents and temperatures. The spectra for the repeated cycles, showing a reduction in the peak current, and an increase in the threshold temperatures can be found in Section 9.3.4.

Table 4.3: Peak emission current, threshold temperatures and effective work functions for the PDD samples.

Sample	Peak emission current (mA)	Threshold Temperature (°C)	Effective Work Function (eV)	Error (eV)
N21134	0.0113*	550	1.604	0.001
N21136	0.1080	515	1.405	0.001
N21139	0.0044**	605	1.687*	0.001

*peak current from the third cycle, the data for the first and second cycles were lost.

**short-circuiting occurred before the maximum temperature was reached, so peak current is likely at least an order of magnitude higher.

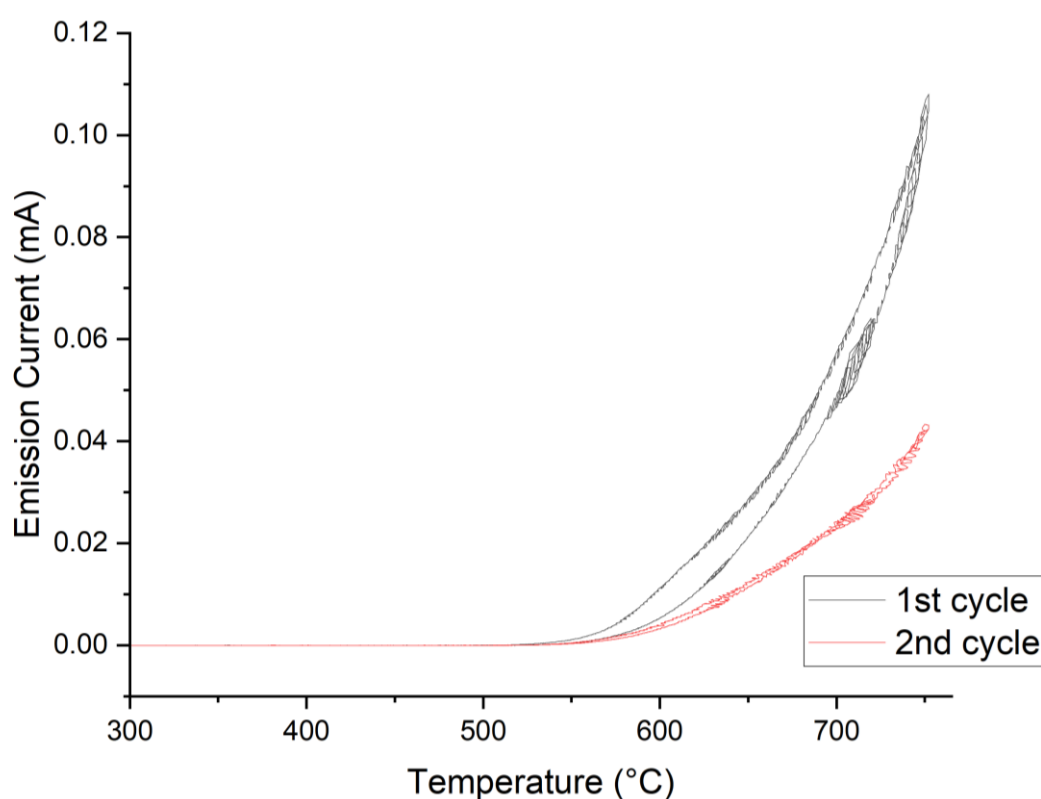


Figure 4.13: Thermionic emission cycles between 300 – 750 °C for a PDD sample (N21136). Peak emission current of 0.108 mA occurred at 750 °C, threshold temperature measured at 520 °C for the 1st cycle. In the 2nd, peak emission current of 0.045 mA occurred again at 750 °C, the threshold temperature in this 2nd cycle was slightly higher at 530 °C.

Figure 4.13, although it represents the specific measurements for sample N21136 may be taken to reflect the general trends for all samples investigated and tested. Once samples had been freshly H-terminated, the first cycle tended to result in the relatively highest emissions. Subsequent cycles then showed a decreasing emission current with an increasing threshold temperature. Hysteresis was observed for each of the emission spectra due to the sample extremities being more uniformly heated during the cooling phase of the cycle.²¹⁵

5. Discussion

The results suggest that there is indeed a relationship between the type and concentration of doping used and the thermionic emission characteristics of diamond films.

The characterisation of the sample surfaces through SEM and Raman spectroscopy was a key part of the project because previous studies have indicated that surface features and (the number of) grain boundaries on diamond films can result in reduced barriers to electron emission.^{27, 30} SEM images allow for the determination of the average grain diameter of the diamond, and can thus give an estimate of the number of grain boundaries, and a first indication of how this could contribute to the thermionic emission behaviour of the diamond films. Although there are additional factors at play (see detailed evaluation of individual samples below), it was suggested that with decreasing grain size, i.e. with increasing number of grain boundaries, the thermionic emission improves. The calculated grain sizes for each sample are shown in Table 4.1. The undoped sample, used as a control for the Raman spectra, as well as the diamond growth under standard conditions, was established to have a mean grain size of $0.2225 \pm 0.0167 \mu\text{m}$. However, the grain size distribution was wide in this microdiamond sample as grains up to $2 \mu\text{m}$ across (Figure 4.12(top), arrowed) were also observed. The grain size measured for the BDD sample was about half that of the undoped sample and the distribution was narrower, giving it a nanodiamond character. The ultrananocrystalline PDD samples, with the smallest mean grain size ($<0.0010 \mu\text{m}$) and, by implication, the highest number of grain boundaries, show the best emission behaviour out of the samples tested. This was however expected as the other sample tested had a different type of dopant. It is also noted that the dopant concentration is not linearly related to the thermionic emission (see discussion below), but the number of grain boundaries does appear to have some control.

The static Raman spectra for each of the doped samples was used to determine their surface structure and were first compared to the spectra obtained for the undoped sample in order to establish any shifts in the characteristic peaks. The Raman spectra and SEM images for the undoped sample can be seen in Figures 4.1 and 4.12, respectively. The undoped sample was used to determine the exact positions of the expected diamond (**X**) and graphite (or 'G' band) (**Y**) peaks for calibration. They were found to be at 1332 cm^{-1} and 1550 cm^{-1} which is consistent with literature values (Table 5.1).^{208, 209, 216, 217} It can be noted in Figure 4.1(bottom) that there are two additional peaks at c. 3900 cm^{-1} and c. 4700 cm^{-1} . These peaks, whilst relatively pronounced, are unexpected and have previously not been described for undoped diamond. A possible explanation is that they are due to the molybdenum substrate underneath, because the diamond film is of this sample, as well as some other samples (see Figure 4.9) may be very thin. An indication for this comes from the generally low peaks, i.e., the low signal-to-noise ratio in the Raman spectrum.

Table 5.1: Common peaks seen in the static Raman spectra of CVD diamond.

Peak Position (cm ⁻¹)	Likely source	References
1100 - 1150	Graphitic species between diamond grains	Ferrari and Robertson (2001) [216]
1332	Diamond peak	Roy et al. (2002) [208]
1350	'D' band - sp ² carbons due to dopants	Knight and White (1989) [217]
1550 - 1600	'G' band due to bulk graphite structures	Knight and White (1989) [217]

For the BDD sample, only a few characteristic peaks were observed in the static spectrum (Figure 4.2(top)), which may be due to a low dopant density from the residual doping deposition. The only peaks that were observed in its static spectrum were the diamond peak at 1332 cm⁻¹ (peak **X**), and the 'G' band at 1520 cm⁻¹ (peak **Y**). Interestingly, the 'G' band for the BDD sample is not as pronounced as for the undoped sample, despite the larger grain sizes of the undoped sample. It is unclear why this may be the case, particularly because the diamond peaks in both samples are similar in intensity. Speculating it may be said that the 'G' band has a maximum intensity.²¹⁶ Taking a Raman spectra with a higher laser power would therefore make the diamond peak appear proportionally larger. The missing peak around 1130 cm⁻¹ (labelled **A** in the NDD and PDD spectra: Figures 4.3 and 4.4, respectively) suggests that its presence or absence is predominantly controlled by the diamond grain size, or more specifically the number of grain boundaries. Whereas in the coarser-grained undoped (microdiamond) sample, and also in this still relatively coarse BDD sample it does not, or may not always, show the **A** peak that is observed for all ultrananodiamond NDD and PDD samples.²¹⁶ This coarser grain size for the BDD can be corroborated by observations from the SEM imaging and also the subsequent grain size analysis (Figures 4.10 and 9.23, respectively). The BDD sample was determined to have an average grain size of 0.00941 ± 0.0044 μm, meaning that the sample surface contained nanodiamond grains. The decreased grain size in comparison to the undoped sample is likely due to the slightly lower CH₄ content in the gaseous reactants during deposition (Growth conditions in Table 3.2), as well as the dopants incorporated into the diamond lattice. As it involves p-type doping, the introduction of the boron atoms results in deformations and "hanging" electrons. This can result in graphitic boundaries and changing growth directions, in turn resulting in the growth of new grains, and thus smaller mean grain sizes. In the SEM images this can be seen in the jagged surface faces of the diamond grains, which appear as different colours (Figure 4.10(bottom), arrowed). This effect of decreasing the grain size is less prominent than would occur for n-type dopants. Doping with a larger, n-type atom will result in adjacent carbon atoms being forced apart and adopting sp² character. These atoms sometimes appear as the peak **A**. As the boron-doped sample could still allow for some adjacent atoms to form normal sp³ bonds, the **A** peak will sometimes not be observed, or not be observed as strongly. The Raman spectra for the BDD sample show relatively little noise in comparison to spectra for the other samples. The spectra also show fewer characteristic peaks, although this can probably be attributed to the sample's thickness. The BDD and NDD samples appear to be significantly thicker than the undoped and PDD samples, meaning that the characteristic peaks will generally be more pronounced and have a higher intensity than for the very thin films.

The static spectra for the NDD sample again show the characteristic peaks for diamond and graphite at 1332 cm^{-1} and 1550 cm^{-1} , as expected (Figure 4.3(top)). The cause of the large, sharp peak at 1130 cm^{-1} (peak **A**) is, as previously mentioned, debated, but seems to occur primarily for surfaces with nanocrystalline (NC) or ultra-nanocrystalline (UNC) grains.^{209, 216, 218, 219} The NDD spectra also show a small peak at 1440 cm^{-1} (peak **B**) which is interpreted as the 'D' band, which is caused by sp^2 carbon structures from the dislocations that the nitrogen atoms create.^{209, 218} It is noted that this **B** peak is shifted significantly towards higher wavelengths when compared to both the literatures values,²¹⁷ as well as the PDD samples (Figure 4.4). The exact cause for this remains unclear but it could be a consequence of the growth conditions, as the exact growth conditions for the PDD samples are unknown. Large shifts in the peak position are also observed for the 'G' band for diamond samples grown at differing CH_4 concentrations.²²⁰ A similar shift could also be observed for the 'D' band.

Another interesting feature is that the **A** peak for the NDD sample is significantly more prominent than is usually expected for NC samples. This high intensity of the nanodiamond peak may be attributed to the high number of grain boundaries i.e. a very small mean grain size in the NDD sample (see Table 4.1). Even at large magnifications (x5000), as shown in Figure 4.11(top), individual diamond grains could barely be discerned. The introduction of larger p-type atoms introduces dislocations and vacancies resulting in a discontinuous grain growth. As the nitrogen-dopant atoms are larger than carbon atoms, the carbons adjacent to the nitrogen atom are pushed apart. This results in some of these carbon atoms displaying sp^2 bonding.^{209, 218} This results in the **B** peak observed on the static spectrum, and it also introduces more disorder in the growth directions, resulting in the less consistent growth of the diamond grains. The lack of this peak on the BDD spectrum can be explained accordingly. As the B-dopant atom is smaller than the N-dopant atom, the adjacent carbons are affected less by their introduction. This is also why there is no observed shift in the positions of the **X** and **Y** peaks for the BDD sample when compared to the undoped sample, despite there being dopants incorporated into the diamond lattice. Another noticeable feature on the NDD sample SEM image is the presence of a boulder-like structure (arrowed) similar to those seen for sample N4 (Figure 4.8). While a large number of features as those seen for N4 will affect the thermionic emission behaviour, a singular boulder as seen for N5 (Figure 4.11) will not.

Similar features were observed in the static spectra for the PDD samples (Figures 4.4(top), 9.13(top), and 9.14(top)). The Raman spectra for all three PDD samples showed the characteristic peaks for diamond at approximately 1338 cm^{-1} (peak **X**), the 'G' band at 1540 cm^{-1} (peak **Y**), and the 'D' band at 1370 cm^{-1} (peak **B**).^{208, 209, 217, 218} All samples also showed a nanodiamond peak around 1130 cm^{-1} (peak **A**), which may be linked to the UNC nature of the PDD samples (see Table 4.1). The observed shift of $+6\text{ cm}^{-1}$ in the diamond peak (1338 versus 1332 cm^{-1}) is explained by the introduction of the phosphorus dopants. As they are significantly larger than carbon atoms, it results in a large dislocation that affects adjacent carbons. It also results in a 'D' band of a higher intensity due to an increased number of sp^2 carbons near the dopants. This shift in the diamond peak, not seen for the NDD sample, is explained by the P-dopant being significantly larger than a N-dopant. Hence, a larger shift is observed for the PDD sample. The -10 cm^{-1} shift for the 'G' band and the position of the 'D' band do not indicate any specific structural abnormalities other than the introduction of dopants into the lattice. The SEM images for all three PDD samples (Figures 4.9, 9.24, and 9.25) show small mean grain diameters, similar to the NDD sample (Figure 4.11). Despite the PDD samples having long growth times between 6 and 8 hours, the resulting diamond layers are found to be very thin ($<1\text{ }\mu\text{m}$). This is confirmed in the visibility of striations through the diamond layer (Figure 4.9, arrowed), which are attributed to scratches that occur from the polishing of the molybdenum substrate (Zulkharnay, pers. comm.). Clearly, having such a thin layer of diamond will have consequences for the thermionic

emission properties of the sample, which will be considered when the thermionic emission experiments are discussed below. The small grain sizes measured for the PDD samples are also associated with the introduction of the large phosphorus atoms. Additionally, the diamond tends to grow conically from the substrate surface meaning that, for thicker layers, the surface grains are larger than they are at the diamond/substrate interface.²²¹ This means that for the thin PDD samples, the grains are expected to be smaller than for the thicker BDD and NDD layers, which provides another possible explanation for why the BDD sample shows larger grain sizes than the NDD and PDD samples.

The extended spectra usually look for additional information on overtone and combination bands for the species determined in the static spectra. The presence of strong peaks in the extended spectra can indicate a high concentration of a specific species on the surface. The 'D' band (peak **B**) often shows strong overtone/combination bands around 2450 cm^{-1} , 2725 cm^{-1} , and 2950 cm^{-1} respectively.²⁰⁹ The peaks labelled **C** and **D** on the NDD sample and PDD samples ((Figure 4.3(bottom) and Figures 4.4(bottom), 9.13, and 9.14) are not interpreted to be overtone or combination bands of the 'D' band as the peaks are significantly wider than would be expected for such peaks. Another explanation for the peaks could be associated with the hydrogen termination of the samples. In optical spectroscopy, high shifts are usually due to hydrogen bonds or intramolecular hydrogen bonds. (Orr-Ewing, pers. comm.) Praver and Nemanich observed similar peaks and found that there are multiple peaks in the range of $2700 - 3100\text{ cm}^{-1}$ for hydrogenated samples.²⁰⁹ This trend was seen for the NDD and PDD samples (Figures 4.3(bottom), 4.4(bottom), 9.13(bottom), and 9.14(bottom)), but not for the BDD sample, (Figure 4.2(bottom)) despite also being hydrogenated (see below). There are several potential ways that these peaks could be due to the hydrogen termination species, and the detailed analysis of the Raman spectra allows for the exclusion of a few of these:

First, it was needed to confirm that the observed peaks were indeed due to hydrogen interactions. It is well known that hydrogenated samples are unstable above $650\text{ }^{\circ}\text{C}$.^{31, 210-213} Therefore, as a single thermionic emission cycle heated the samples up to $750\text{ }^{\circ}\text{C}$, and multiple cycles were run per sample, significant hydrogen desorption may be assumed to have occurred during thermionic emission analysis. The Raman spectra for each PDD sample were therefore repeated to see how the peak intensity differed with a lower coverage of hydrogen on the surface. Figure 4.7 shows a comparison for the Raman spectra of a PDD sample (N21139) taken before and after thermionic emission analysis. The diamond peak and 'G' band for the sample after thermionic analysis appear to be closer together in the static region ($1100 - 1600\text{ cm}^{-1}$) of the spectrum, but why this occurs is unclear. The main goal of comparing the sample before and after is to contrast the intensities of the **C** and **D** peaks. Figure 4.7 shows that the intensities for these two peaks dropped significantly post-thermionic emission analysis, with the peak at **D** disappearing entirely for sample N21139. This confirmed that the peaks occurred due to hydrogen interactions with the sample, and therefore also corroborating its interaction with the dopant species. To evaluate the nature of these interactions, Raman spectra for each PDD sample were compared, as each sample was grown with a slightly different dopant concentration (based upon the concentration of the gases in the reaction chamber). While exact reasons remain unclear, current speculations are that the peaks are either due to doping clusters in the diamond structure, where the n-type dopants bond with the hydrogen before being deposited into the diamond lattice, or due to dopant species being visible on the surface and becoming hydrogenated. Pre-TECsim analysis (Figure 4.5) suggests that the highest intensities for the **C** peak occur in the two samples with the lowest doping concentrations, whereas the highest signal intensity for the **D** peak was observed for the 'intermediate' sample (N21136, c. $63\text{k dopants per cm}^2$). Across both peaks, the highest signal intensity was seen for sample N21136. This is unexpected as, theoretically, higher doping concentrations would be more likely to have dopants at the surface,

which would thus be available for interaction with the hydrogen surface termination. It is possible that exposure to oxygen in ambient conditions resulted in a reduction of the surface coverage of hydrogen, however. The final feature of note is that for the sample with the highest concentration of doping (N21139, c. 250k dopants per cm^2), the position of the **D** peak occurs at an approximately 200 cm^{-1} higher shift than for the other PDD samples. A logical explanation would be that the increased dopant concentration has resulted in a shifted peak position, due to more disorder in the diamond lattice. Post-TECsim analysis, a clear, negative trend was shown in the intensity of peak **C** with an increasing dopant concentration (Figure 4.6). A large reduction was also seen for peak **D** which was not observed for any of the PDD samples. In this situation however, the position of peak **C** was shifted for sample N21139. While this was not seen in Figure 4.5, the reasons are probably similar. The trend observed for peak **C** is interesting and opposite to what would be expected. The highest peak intensity was observed for the sample with the lowest doping concentration. As the proposed causes were associated with hydrogen-dopant clusters or surface interactions between hydrogen and the dopant, a higher dopant concentration would naturally be expected to have a higher signal intensity. This conflicting result would therefore require further characterisation to fully investigate the potential causes for these peaks (see Section 6).

After the Raman and SEM analyses, the thermionic behaviour of the PDD and BDD samples was further analysed using the home-built thermionic emission kit (see Section 9.2.3.). All profiles obtained for the PDD samples (Figure 4.13, 9.24, and 9.25) showed emission below $750 \text{ }^\circ\text{C}$ with threshold temperatures in the range of $500 - 600 \text{ }^\circ\text{C}$ on the primary run. This was an expected result for n-type diamond that has been terminated with hydrogen, as an NEA surface will be formed.^{17, 44, 121, 124} The fact that the BDD sample did not exhibit thermionic emission is also as expected. While the H-termination and B-doping should be expected to result in band-bending at the surface, particularly given the doping concentration used in this study, a higher temperature would be required for emission to occur. It may be expected that the BDD sample would, not considering hydrogen desorption, would start to exhibit emission at a higher temperature. Another noticeable trend was that the PDD profiles exhibit hysteresis throughout the analysis. This effect is commonly observed in this type of analysis and is caused by the increased uniformity of the surface temperature across the surface upon cooling.²¹⁵ Increased surface temperature uniformity usually results in increased emission currents and decreased threshold temperatures for any type of doped diamond. The increased surface temperature uniformity observed under cooling is a side effect of the method of sample heating method in the TECsim (explained in detail in Section 9.2.3). A laser heats the back of the sample, meaning that during heating, the edges of the sample are slightly cooler than the centre. Upon cooling, this effect is less pronounced as the centre of the sample is cooled through a reduction of the laser power, which generally means that the corners and edges cool at a similar rate to the centre of the sample.

There is a marked reduction in the emission currents, as well as an increase of the threshold temperatures between cycles which can be attributed to the desorption of hydrogen at temperatures exceeding $650 \text{ }^\circ\text{C}$. These changes, illustrated in Figure 4.13 for the sample N21136 but observed for the other PDD samples as well, resulted in a reduction of approximately 70% relative to the maximum emission current measured for the first cycle. Table 4.3 shows the maximum measured emission currents for each of the PDD samples. The highest emission current was observed for the sample with intermediate doping concentration (N21136, c. 63k dopants per cm^2). It should be noted that for the lowest doped sample (N21134, c. 16k dopants per cm^2), data were only stored for the third emission cycle. Based upon trends from the other samples however, it may be expected that a higher emission current (as well as a lower threshold temperature) would have occurred in the first run (estimated to

be approximately an order of magnitude higher). For the sample with the highest doping concentration, the circuit short-circuited before the maximum temperature of the profile was reached. However, the threshold temperature obtained would not have been significantly affected if a full profile had been taken, but the emission current would have been higher in magnitude.

From literature, the H-terminated PDD systems have computationally been shown to have large, positive work functions in the range of 4 to 5 eV.⁸³ However, experimental work has found work functions as low as 1.18 eV.¹⁸ Table 4.3 shows the calculated work functions for the PDD samples in this study based on the measured thermionic emission current and the Richardson constant of diamond ($9 \times 10^5 \text{ A}\cdot\text{m}^{-2}\cdot\text{K}^{-2}$).²¹⁴ These work functions are assumed to be “effective” as the presence of space charge effects cannot be neglected despite the application of a forward bias of c. 25 V.¹⁶ All samples showed effective work functions in the range of 1.4 - 1.7 eV. The lowest effective work function found, 1.408 eV, was for the intermediately doped sample (N21136, c. 63k dopants per cm^2) and the highest, 1.687 eV, was found for the highest doped sample (N21139, c. 250k dopants per cm^2). As stated, the effective work function for N21139 may be assumed to have been lower had no short-circuiting occurred. However, the threshold temperature is also higher for samples that have a higher effective work function. As the threshold temperature for N21139 would have been approximately 600 °C, it may be assumed that the effective work function, and hence the emission current, would still have been lower than for N21136. The same logic could not be applied to the sample with the lowest doping concentration, however. As the threshold temperature and emission current have both been shown to vary across multiple testing profiles, the exact threshold temperature or emission current for N21134 can unfortunately not be estimated. The only useful information provided is a comparison of the threshold temperature with the repeated cycles for the other samples. Assuming that there is an approximate reduction for the emission current of 70% between each cycle, a third emission cycle for the N21136 sample would have shown an emission current of c. 0.02 mA. If this is compared to the current observed for the third cycle for the sample N21134, which is 0.0012 mA, still the intermediate sample has a noticeably higher current. In the case of nitrogen-doped diamond, increasing the doping concentration leads to a more negative electron affinity as the donor level of nitrogen becomes more accessible. It can therefore be assumed that the lower doped sample (N21134) has a lower emission current and higher threshold temperature than the intermediate doped sample (N21136). The higher threshold temperature observed for the highly doped sample (N21139) is therefore interesting. Logically, the increased dopant concentration should result in a higher emission current and lower threshold temperature. It has however been suggested that for NDD, increasing the dopant concentration, above some critical value, results in a negative effect on the electron affinity and work functions observed. (Fox, pers. comm.) This effect likely also applies to PDD as it is suggested that once that concentration has been reached, the carbon atoms behave in a manner similar to the dopant species, which obviously limits the desirable properties of the material. The work functions calculated in this study are consistent with those calculated for other PDD systems using the same characterisation equipment and PDD samples, as the samples were cut to size from a larger wafer.²¹⁵ While Wills analysed the PDD samples in the context of the collector instead of the emitter, similar currents were measured in that study as the difference in the work functions between the emitter and collector were also similar. The higher work functions observed for the PDD samples in both the present study, as well as Will’s study, are explained by a thinner-than-expected PDD layer. A thicker layer would have likely resulted in higher emission currents at every temperature, simply because a larger number of electrons would be available. It is known that there is a required trade-off between the maximum power output and device efficiency (from Equations 6 and 7). As this system used a H-terminated PDD emitter and a tungsten collector (see Section 9.2.3),

the calculated difference in the surface work functions is approximately 3 eV as the work function of tungsten is 4.9 eV.²²² In order to maximise the emission current, a smaller collector work function would be needed (from Equation 7), however, this would have a detrimental effect on the efficiency of the system (from Equation 6). As the boundary for usable emission currents is $>1 \text{ A.cm}^{-2}$,^{23, 24} a significant increase in power would be required before the samples in this study would be useable. As the efficiency was not calculated, ideally the collector work function would have to be decreased in order to make them viable.

Based upon literature values for the work function of NDD samples, it may be expected that the emission currents that should have been obtained for the NDD sample would have been lower than those obtained for the PDD samples in this study.¹³⁹ The work by Zulkharnay found an effective work function of 1.48 eV for the NDD sample. This is explained by the donor level of PDD being closer to the conduction band than for the NDD, meaning that the movement of electrons into the conduction band has a smaller energy barrier. However, some studies such as a study by Kataoka, found that NDD samples actually showed a higher emission current than PDD.²²³ As the dopant concentration plays a large role in the emission currents observed, it means that samples are not necessarily most efficient at the highest doping concentrations. In fact, it has been suggested that a high doping concentration in NDD can detrimentally affect the thermionic emission currents (Fox, pers. comm.). Therefore, based upon previous experimental and computational studies and the low dopant concentrations of the samples in this study, it can be speculated that if sample N5 had been thermionically tested, it might have exhibited a lower emission current and higher work function than the PDD samples tested. Still, NDD remains interesting as a material as its growth rate, sample purities, and growth consistencies are significantly better than for PDD. For the eventual use in TEC devices, these characteristics currently mean that NDD is still closer to practicality than PDD.

Unfortunately, many technical issues meant that this study did not proceed as planned, and the analysis concentrated on H-terminated samples only. Further work should therefore focus on decreasing the effective work function through surface functionalisation (See Section 6). Scandium-termination, which was an initial additional focus of this study, specifically holds much promise for the improved thermionic behaviour of diamond films.¹³⁸⁻¹⁴⁰

6. Future Work

Due to a series of technical and equipment failures and mishaps, several of the intended aims of this study were not met. The work that could be carried out led to some interesting results and insights, but there are still several research avenues that were unfortunately not attempted. The presented work focused on the characterisation and thermionic testing of hydrogen-terminated doped diamond surfaces, and as touched upon in the previous section, a logical next step would be to run the same test for scandium-terminated samples using the same dopants.

Certain characterisation techniques that were planned were unavailable on the present timescale. One of the characterisation techniques is Secondary Ion Mass Spectrometry (SIMS), which could provide information about the exact dopant concentrations of the samples. To use an example, a back-implanted NDD sample supplied by the University of Surrey, was used to calibrate the SIMS equipment for the detection of N dopants in a sample. Figure 6.1 shows an example graph, from work by Othman,¹²⁴ of what an expected SIMS depth spectrum looks like.

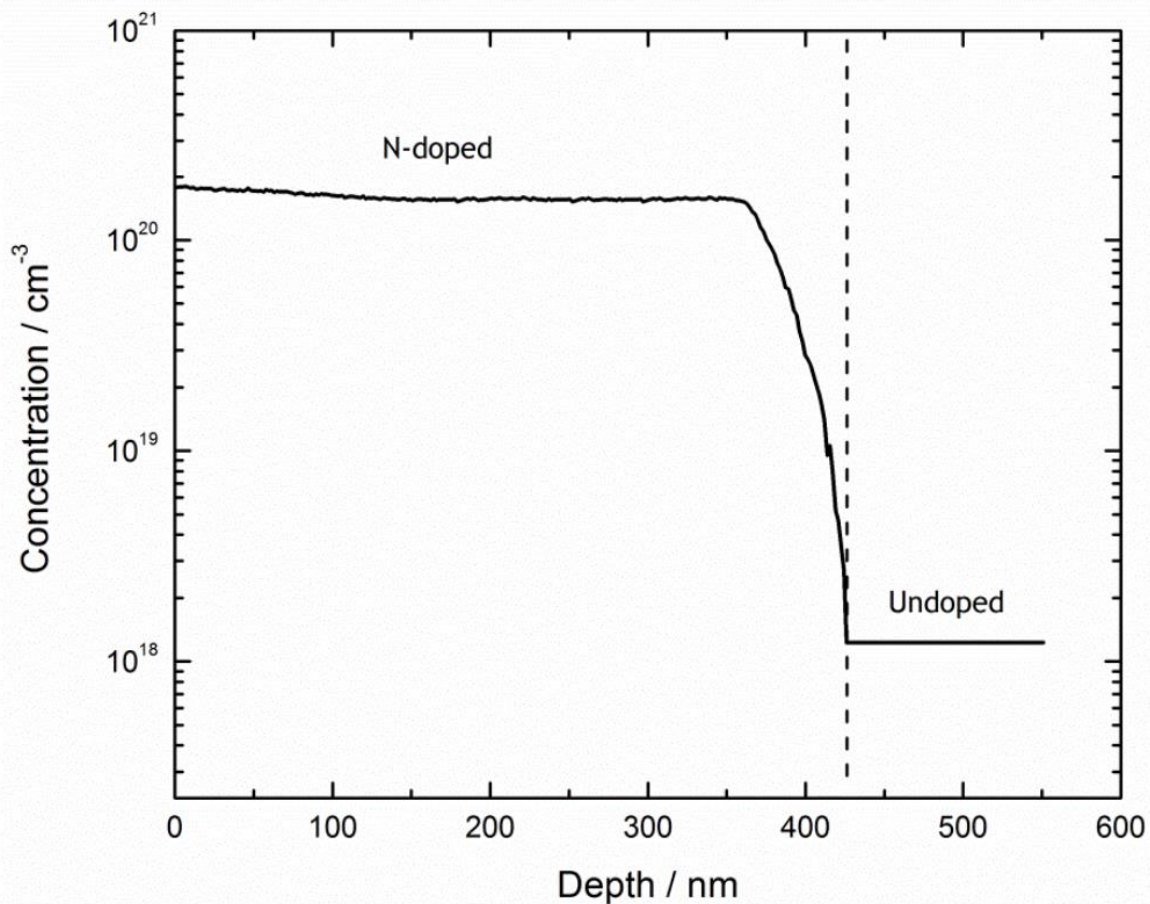


Figure 6.1: A depth profile of a NDD sample from a calibrated SIMS detector. Spectrum from reference [124].

This method thus characterises how the nitrogen concentration varies with depth into the dopant layer. It allows calculations to be made of the carrier density within the material, allowing for quantification of the effect of doping on the efficiency of heat transfer throughout the sample. Again, a logical next step would be to extend the research onto NDD samples of varying dopant

concentrations to examine how these affect the thermionic emission properties. This could also be repeated for P-doped samples, although back-implantation using phosphorus is substantially more difficult. More details on SIMS can be found in Section 9.2.4.

In future work, further characterisation of the diamond layer could be carried out through ultraviolet and X-ray photoelectron spectroscopy (UPS and XPS, respectively) to provide specific and detailed information about the electrons of the sample. The XPS and UPS equipment is fitted onto the nanoESCA and these techniques are covered briefly in Section 9.2.5. The methods allow for the determination of the binding energies of the electrons and can be used to corroborate the Raman spectral data. However, the binding energy also relates to the work function of the samples, which calls for the creation of work function maps that show the local work function across the sample surface. Figure 6.2 shows an example of a work function map, taken from Wills.²¹⁵

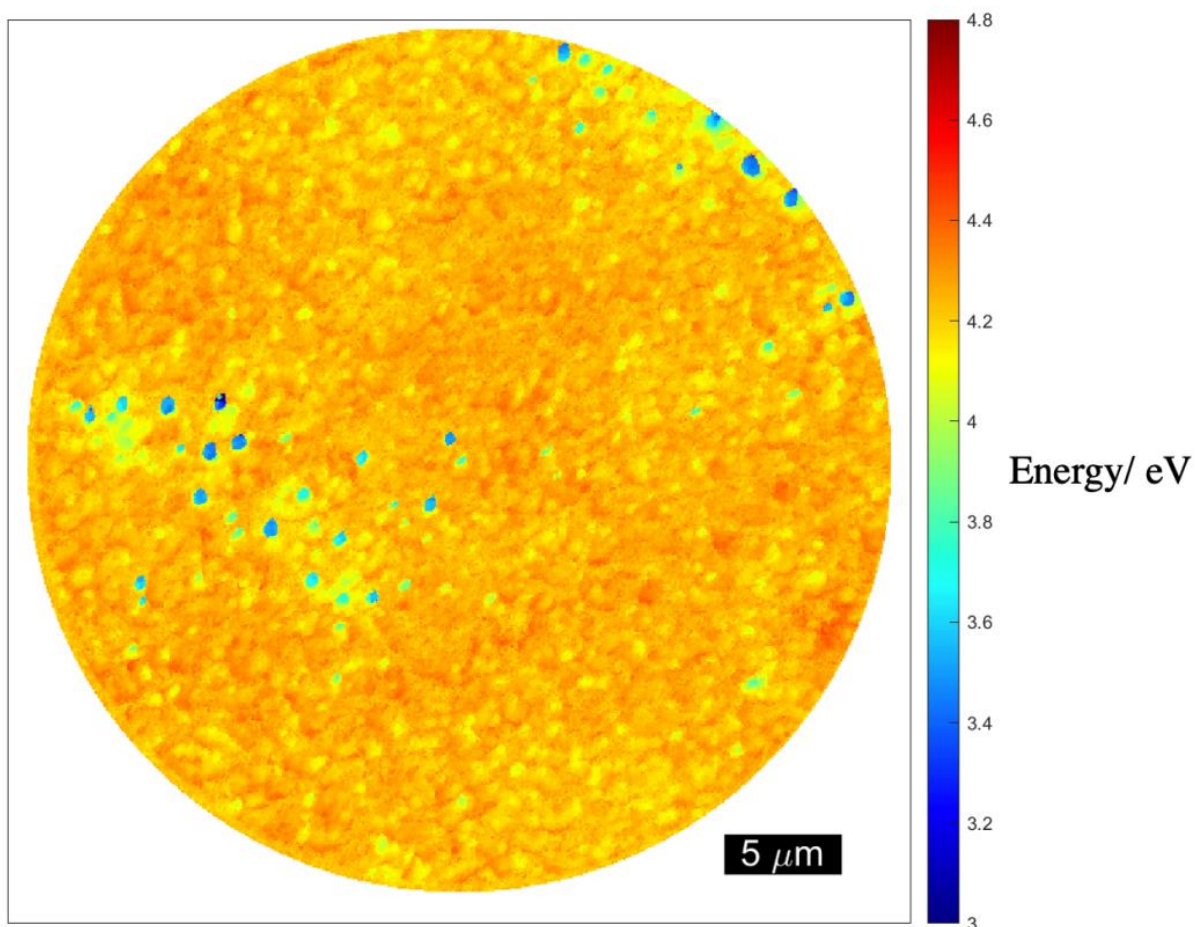


Figure 6.2: A heat map of the work function across a bare PDD surface grown under 0.75% CH₄ conditions. Map from thesis by Wills. [215]

The maps allow for the quantification of the effect space charge effects have on the thermionic emission of the sample through comparison to the effective work functions. This in turn could be combined with TECsim measurements with low/no bias to determine the true barrier to emission of the isolated surface.

This additional characterisation of the diamond surface would create the baseline for work on how altering the surface termination to other species affects the magnitude of the NEA. As stated, one area that would be of particular interest would be to terminate the doped diamond surfaces with a

species such as scandium. As scandium is a small electropositive metal, it theoretically increases the magnitude of the NEA at the surface. Previous work on scandium found that the work function and electron affinity decrease drastically compared to their H-terminated counterparts from 3.49 eV to 3.22 eV for the (100) undoped diamond and 3.62 eV to 3.52 eV for the (111) undoped diamond.¹³⁹ Using the Richardson-Dushman equation, this reduction in the work function and electron affinity results in a marked increase of the thermionic emission current of a sample. Provided there is a good contact between the scandium terminations and the diamond film, the threshold temperature would also be expected to increase further. The reduction of the threshold temperature (through reduction of the emission barrier) is one of the main hurdles for the mainstream use of TEC devices in industrial applications. The effects of space charge are reduced through the application of a forward bias in the device (or during thermionic analysis).

For the H-terminated samples that were studied, the possibility of PETE devices would still be plausible, albeit not with visible light, reducing the threshold temperature and possibly allowing thermionic emission to occur at temperatures that would allow for the industrialisation of TEC devices. This would be an interesting future direction in which to take this research. It would require an adjustment to the thermionic kit as a light source would need to be added. Based on the chamber design, it would have to be a top-down light source that would require the sample mount described in Section 9.2.3 to be adapted to have a collector transparent to the wavelength of the light selected. In such a case, the light source could be added to shine directly through the collector and onto the sample surface, thus increasing the energy supplied to electrons in the emitter's bulk.

7. Conclusions

Diamond film samples were prepared to investigate the effects of nitrogen-, boron-, and phosphorus-dopants (the latter in different concentrations) and hydrogen termination on the thermionic emission behaviour of diamond films. The samples were characterised using SEM and Raman spectroscopy before being tested for thermionic emission using thermionic emission analysis.

Analysis of the SEM images revealed that the grain size of the phosphorus-doped diamond (PDD) and nitrogen-doped diamond (NDD) samples all exhibited an ultrananocrystalline character with mean grain diameters of less than $0.001\ \mu\text{m}$. The undoped and BDD samples had coarser grains with mean grain diameters of approx. $0.2225 \pm 0.0167\ \mu\text{m}$ and $0.0941 \pm 0.0044\ \mu\text{m}$, respectively. While dopant concentration does not show a linear relationship with thermionic emission, the number of grain boundaries does exert some level of control in that a higher number of boundaries appears to reduce the emission barriers.

Static Raman spectra were used to characterise the samples and to determine the species on the diamond surface. The key peaks found were the diamond peak at c. $1332\ \text{cm}^{-1}$ and the 'G' band or graphite band around $1550\ \text{cm}^{-1}$ (all samples), and peaks that were attributed to graphitic grain boundaries in the ultrananocrystalline samples (NDD and PDD). There was also a 'D' band that is due to disordered diamond as a consequence of the doping atoms (NDD and PDD). A shift was observed for the PDD samples only, from $1332\ \text{cm}^{-1}$ to $1338\ \text{cm}^{-1}$ that was interpreted to be due to the introduction of the phosphorus dopants. As they are larger than nitrogen and thus cause more deformation in the diamond lattice, this shift was not seen for the NDD samples. The extended Raman spectral analyses found interesting but peculiar peaks around $2900\ \text{cm}^{-1}$ and $4200 - 4500\ \text{cm}^{-1}$ for both the NDD and PDD samples. These were speculated to be due to interactions between the p-type dopants and the hydrogen terminations. In additional analysis, through the comparison of the extended Raman spectra before and after thermionic analysis, it was established that the intensity of these peaks did decrease upon the desorption of hydrogen from the surface. However, when looking at how the dopant concentration affected the intensity, it was found that an increase in the dopant concentration resulted in a decrease in the peak intensity. The causes for this are unclear and would require further research.

The thermionic analysis revealed that the boron-doped diamond (BDD) sample showed no emission below $750\ ^\circ\text{C}$, which was expected from p-type diamond despite the favourable effects of band bending caused by the hydrogen termination. The PDD samples all exhibited a thermionic emission current below $750\ ^\circ\text{C}$ with threshold temperatures between $500 - 600\ ^\circ\text{C}$. It was found that the sample with the 'intermediate' doping concentration (N21136, c. 63k dopants per cm^2) exhibited the highest thermionic emission current of $0.105\ \text{mA}$. It was projected that at the observed threshold temperature of approximately $600\ ^\circ\text{C}$ exhibited by the sample with the highest doping concentration (N21139, c. 250k dopants per cm^2), it would have exhibited a lower thermionic emission current than the 'intermediate' sample. As expected, the sample with the lowest dopant concentration would also have shown a lower emission current, and a higher threshold temperature, than sample N21136. Multiple thermionic profiles were taken, and it was observed that each consecutive cycle resulted in a marked decrease in the maximum emission current, and a clear increase in the threshold temperature. The effective work functions calculated for the samples followed the same non-linear trend that was observed for the thermionic emission currents. The work functions of the PDD samples were found to be in the range of $1.4 - 1.7\ \text{eV}$ with the sample with the highest dopant concentration

exhibiting the highest work function of 1.687 eV. The lowest work function was found to be 1.408 eV, shown by sample N21136.

The measured and calculated emission currents and work functions of the tested diamond samples were all in a range that were significantly below values that would be considered promising for development of the doped materials in practical applications. Recommendations for future research focus on NDD material as this has the most uniform surface characteristics and because, out of the doped samples in this study, it is relatively the easiest to grow and manufacture samples with uniform grains and doping concentrations.

8. References

1. K. G. z. Ikhtiyorovna, *American Journal of Language, Literacy and Learning in STEM Education (2993-2769)*, 2023, **1**, 339-344.
2. R. G. Bodkhe, R. L. Shrivastava, V. K. Soni and R. B. Chadge, *International Journal of Electrochemical Science*, 2023, **18**, 100108.
3. A. Sowers, B. Ward, S. English and R. Nemanich, *Journal of applied physics*, 1999, **86**, 3973-3982.
4. J. Cui, J. Ristein, M. Stammler, K. Janischowsky, G. Kleber and L. Ley, *Diamond and Related Materials*, 2000, **9**, 1143-1147.
5. P. May, J. Stone, M. Ashfold, K. Hallam, W. Wang and N. Fox, *Diamond and related materials*, 1998, **7**, 671-676.
6. J. L. Van Noord, H. Kamhawi and H. K. McEwen, *Characterization of a high current, long life hollow cathode*, 2006.
7. V. L. Granatstein, R. K. Parker and C. M. Armstrong, *Proceedings of the IEEE*, 1999, **87**, 702-716.
8. P. J. Wilbur, R. G. Jahn and F. C. Curran, *IEEE Transactions on Plasma Science*, 1991, **19**, 1167-1179.
9. J. Van Noord, *NEXT ion thruster thermal model*, 43rd AIAA/ASME/SAE/ASEE Joint Propulsion Conference & Exhibit, 2007, 5218.
10. M. Geis, J. Twichell, N. Efremow, K. Krohn and T. Lyszczarz, *Applied Physics Letters*, 1996, **68**, 2294-2296.
11. Q. Dong and J. M. Cole, *Scientific Data*, 2022, **9**, 193.
12. M. C. James, F. Fogarty, R. Zulkarnay, N. A. Fox and P. W. May, *Carbon*, 2021, **171**, 532-550.
13. J. Shammass, *Characterization of Cubic Boron Nitride Interfaces with in situ Photoelectron Spectroscopy*, Arizona State University, 2016.
14. I.-N. Lin, S. Koizumi, J. Yater and F. Koeck, *MRS Bulletin*, 2014, **39**, 533-541.
15. F. Koeck, J. Garguilo and R. Nemanich, *Diamond and related materials*, 2004, **13**, 2052-2055.
16. F. A. Koeck and R. J. Nemanich, *Diamond and related materials*, 2006, **15**, 217-220.
17. F. A. Koeck, R. J. Nemanich, A. Lazea and K. Haenen, *Diamond and related materials*, 2009, **18**, 789-791.
18. F. A. Koeck, R. J. Nemanich, Y. Balasubramaniam, K. Haenen and J. Sharp, *Diamond and related materials*, 2011, **20**, 1229-1233.
19. R. Nemanich, P. Baumann, M. Benjamin, S. King, J. Van der Weide and R. Davis, *Diamond and Related Materials*, 1996, **5**, 790-796.
20. K. P. Loh, I. Sakaguchi, M. Nishitani-Gamo, T. Taniguchi and T. Ando, *Diamond and related materials*, 1999, **8**, 781-784.
21. S. Dushman, *Reviews of Modern Physics*, 1930, **2**, 381.
22. O. W. Richardson, *On the Negative Radiation from Hot Platinum*, University Press, 1901.
23. J. F. Morris and D. L. Jacobson, *Thermionic energy conversion for space-power and terrestrial-topping applications*, INTELEC'84-International Telecommunications Energy Conference, IEEE, 1984, 43-47.
24. G. N. Hatsopoulos and J. Kaye, *Journal of Applied Physics*, 1958, **29**, 1124-1125.
25. O. Richardson, *Physical Review*, 1924, **23**, 153.
26. M. C. James, *Aluminium and oxygen termination of diamond for thermionic applications*, PhD thesis, University of Bristol, 2020.
27. R. L. Harniman, O. J. Fox, W. Janssen, S. Drijkoningen, K. Haenen and P. W. May, *Carbon*, 2015, **94**, 386-395.
28. W. Kang, J. Davidson, Y. Wong and K. Holmes, *Diamond and related materials*, 2004, **13**, 975-981.
29. C. Spindt, *Journal of Applied Physics*, 1968, **39**, 3504-3505.
30. R. Harniman, P. W. May and O. J. Fox, *Diamond and Related Materials*, 2017, **80**, 147-152.
31. V. S. Robinson, Y. Show, G. M. Swain, R. G. Reifenberger and T. S. Fisher, *Diamond and related materials*, 2006, **15**, 1601-1608.
32. K. Uppireddi, T. L. Westover, T. S. Fisher, B. R. Weiner and G. Morell, *Journal of Applied Physics*, 2009, **106**.

33. J. Voss, A. Vojvodic, S. H. Chou, R. T. Howe, I. Bargatin and F. Abild-Pedersen, *The Journal of Chemical Physics*, 2013, **138**.
34. T. D. Musho, W. F. Paxton, J. L. Davidson and D. G. Walker, *Journal of Vacuum Science & Technology B*, 2013, **31**.
35. O. C. Olawole and D. K. De, *Modeling thermionic emission from carbon nanotubes with modified Richardson-Dushman equation*, Nanoengineering: Fabrication, Properties, Optics, and Devices XIII, SPIE, 2016, 176-183.
36. G. N. Hatsopoulos, *The thermo-electron engine*, PhD thesis, Massachusetts Institute of Technology, 1956.
37. G. Hatsopoulos and E. Gyftopoulos, *Thermionic energy conversion. Volume II. Theory, technology, and application*, MIT Press, Cambridge, MA, 1979.
38. H. Dominguez-Andrade, A. Croot, G. Wan, J. A. Smith and N. A. Fox, *Review of Scientific Instruments*, 2019, **90**.
39. K. A. A. Khalid, T. J. Leong and K. Mohamed, *IEEE transactions on electron devices*, 2016, **63**, 2231-2241.
40. P. Shefsiek, *IEEE Transactions on Plasma Science*, 2010, **38**, 2041-2047.
41. R. Jenkins, *Vacuum*, 1969, **19**, 353-359.
42. J. Houston, *Journal of Applied Physics*, 1959, **30**, 481-487.
43. P. Tanner, D. Fraser and A. Irving, *IEE Proceedings-Science, Measurement and Technology*, 2005, **1**, 1-6.
44. F. A. Koeck and R. J. Nemanich, *Frontiers in Mechanical Engineering*, 2017, **3**, 19.
45. T. Zeng, *Applied physics letters*, 2006, **88**.
46. W. Raja, P. Zilio, A. Alabastri, R. P. Zaccaria, J. Cunha, T. Summerer, R. P. Zaccaria and L. Summerer, *Final Report, Istituto Italiano di Technologia (IIT)*, 2015, **5**, 20215.
47. M. Kataoka, C. Zhu, F. A. Koeck and R. J. Nemanich, *Diamond and Related Materials*, 2010, **19**, 110-113.
48. D. V. Paramonov and M. S. El-Genk, *Energy conversion and management*, 1997, **38**, 533-549.
49. A. Kribus and G. Segev, *Journal of Optics*, 2016, **18**, 073001.
50. O. Dunseath, E. Smith, T. Al-Jeda, J. Smith, S. King, P. W. May, A. H. Nobbs, G. Hazell, C. C. Welch and B. Su, *Scientific reports*, 2019, **9**, 8815.
51. A. Bellucci, P. Calvani, M. Girolami, S. Orlando, R. Polini and D. M. Trucchi, *Applied Surface Science*, 2016, **380**, 8-11.
52. E. Smith, A. Piracha, D. Field, J. W. Pomeroy, G. Mackenzie, Z. Abdallah, F.-P. Massabuau, A. Hinz, D. Wallis and R. A. Oliver, *Carbon*, 2020, **167**, 620-626.
53. M. Islam, O. T. Inal and J. R. Luke, *Journal of applied physics*, 2006, **100**.
54. F. A. Koeck, R. J. Nemanich and J. Sharp, *Doped diamond thin film electron sources for thermionic energy conversion*, 2013 26th International Vacuum Nanoelectronics Conference (IVNC), IEEE, 2013, 1-3.
55. W. F. Paxton, S. Ravipati, M. M. Brooks, M. Howell and J. L. Davidson, *Frontiers in Mechanical Engineering*, 2017, **3**, 18.
56. J.-H. Lee, I. Bargatin, N. A. Melosh and R. T. Howe, *Applied Physics Letters*, 2012, **100**.
57. A. Croot, G. Wan, A. Rowan, H. D. Andrade, J. A. Smith and N. A. Fox, *Frontiers in Mechanical Engineering*, 2017, **3**, 17.
58. S. Elfimchev, M. Chandran, R. Akhvediani and A. Hoffman, *physica status solidi (a)*, 2015, **212**, 2583-2588.
59. T. Sun, F. A. Koeck, C. Zhu and R. J. Nemanich, *Applied Physics Letters*, 2011, **99**.
60. N. Neugebohrn, T. Sun, F. A. Koeck, G. G. Hembree, R. J. Nemanich, T. Schmidt and J. Falta, *Diamond and related materials*, 2013, **40**, 12-16.
61. H. Kato, J. Hees, R. Hoffmann, M. Wolfer, N. Yang, S. Yamasaki and C. E. Nebel, *Electrochemistry communications*, 2013, **33**, 88-91.

62. A. Bellucci, P. Calvani, M. Girolami and D. Trucchi, *Defect engineering of diamond cathodes for high temperature solar cells*, 2015 IEEE 15th International Conference on Environment and Electrical Engineering (EEEIC), IEEE, 2015, 1616-1619.
63. C. Delfaure, M. Pomorski, J. De Sanoit, P. Bergonzo and S. Saada, *Applied Physics Letters*, 2016, **108**.
64. V. Bormashov, S. Y. Troschiev, S. Tarelkin, A. Volkov, D. Teteruk, A. Golovanov, M. Kuznetsov, N. Kornilov, S. Terentiev and V. Blank, *Diamond and Related Materials*, 2018, **84**, 41-47.
65. Y. J. Lu, C. N. Lin and C. X. Shan, *Advanced Optical Materials*, 2018, **6**, 1800359.
66. O. Loto, M. Florentin, C. Masante, N. Donato, M.-L. Hicks, A. Pakpour-Tabrizi, R. Jackman, V. Zuerbig, P. Godignon and D. Eon, *IEEE Transactions on Electron Devices*, 2018, **65**, 3361-3364.
67. P. Siyushev, M. Nesladek, E. Bourgeois, M. Gulka, J. Hruby, T. Yamamoto, M. Trupke, T. Teraji, J. Isoya and F. Jelezko, *Science*, 2019, **363**, 728-731.
68. F. Bundy, H. T. Hall, H. Strong and R. Wentorfjun, *nature*, 1955, **176**, 51-55.
69. J. E. Field, *Properties of Natural and Synthetic Diamond*, Elsevier Science, 1992.
70. P. W. May, *Philosophical Transactions of the Royal Society of London. Series A: Mathematical, Physical and Engineering Sciences*, 2000, **358**, 473-495.
71. P. W. May and Y. A. Mankelevich, *The Journal of Physical Chemistry C*, 2008, **112**, 12432-12441.
72. J. C. Angus, H. A. Will and W. S. Stanko, *Journal of Applied Physics*, 1968, **39**, 2915-2922.
73. D. J. Poflerl, N. C. Gardner and J. C. Angus, *Journal of Applied Physics*, 1973, **44**, 1428-1434.
74. B. Deryagin, D. Fodoseev, B. Spitsyn, L. Builov, A. Klochkov, A. Gurodetzki and S. AV, *Synthesis of diamond on non-diamond substrates*, Dokl. Akad. Nauk SSSR, 1976, 333-335.
75. B. Spitsyn, L. Bouilov and B. Derjaguin, *Journal of Crystal Growth*, 1981, **52**, 219-226.
76. S. Matsumoto, Y. Sato, M. Tsutsumi and N. Setaka, *Journal of materials Science*, 1982, **17**, 3106-3112.
77. Y. Saito, S. Matsuda and S. Nogita, *Journal of materials science letters*, 1986, **5**, 565-568.
78. M. Kamo, Y. Sato, S. Matsumoto and N. Setaka, *Journal of crystal growth*, 1983, **62**, 642-644.
79. M. Varga, S. Stehlik, O. Kaman, T. Izak, M. Domonkos, D. Lee and A. Kromka, *Carbon*, 2017, **119**, 124-132.
80. Y. Yu, L. Wu and J. Zhi, *Angewandte Chemie International Edition*, 2014, **53**, 14326-14351.
81. J. V. Macpherson, *Physical Chemistry Chemical Physics*, 2015, **17**, 2935-2949.
82. M. Suzuki, T. Ono, N. Sakuma and T. Sakai, *Diamond and Related Materials*, 2009, **18**, 1274-1277.
83. K. Larsson, *Electron Emission Studies of Scandium on Diamond for Thermionic Solar Energy Generation Devices, C*, 2020, **6**, 22.
84. W. F. Paxton, T. Wade, M. Howell, N. Tolk, W. P. Kang and J. L. Davidson, *physica status solidi (a)*, 2012, **209**, 1993-1995.
85. R. Telling, C. Pickard, M. Payne and J. Field, *Physical Review Letters*, 2000, **84**, 5160.
86. F. Maier, J. Ristein and L. Ley, *Physical Review B*, 2001, **64**, 165411.
87. K. Pandey, *Physical Review B*, 1982, **25**, 4338.
88. T. Ando, M. Ishii, M. Kamo and Y. Sato, *Journal of the Chemical Society, Faraday Transactions*, 1993, **89**, 1783-1789.
89. J. Van der Weide and R. Nemanich, *Applied physics letters*, 1993, **62**, 1878-1880.
90. B. D. Thoms, M. S. Owens, J. E. Butler and C. Spiro, *Applied Physics Letters*, 1994, **65**, 2957-2959.
91. J. Cui, J. Ristein and L. Ley, *Physical Review Letters*, 1998, **81**, 429.
92. C. Bandis and B. Pate, *Physical Review B*, 1995, **52**, 12056.
93. C. Bandis and B. Pate, *Surface science*, 1996, **350**, 315-321.
94. L. Diederich, P. Aebi, O. Küttel and L. Schlapbach, *Surface science*, 1999, **424**, L314-L320.
95. J. van der Weide, Z. Zhang, P. Baumann, M. Wensell, J. Bernholc and R. Nemanich, *Physical Review B*, 1994, **50**, 5803.
96. M. Rutter and J. Robertson, *Physical Review B*, 1998, **57**, 9241.
97. S. Sque, R. Jones and P. Briddon, *Physical review B*, 2006, **73**, 085313.
98. D. Zhu, L. Zhang, R. E. Ruther and R. J. Hamers, *Nature materials*, 2013, **12**, 836-841.
99. L. Zhang, D. Zhu, G. M. Nathanson and R. J. Hamers, *Angewandte Chemie*, 2014, **126**, 9904-9908.

100. S. Torrenzo, A. Miotello, L. Minati, I. Bernagozzi, M. Ferrari, M. Dipalo, E. Kohn and G. Speranza, *Diamond and related materials*, 2011, **20**, 990-994.
101. M. Geis, J. Twichell, J. Macaulay and K. Okano, *Applied physics letters*, 1995, **67**, 1328-1330.
102. A. K. Tiwari, J. Goss, P. Briddon, A. Horsfall, N. Wright, R. Jones and M. Rayson, *Europhysics Letters*, 2014, **108**, 46005.
103. K. Loh, J. Foord, R. Egdell and R. Jackman, *Diamond and Related Materials*, 1997, **6**, 874-878.
104. K. P. Loh, X. Xie, S. Yang, J. Pan and P. Wu, *Diamond and related materials*, 2002, **11**, 1379-1384.
105. W. E. Pickett, *Physical review letters*, 1994, **73**, 1664.
106. L. Diederich, O. Küttel, P. Aebi, E. Maillard-Schaller, R. Fasel and L. Schlapbach, *Diamond and related materials*, 1998, **7**, 660-665.
107. K. O'Donnell, T. Martin, N. Fox and D. Cherns, *Physical Review B*, 2010, **82**, 115303.
108. J. Nie, H. Xiao, X. Zu and F. Gao, *Chemical physics*, 2006, **326**, 308-314.
109. M. J. Sear, A. K. Schenk, A. Tadich, A. Stacey and C. I. Pakes, *Applied Physics Letters*, 2017, **110**.
110. T. L. Martin, *Lithium oxygen termination as a negative electron affinity surface on diamond: a computational and photoemission study*, PhD Thesis, University of Bristol, 2011.
111. K. M. O'Donnell, M. T. Edmonds, J. Ristein, A. Tadich, L. Thomsen, Q. H. Wu, C. I. Pakes and L. Ley, *Advanced Functional Materials*, 2013, **23**, 5608-5614.
112. K. M. O'Donnell, T. L. Martin, M. T. Edmonds, A. Tadich, L. Thomsen, J. Ristein, C. I. Pakes, N. A. Fox and L. Ley, *physica status solidi (a)*, 2014, **211**, 2209-2222.
113. K. M. O'Donnell, M. T. Edmonds, A. Tadich, L. Thomsen, A. Stacey, A. Schenk, C. I. Pakes and L. Ley, *Physical Review B*, 2015, **92**, 035303.
114. M. C. James, P. W. May and N. L. Allan, *Journal of Physics: Condensed Matter*, 2019, **31**, 295002.
115. P. Baumann and R. Nemanich, *Journal of applied physics*, 1998, **83**, 2072-2082.
116. P. Baumann and R. Nemanich, *Physical Review B*, 1998, **58**, 1643.
117. P. Baumann and R. Nemanich, *Applied surface science*, 1996, **104**, 267-273.
118. J. Van der Weide and R. Nemanich, *Journal of Vacuum Science & Technology B: Microelectronics and Nanometer Structures Processing, Measurement, and Phenomena*, 1992, **10**, 1940-1943.
119. A. K. Tiwari, J. Goss, P. Briddon, N. Wright, A. Horsfall and M. Rayson, *physica status solidi (a)*, 2012, **209**, 1697-1702.
120. W. M. Haynes, *CRC handbook of chemistry and physics*, CRC press, 2014.
121. F. Köck, J. Garguilo, B. Brown and R. Nemanich, *Diamond and related materials*, 2002, **11**, 774-779.
122. P. Baumann and R. Nemanich, *Diamond and related materials*, 1998, **7**, 612-619.
123. T. Sun, *Combined photo-and thermionic electron emission from low work function diamond films*, Arizona State University, 2013.
124. M. Z. Othman, *Studies of n-type doping and surface modification of CVD diamond for use in thermionic applications*, PhD thesis, University of Bristol, 2014.
125. J. Navas, D. Araujo, J. C. Piñero, A. Sánchez-Coronilla, E. Blanco, P. Villar, R. Alcántara, J. Montserrat, M. Florentin and D. Eon, *Applied Surface Science*, 2018, **433**, 408-418.
126. A. K. Tiwari, J. Goss, P. Briddon, N. G. Wright, A. B. Horsfall and M. Rayson, *Physical Review B*, 2012, **86**, 155301.
127. C. Mead and T. McGill, *Physics Letters A*, 1976, **58**, 249-251.
128. F. Himpsel, P. Heimann and D. Eastman, *Solid State Communications*, 1980, **36**, 631-633.
129. D. A. Evans, O. R. Roberts, A. R. Vearey-Roberts, D. P. Langstaff, D. Twitchen and M. Schwitters, *Applied Physics Letters*, 2007, **91**.
130. P. Lurie and J. Wilson, *Surface Science*, 1977, **65**, 499-510.
131. T. Matsumoto, H. Kato, K. Oyama, T. Makino, M. Ogura, D. Takeuchi, T. Inokuma, N. Tokuda and S. Yamasaki, *Scientific reports*, 2016, **6**, 31585.
132. A. Maréchal, M. Aoukar, C. Vallée, C. Rivière, D. Eon, J. Pernot and E. Gheeraert, *Applied Physics Letters*, 2015, **107**.
133. M. Imura, R. Hayakawa, E. Watanabe, M. Liao, Y. Koide and H. Amano, *physica status solidi (RRL)–Rapid Research Letters*, 2011, **5**, 125-127.

134. C. Pietzka, J. Scharpf, M. Fikry, D. Heinz, K. Forghani, T. Meisch, T. Diemant, R. J. Behm, J. Bernhard and J. Biskupek, *Journal of Applied Physics*, 2013, **114**.
135. C. Miskys, J. Garrido, C. Nebel, M. Hermann, O. Ambacher, M. Eickhoff and M. Stutzmann, *Applied physics letters*, 2003, **82**, 290-292.
136. J. M. A. Beattie, J. P. Goss, M. J. Rayson and P. R. Briddon, *Diamond and Related Materials*, 2019, **94**, 137-145.
137. K. M. O'Donnell, T. L. Martin and N. L. Allan, *Chemistry of Materials*, 2015, **27**, 1306-1315.
138. R. Zulkharnay, N. L. Allan and P. W. May, *Carbon*, 2022, **196**, 176-185.
139. R. Zulkharnay, *Electron Emission Studies of Scandium on Diamond for Thermionic Solar Energy Generation Devices*, PhD thesis, University of Bristol, 2023.
140. R. Zulkharnay and P. W. May, *Journal of Materials Chemistry A*, 2023.
141. A. Schenk, A. Tadich, M. Sear, K. M. O'Donnell, L. Ley, A. Stacey and C. Pakes, *Applied Physics Letters*, 2015, **106**.
142. A. Schenk, A. Tadich, M. Sear, D. Qi, A. Wee, A. Stacey and C. Pakes, *Nanotechnology*, 2016, **27**, 275201.
143. A. Schenk, M. Sear, A. Tadich, A. Stacey and C. Pakes, *Journal of Physics: Condensed Matter*, 2016, **29**, 025003.
144. J.-M. Zhang, H.-Y. Li, K.-W. Xu and V. Ji, *Applied Surface Science*, 2008, **254**, 4128-4133.
145. M. J. Sear, A. K. Schenk, A. Tadich, B. J. Spencer, C. A. Wright, A. Stacey and C. I. Pakes, *Journal of Physics: Condensed Matter*, 2017, **29**, 145002.
146. F. Maier, M. Riedel, B. Mantel, J. Ristein and L. Ley, *Physical review letters*, 2000, **85**, 3472.
147. T. Derry, N. Makau and C. Stampfl, *Journal of Physics: Condensed Matter*, 2010, **22**, 265007.
148. X. Zheng and P. Smith, *Surface science*, 1992, **262**, 219-234.
149. K. P. Loh, X. Xie, S. Yang and J. Zheng, *The Journal of Physical Chemistry B*, 2002, **106**, 5230-5240.
150. D. Shi, N. Huang, L. Liu, B. Yang, Z. Zhai, Y. Wang, Z. Yuan, H. Li, Z. Gai and X. Jiang, *Applied Surface Science*, 2020, **512**, 145652.
151. J. Robertson and M. Rutter, *Diamond and related materials*, 1998, **7**, 620-625.
152. M. Kaviani, P. Deák, B. Aradi, T. Frauenheim, J.-P. Chou and A. Gali, *Nano letters*, 2014, **14**, 4772-4777.
153. H. Dominguez-Andrade, J. Anaya, A. Croot, M. Cattelan, D. J. Twitchen, M. Kuball and N. A. Fox, *ACS applied materials & interfaces*, 2020, **12**, 26534-26542.
154. R. Yoshida, D. Miyata, T. Makino, S. Yamasaki, T. Matsumoto, T. Inokuma and N. Tokuda, *Applied Surface Science*, 2018, **458**, 222-225.
155. S. Falina, S. Kawai, N. Oi, H. Yamano, T. Kageura, E. Suaebah, M. Inaba, Y. Shintani, M. Syamsul and H. Kawarada, *Sensors*, 2018, **18**, 2178.
156. J.-H. Yang, Y. Nakano, Y. Murakami, K.-S. Song and H. Kawarada, *Journal of Nanoparticle Research*, 2008, **10**, 69-75.
157. Y. Tian and K. Larsson, *Journal of Material Sciences & Engineering*, 2019, **8**.
158. K. Ushizawa, Y. Sato, T. Mitsumori, T. Machinami, T. Ueda and T. Ando, *Chemical Physics Letters*, 2002, **351**, 105-108.
159. H. B. Man and D. Ho, *Journal*, 2012, **209**, 1609-1618.
160. S. M. Parks, R. R. Grote, D. A. Hopper and L. C. Bassett, *Diamond and Related Materials*, 2018, **84**, 20-25.
161. H. Koch, W. Kulisch, C. Popov, R. Merz, B. Merz and J. Reithmaier, *Diamond and related materials*, 2011, **20**, 254-258.
162. J. Yeh and I. Lindau, *Atomic data and nuclear data tables*, 1985, **32**, 1-155.
163. F. Li, Y. Li, D. Fan and H. Wang, *Applied Surface Science*, 2018, **456**, 532-537.
164. D. Zhu, J. A. Bandy, S. Li and R. J. Hamers, *Surface Science*, 2016, **650**, 295-301.
165. F. Fogarty, *Temperature Thermionic Emission from Modified Diamond Surfaces*, PhD thesis, University of Bristol, 2020.
166. G. Braunbeck, S. Mandal, M. Touge, O. A. Williams and F. Reinhard, *Diamond and Related Materials*, 2018, **85**, 18-22.

167. A. Stacey, K. O'Donnell, J. Chou, A. Schenk, A. Tadich, N. Dontschuk, J. Cervenka, C. Pakes, A. Gali and A. Hoffman, *Advanced Materials Interfaces*, 2015, **2**.
168. J.-P. Chou, A. Retzker and A. Gali, *Nano letters*, 2017, **17**, 2294-2298.
169. M. Gong, Q. Wang, N. Gao and H. Li, *Diamond and Related Materials*, 2021, **120**, 108601.
170. M. Attrash, M. K. Kuntumalla, S. Michaelson and A. Hoffman, *Surface Science*, 2021, **703**, 121741.
171. M. Attrash, M. K. Kuntumalla and A. Hoffman, *Surface Science*, 2019, **681**, 95-103.
172. J. B. Miller, *Surface Science*, 1999, **439**, 21-33.
173. M.-H. Hsu, H. Chuang, F.-Y. Cheng, Y.-P. Huang, C.-C. Han, J.-Y. Chen, S.-C. Huang, J.-K. Chen, D.-S. Wu and H.-L. Chu, *ACS Applied Materials & Interfaces*, 2014, **6**, 7198-7203.
174. T. Nakamura, T. Ohana, Y. Hagiwara and T. Tsubota, *Physical Chemistry Chemical Physics*, 2009, **11**, 730-734.
175. A. K. Tiwari, J. Goss, P. Briddon, N. G. Wright, A. B. Horsfall, R. Jones, H. Pinto and M. Rayson, *Physical Review B*, 2011, **84**, 245305.
176. C. Widmann, C. Giese, M. Wolfer, S. Kono and C. Nebel, *physica status solidi (a)*, 2014, **211**, 2328-2332.
177. K. J. Rietwyk, S. Wong, L. Cao, K. O'Donnell, L. Ley, A. Wee and C. Pakes, *Applied Physics Letters*, 2013, **102**.
178. T. Kondo, H. Ito, K. Kusakabe, K. Ohkawa, Y. Einaga, A. Fujishima and T. Kawai, *Electrochimica acta*, 2007, **52**, 3841-3848.
179. H. Kawarada and A. Ruslinda, *physica status solidi (a)*, 2011, **208**, 2005-2016.
180. Y. Wang, H. Huang, J. Zang, F. Meng, L. Dong and J. Su, *International Journal of Electrochemical Science*, 2012, **7**, 6807-6815.
181. V. N. Mochalin, O. Shenderova, D. Ho and Y. Gogotsi, *Nature Nanotechnology*, 2012, **7**, 11-23.
182. A. K. Tiwari, *Diamond-based thermo-tunnel devices for hostile environments*, PhD Thesis, Newcastle University, 2013.
183. J. B. Miller and D. W. Brown, *Langmuir*, 1996, **12**, 5809-5817.
184. M. Wang, M. R. Das, V. G. Praig, F. LeNormand, M. Li, R. Boukherroub and S. Szunerits, *Chemical communications*, 2008, 6294-6296.
185. M. R. Lockett and L. M. Smith, *Langmuir*, 2009, **25**, 3340-3343.
186. T. Strother, T. Knickerbocker, J. N. Russell, J. E. Butler, L. M. Smith and R. J. Hamers, *Langmuir*, 2002, **18**, 968-971.
187. S. Szunerits, N. Shirahata, P. Actis, J. Nakanishi and R. Boukherroub, *Chemical communications*, 2007, 2793-2795.
188. R. E. Ruther, M. L. Rigsby, J. B. Gerken, S. R. Hogendoorn, E. C. Landis, S. S. Stahl and R. J. Hamers, *Journal of the American Chemical Society*, 2011, **133**, 5692-5694.
189. I. Zegkinoglou, P. L. Cook, P. S. Johnson, W. Yang, J. Guo, D. Pickup, R. n. González-Moreno, C. Rogero, R. E. Ruther and M. L. Rigsby, *The Journal of Physical Chemistry C*, 2012, **116**, 13877-13883.
190. S. A. Yao, R. E. Ruther, L. Zhang, R. A. Franking, R. J. Hamers and J. F. Berry, *Journal of the American Chemical Society*, 2012, **134**, 15632-15635.
191. T. C. Kuo, R. L. McCreery and G. M. Swain, *Electrochemical and solid-state letters*, 1999, **2**, 288.
192. B. M. Nichols, J. E. Butler, J. N. Russell and R. J. Hamers, *The Journal of Physical Chemistry B*, 2005, **109**, 20938-20947.
193. S. Szunerits, C. E. Nebel and R. J. Hamers, *MRS Bulletin*, 2014, **39**, 517-524.
194. W. Kulisch, C. Popov, D. Gilliland, G. Ceccone, J. Reithmaier and F. Rossi, *Surface and Coatings Technology*, 2011, **206**, 667-675.
195. T. Knickerbocker, T. Strother, M. P. Schwartz, J. N. Russell, J. Butler, L. M. Smith and R. J. Hamers, *Langmuir*, 2003, **19**, 1938-1942.
196. S. Wenmackers, P. Christiaens, M. Daenen, K. Haenen, M. Nesladek, M. van de Ven, V. Vermeeren, L. Michiels, M. Ameloot and P. Wagner, *physica status solidi (a)*, 2005, **202**, 2212-2216.
197. W. Yang, S. E. Baker, J. E. Butler, C.-s. Lee, J. N. Russell, L. Shang, B. Sun and R. J. Hamers, *Chemistry of materials*, 2005, **17**, 938-940.

198. M. Liu, G. Zhao and Y. Qi, *International Journal of Environmental Analytical Chemistry*, 2012, **92**, 534-547.
199. Y. L. Zhong, K. P. Loh, A. Midya and Z.-K. Chen, *Chemistry of Materials*, 2008, **20**, 3137-3144.
200. H. Krysova, L. Kavan, Z. V. Zivcova, W. S. Yeap, P. Verstappen, W. Maes, K. Haenen, F. Gao and C. E. Nebel, *RSC advances*, 2015, **5**, 81069-81077.
201. G. Jarre, Y. Liang, P. Betz, D. Lang and A. Krueger, *Chemical communications*, 2011, **47**, 544-546.
202. D. Qi, L. Liu, X. Gao, T. Ouyang, S. Chen, K. P. Loh and A. T. Wee, *Langmuir*, 2007, **23**, 9722-9727.
203. E. Smith, *Growing Diamond on Unusual Substrates*, PhD thesis, University of Bristol, 2021.
204. T. Tsutsumoto, *Thin Solid Films*, 1998, **317**, 371-375.
205. S. Nunez-Sanchez, H. Dominguez Andrade, J. Harwood, I. Bickerton, N. A. Fox and M. J. Cryan, *Micro & Nano Letters*, 2018, **13**, 1325-1328.
206. Origin, Version 2024, OriginLab Corporation, Northampton, MA, USA.
207. C. A. Schneider, W. S. Rasband and K. W. Eliceiri, *Nature methods*, 2012, **9**, 671-675.
208. M. Roy, V. George, A. Dua, P. Raj, S. Schulze, D. Tenne, G. Salvan and D. Zahn, *Diamond and related materials*, 2002, **11**, 1858-1862.
209. S. Prawer and R. J. Nemanich, *Philosophical Transactions of the Royal Society of London. Series A: Mathematical, Physical and Engineering Sciences*, 2004, **362**, 2537-2565.
210. C. Su and J.-C. Lin, *Surface science*, 1998, **406**, 149-166.
211. M. T. Schulberg, C. A. Fox, G. D. Kubiak and R. H. Stulen, *Journal of applied physics*, 1995, **77**, 3484-3490.
212. W. Paxton, A. Steigerwald, M. Howell, N. Tolk, W. Kang and J. Davidson, *Applied Physics Letters*, 2012, **101**.
213. D. Koleske, S. Gates, B. Thoms, J. Russell Jr and J. Butler, *The Journal of chemical physics*, 1995, **102**, 992-1002.
214. V. Blank, V. Bormashov, S. Tarelkin, S. Buga, M. Kuznetsov, D. Teteruk, N. Kornilov, S. Terentiev and A. Volkov, *Diamond and Related Materials*, 2015, **57**, 32-36.
215. S. Wills, *Thermionic Emission Studies of Surface Functionalized Diamond Semiconductor Materials for the Production of Collectors in Thermionic Energy Converters*, MSci thesis, University of Bristol, 2022.
216. A. Ferrari and J. Robertson, *Physical review B*, 2001, **63**, 121405.
217. D. S. Knight and W. B. White, *Journal of Materials Research*, 1989, **4**, 385-393.
218. J. Filik, *Spectroscopy Europe*, 2005, **17**, 10.
219. T. Lopez-Rios, E. Sandre, S. Leclercq and E. Sauvain, *Physical review letters*, 1996, **76**, 4935.
220. A. Dychalska, P. Popielarski, W. Franków, K. Fabisiak, K. Paprocki and M. Szybowicz, *Mater. Sci.-Pol*, 2015, **33**, 799-805.
221. C. Wild, N. Herres and P. Koidl, *Journal of Applied Physics*, 1990, **68**, 973-978.
222. C. Davisson and L. Germer, *Physical Review*, 1922, **20**, 300.
223. M. Kataoka, N. Morioka, Y. Kimura, S. Sobue, H. Kato, D. Takeuchi and S. Yamasaki, *physica status solidi (a)*, 2016, **213**, 2650-2653.
224. A. Croot, *Boron and nitrogen in diamond: an ab initio simulation, plasma emission spectroscopy and material deposition & characterisation study*, PhD thesis, 2018
225. S. Abedrabbo, J. Hensel, O. Gokce, F. Tong, B. Sopori, A. Fiory and N. Ravindra, *MRS Online Proceedings Library*, 1998, **525**, 95-102.
226. A. Mohammed and A. Avin, *Scanning electron microscopy (SEM): A review*, Proceedings of the 2018 International Conference on Hydraulics and Pneumatics—HERVEX, *Băile Govora, Romania*. Vol. 2018. 2018.
227. S. Reich and C. Thomsen, *Philosophical Transactions of the Royal Society of London. Series A: Mathematical, Physical and Engineering Sciences*, 2004, **362**, 2271-2288.
228. R. Kostić, M. Mirić, T. Radić, M. Radović, R. Gajić and Z. Popović, *Acta Physica Polonica A*, 2009, **116**, 718-721.
229. P. Van der Heide, *Secondary ion mass spectrometry: an introduction to principles and practices*, John Wiley & Sons, 2014.

9. Appendix

9.1. CVD reactors

9.1.1. Hot Filament CVD

Hot filament (HF) reactors use filament wires to heat the growth surface. This occurs through the resistive heating of the filament, in this case Tungsten wire, to reach temperatures higher than 1500 °C. This temperature is sufficient for the CVD growth mechanism to be activated.

The space in the reactor used for this study is limited to two samples of 1 cm² and allows growth rates of approximately 0.5 μm h⁻¹. This specific reactor uses diborane as the boron supply to allow for the growth of boron-doped diamond. The diborane “contaminates” the reaction chamber with residual boron resulting in any diamond grown, even without diborane added into the reaction chamber, becomes lightly doped with diamond. Figure 9.1 shows the schematic design,⁷⁰ as well as a photograph of the reactor.

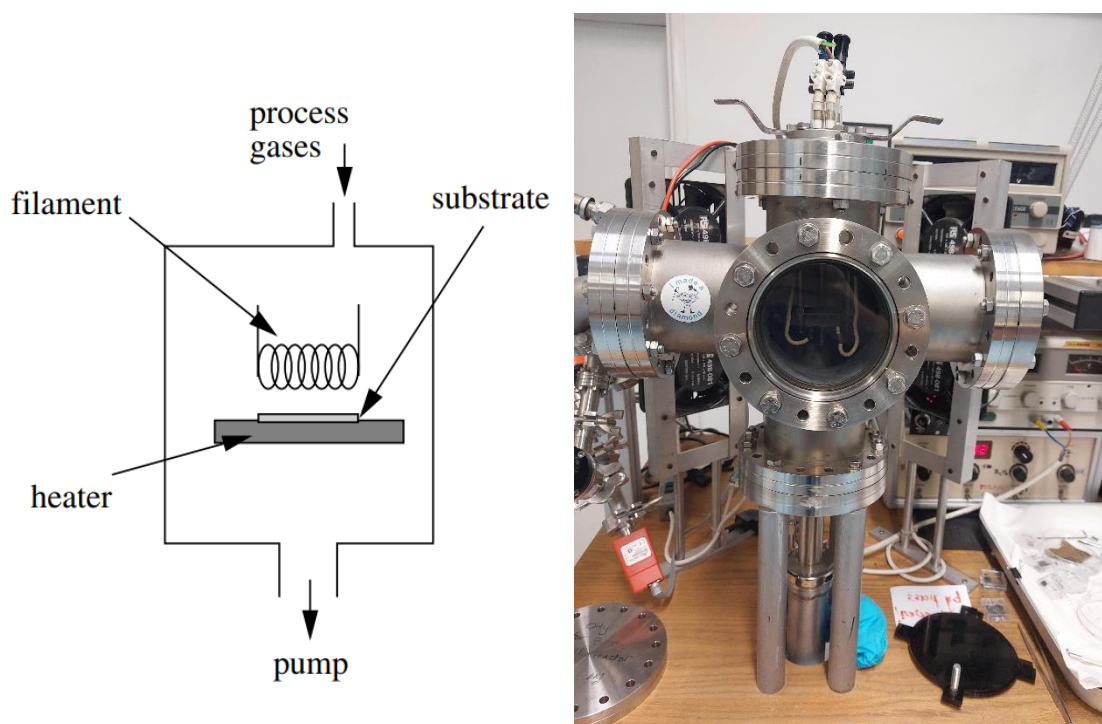


Figure 9.1: (left) Schematic of a hot filament reactor. Adapted from [70] (right) a photograph of the hot filament reactor used for the deposition of the boron-doped sample.

In this study, three tantalum filaments with a diameter of 0.25 mm were used (supplied by Advent Research Materials Ltd), tensioned above the substrate platform using springs. Tantalum is used due to its relatively low thermal expansions at temperatures and pressures suitable for diamond growth. The running conditions for this reactor are dependent on the current and voltage through the filament. This is usually approximately 25 A and 8 - 12 V (applied in parallel across the three filaments) resulting in an approximate power of 250 W when growth occurs. Growth will occur on any substrate below the filaments, an approximate area of 25 x 20 mm. However, for surface consistency, sample are usually kept to 10 x 10 mm. The samples are usually seeded to speed up the initiation of growth (see Section 3.1.), to increase the nucleation rate, and hence, the layer thickness for a certain growth

time. The substrate holder can be moved within the chamber to allow for different sample thicknesses. The optimal growth depth is taken to be 4 mm of separation between the filaments and sample surface.²⁰³

In order to reduce the chances of the filaments oxidising and breaking, the chamber is brought under vacuum for at least 60 minutes, achieving a minimum pressure of ~ 100 mTorr. This is achieved using a 2-stage rotary pump. The chamber and substrate holder are then heated for another 30 minutes to remove oxygen-containing species remaining in the chamber. This is to reduce the chance of the filaments breaking in the early growth stages.²⁰⁴ The filaments slowly carburised once the growth was started, changing their resistance. This then changed the applied voltage and power, requiring initial tuning to keep a consistent current flowing through the filaments. Standard growth conditions in this reactor are ~ 20 Torr, with a gas concentration of 1% CH₄ in H₂ (2 sccm and 200 sccm, respectively). For this study, only a low boron doping concentration was required. This meant that residual doping (doping using embedded boron-containing species embedded in the chamber walls) resulted in a sufficiently high doping concentration.

These gas concentrations were controlled using mass flow controllers (MFCs) for each gas separately. The gases flowed into the chamber through the side before being pumped out from the bottom of the chamber. This ensured that the activated gases flowed past the substrate after activation. This type of growth yielded high quality thin films with a high level of control over the diamond layer thickness. The standard growth rate is approximately $0.5 \mu\text{m h}^{-1}$. This study required lightly boron-doped films of several μm thick, achieved through deposition times of around 5 hours.

9.1.2. Microwave plasma-assisted CVD

Microwave plasma-assisted CVD takes a different approach. It uses microwaves to supply energy to gas phase electrons in the reaction chamber through a dielectric window (usually quartz). These gas phase electrons can then transfer that energy into the gas through collisions, forming a plasma that forms the reactive species required for CVD deposition.⁷⁰ This study used a 2.45 GHz ASTeX-type reactor, a schematic of which can be seen in Figure 9.2.²²⁴ In the reactor used for this study, the microwave source has a maximum power output of 2.00 kW with a Siemens power supply.

The operation of the MWCVD reactor is similar to the HFCVD reactor, with a few differences. In this case, the sample is placed on a disk, which is itself placed onto a spacer wire. In this study these were both Mo, with a spacer wire of a diameter of 8 mm. However, the same process was applied in reducing the chamber base pressure to ~ 200 mTorr. As the activation of the gaseous species occurs through a plasma ball located directly above the sample, the plasma needs to be created before growth occurs. The "striking" conditions for a hydrogen plasma are approximately 15 Torr (H₂ only) and 0.70 kW. This results in a purple plasma. Once this plasma is seen, the pressure is increased slowly to reduce sample etching from the bombardment of electrons and ions. This increased pressure shrinks the plasma; hence, the power is slowly increased. This process increases in a stepwise manner until the pressure reaches ~ 50 Torr. At this stage, the relevant concentrations of CH₄ and N₂ are added. They are not present initially, as it is found that the plasma is easier to strike, and is more stable, in pure H₂ conditions.²⁰³ This addition is clearly noticeable as the plasma turns a pale green, starting from the top of the plasma. The pressure and power are then increased together until growth conditions of 100 - 150 Torr and 1000 - 2000 W are reached. Standard growth

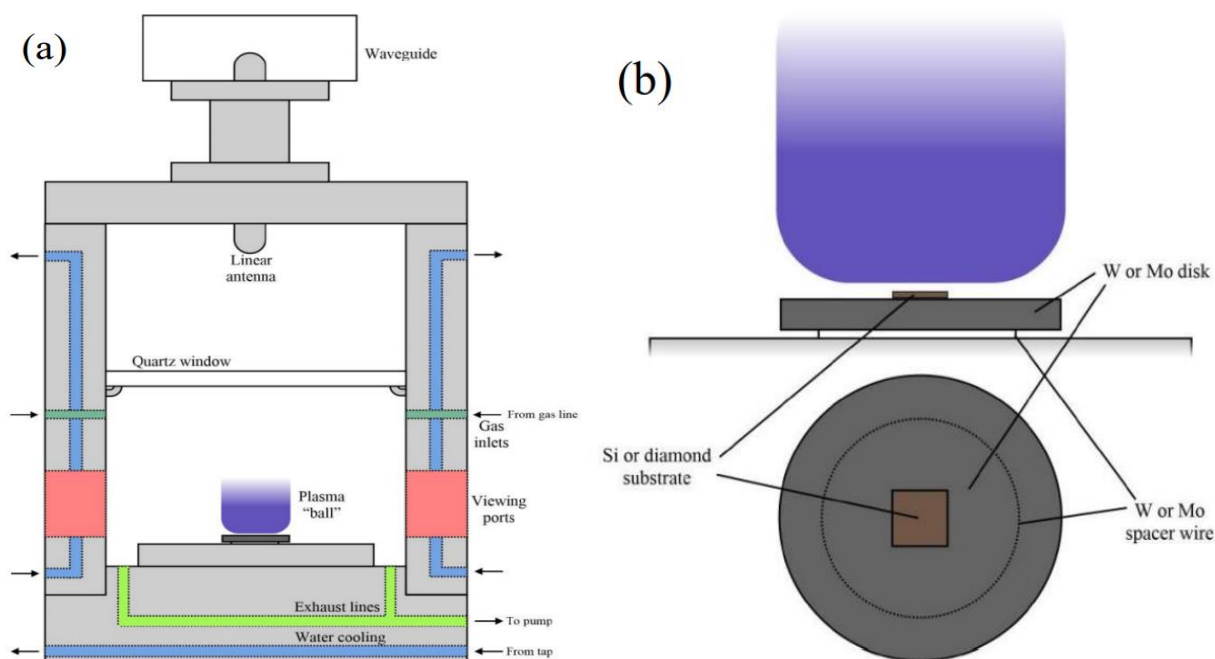


Figure 9.2: A schematic of a microwave plasma CVD reactor, as well as the substrate holder. Image from reference [57].

conditions occur at 300 sccm (standard cubic centimetres per minute) and 12.5 sccm of H_2 and CH_4 , respectively. The flow rate of any dopant gases can be adjusted. For this study, as lightly doped samples were required, a maximum N_2 flow rate of 4.0 sccm was used. Initially, the samples needed to be H-terminated. This was achieved at the end of the deposition by stopping the flow of the CH_4 and N_2 for c. 30 s before the shutdown procedure started. The sample can be re-terminated with hydrogen by creating a H_2 plasma at a high temperature, $>900\text{ }^\circ\text{C}$, to etch off any oxidation that occurred. By then dropping the temperature to $\sim 550\text{ }^\circ\text{C}$ for several minutes, a new hydrogen termination can be processed. (See Table 4.2)

The substrate temperature can be estimated using a $2.2\text{ }\mu\text{m}$ -wavelength one-colour pyrometer. This compares the material's emitted radiation to what would be emitted by a black body under the same conditions. This ratio is called the emissivity, the value of which is well-documented for various materials.²²⁵ However, the emissivity is dependent on the surface morphology, as well as the thickness of a materials. This means that as the diamond layer grows, a large uncertainty is introduced on estimations of the surface temperature.

The diamond growth rate for MWCVD is faster than for HFCVD, with a maximum growth rate of $20\text{ }\mu\text{m h}^{-1}$ achievable. Usually, growth rates of $2 - 5\text{ }\mu\text{m h}^{-1}$ are observed, however. Finally, the substrate materials, size, and shape are a lot more significant in MWCVD than in HFCVD.²⁰³ The plasma ball has a limited size within the reaction chamber and the temperature can be more variable towards its extremities. Therefore, sample sizes in this study are kept to $10 \times 10\text{ mm}$, to ensure that the whole sample has identical growth conditions.

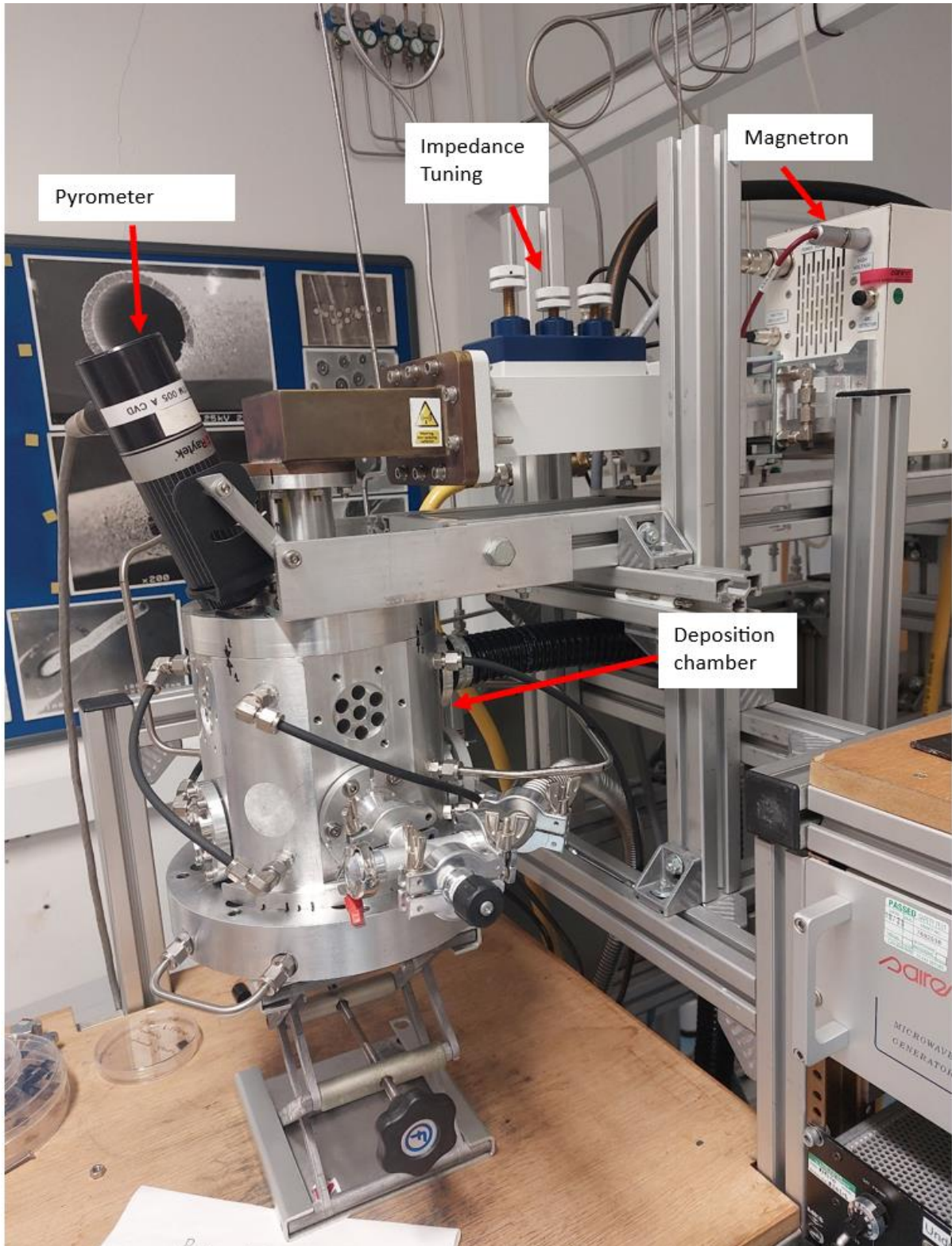


Figure 9.3: Labelled photograph of the reaction chamber on the microwave plasma reactor.

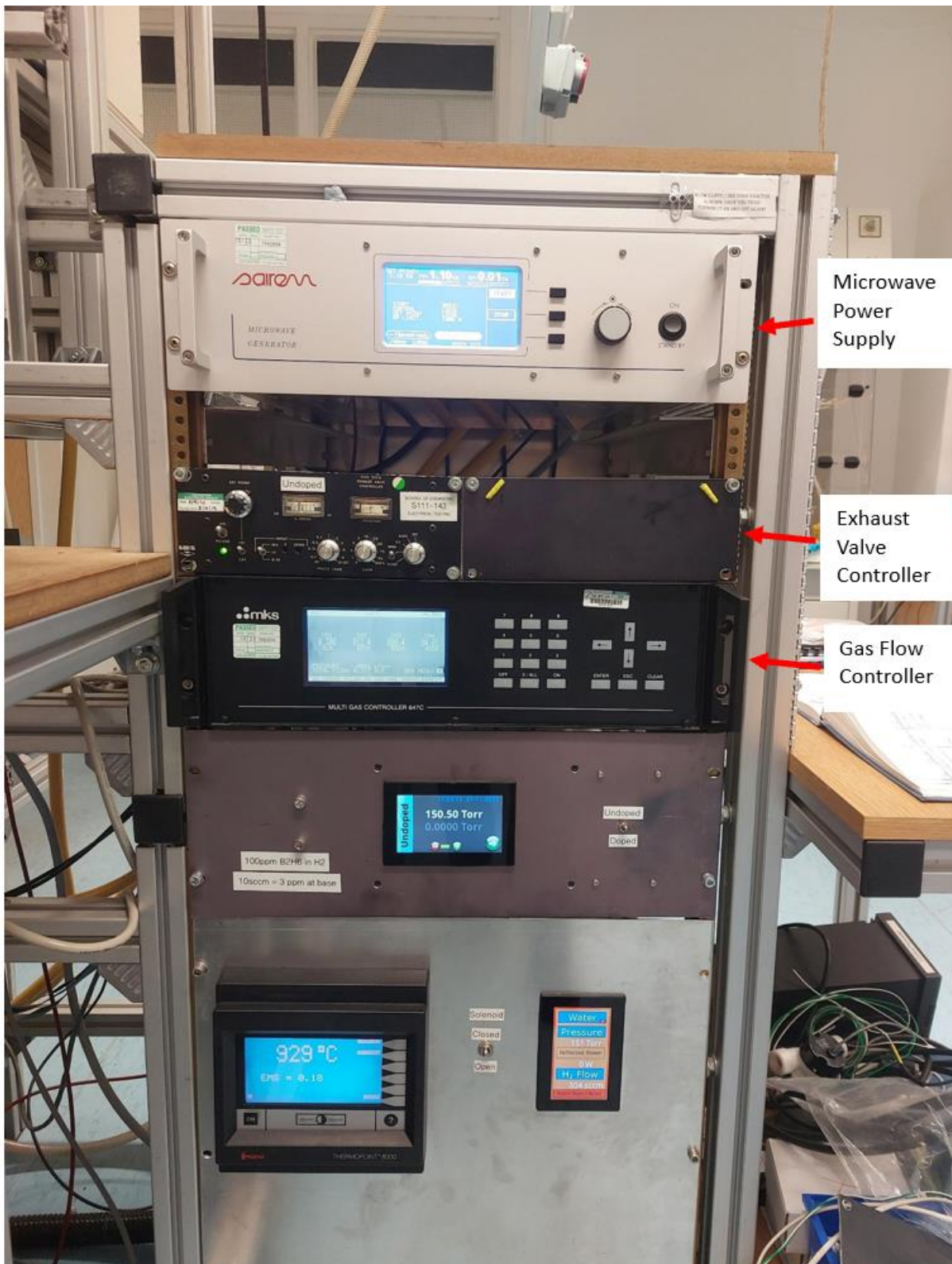


Figure 9.4: Labelled photograph of the control stack for the microwave plasma reactor during deposition.

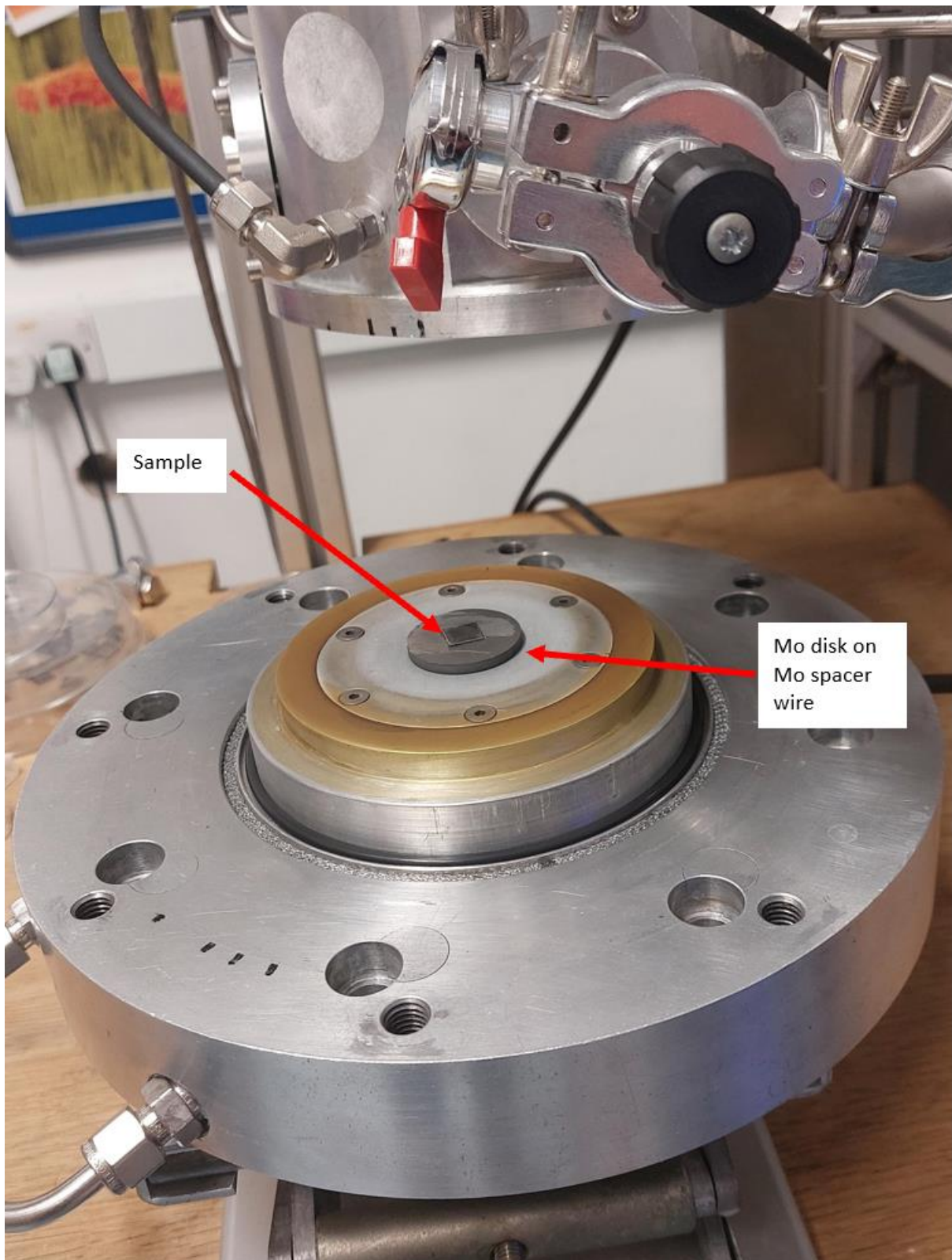


Figure 9.5: Labelled photograph of the internal reaction chamber.

9.2. Characterisation Techniques

9.2.1. Scanning Electron Microscopy (SEM)

SEM is one of the most useful characterisation techniques for diamond as it allows for the imaging of the diamond surfaces at a higher resolution than would be possible using visible light microscopy. A schematic of a generic scanning electron microscope is shown in Figure 9.6. A high-energy electron beam (100 - 30,000 eV) is generated through the heating of a filament under high vacuum. Using electromagnetic lenses, the electron beam is focused into a spot with a diameter $<10\ \mu\text{m}$, which penetrates up to a depth of $1\ \mu\text{m}$.²²⁶ When these electrons hit the sample they scatter, resulting in the further ejection of secondary electrons. The image is then collected point-by-point, through the movement of the detector, which collects the secondary electrons and measures their intensities. This results in an image with a resolution of $\sim 50\ \text{nm}$ being formed in 2D. For doped samples that are conductive, no adjustment is needed, however, undoped diamond is an insulator and is usually sputtered with a thin layer of gold or silver to reduce the charging.²⁰³ In the context of this study, even the undoped sample did not require sputtering as the sample was thin enough so that not much charging would have developed.

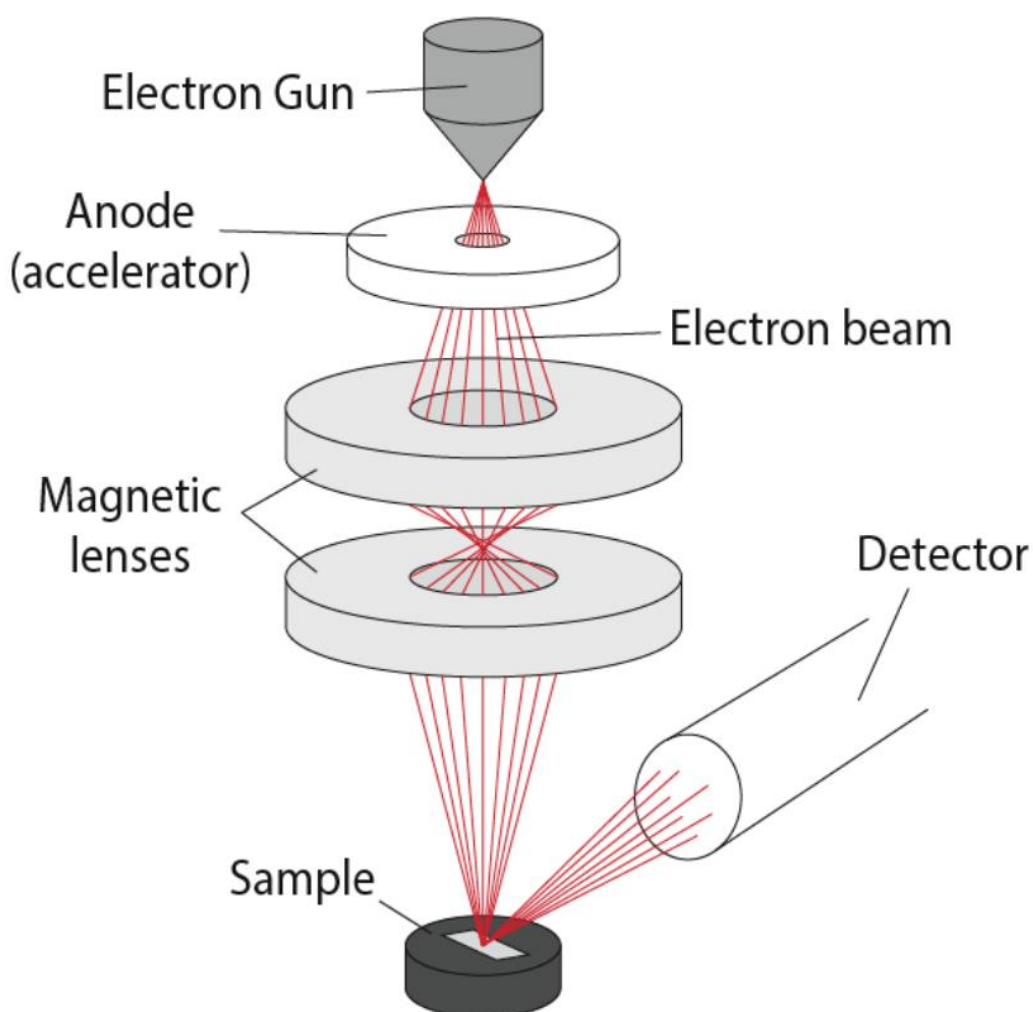


Figure 9.6: Schematic of a scanning electron microscope. Image from reference [203].

9.2.2. Raman Spectroscopy

Raman spectroscopy is a non-destructive method for the quantitative analysis of CVD diamond. It uses lasers of known wavelengths (514 nm in this study) that interacts with the diamond structure to give characteristic peaks. These peaks are well-documented for both sp^2 and sp^3 carbon structures, as well as for doped diamond films. These peaks occur due to a shift in the polarisability of the diamond when the high energy photon interacts with a phonon-mode of the crystal structure.²⁰³ It is also possible to obtain quantitative information for the diamond film through the integration of the characteristic peaks, as well as through the measurement of the full-width half-maximum (FWHM). However, this study focuses on the position of the peaks in order to characterise the surface of the film. The Raman spectra are therefore only used to identify the characteristic peaks.

One of these key characteristic peaks is the first-order diamond (sp^3) peak which for undoped diamond occurs at 1332 cm^{-1} .²⁰⁹ This type of peak is uncommon as it is due to polarisability in the diamond structure. In other words, the peaks are due to an induced dipole moment within the sample. At longer laser wavelengths, the sp^3 peak becomes less prominent and the sp^2 peaks dominate. These graphitic peaks occur due to a different mechanism than the diamond peak.^{227, 228} It is worth noting that doping the diamond sample can result in the appearance of the 'D' peak at $\sim 1370\text{ cm}^{-1}$ and a slight shift of the 'G' and diamond peaks.

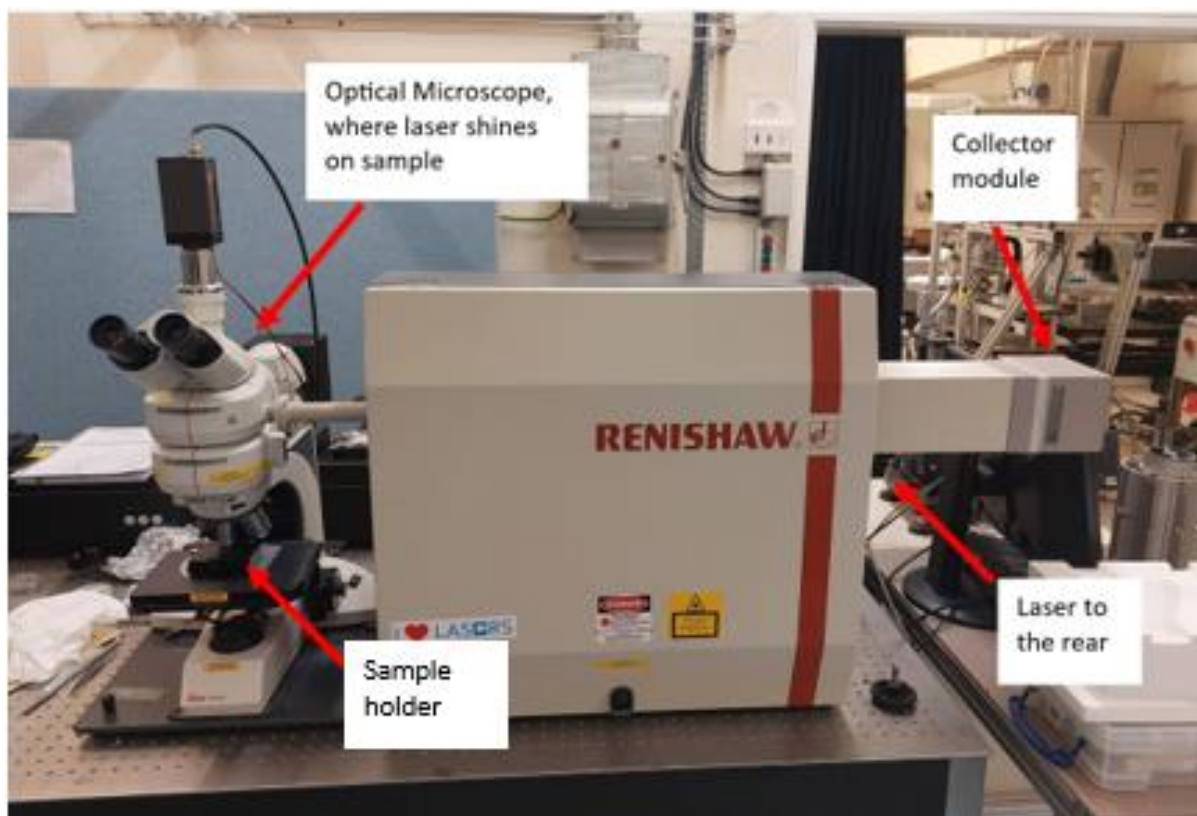


Figure 9.7: Labelled photograph of the Renishaw 2000 spectrometer.

9.2.3. Thermionic Emission Simulator Kit (TECsim)

The homebuilt TECsim kit consists of three modules: the emitter/collector chamber, the laser heating system, and the current measuring component. The heating system consists of an infrared CO₂ laser with a wavelength of 10.6 μm and a maximum power of 40 W (Synrad FSV40KFD, Firestar), shown in Figure 9.8. Three gold-coated copper mirrors reflect the polarized laser onto the reverse side of the sample through the quartz window of the emitter/collector chamber. This chamber is made from stainless steel and is evacuated by turbomolecular and scroll pumps. This allows a base pressure of the order 10⁻⁷ Torr to be achieved.¹³⁹ A 10 x 10 mm sample, which becomes the cathode in this system, is mounted in the centre of a quartz plate by two diagonally placed Mo clamps above a circular hole of diameter 8 mm. This sample holder system is shown in Figure 9.9.



Figure 9.8: Photograph of the Synrad FSV40KFD, Firestar laser.

The current density was measured using a cylindrical shaped tungsten collector (10 mm diameter), though other materials and sizes can also be used.¹³⁹ The collector (anode) is situated just above the sample with a fixed separation, which can be adjusted using a stepper motor (Z825BV, Thorlabs, Inc.) both outside the chamber, and under vacuum. The sample/collector system (Figure 9.9) is connected to a DC power supply (HY3003D) and an ammeter (Keithley Model 2750). This allows the current to be measured to an accuracy of ±0.01 μA.

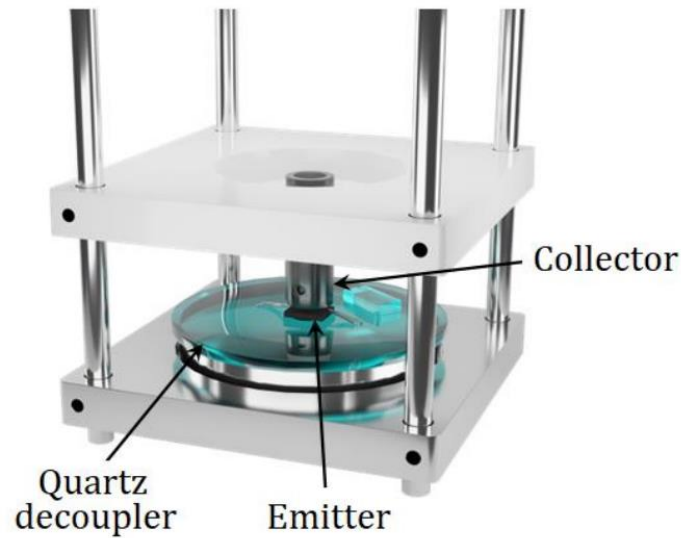


Figure 9.9: Close-up image of the emitter-collector module. Image from work by Zulkharnay. [139]

Finally, the temperature of the sample is measured using a two-colour IR pyrometer (Spotmeter R160, Land Instruments International Ltd.). This specific model has two detection modes at different wavelengths: $\lambda_1 = 1.0 \mu\text{m}$ and $\lambda_2 = 1.5 \mu\text{m}$. This model allows the two wavelengths to be used simultaneously for temperature detection in the range 250 – 1600 °C. The accuracy can be further improved by setting the emissivity of the sample (0.125 in the case of a Mo substrate). The emitter temperature is controlled using LabVIEW virtual software in real time. The laser output power, proportional integral derivative (PID), pyrometer, ammeter, and pressure gauges can all be operated during the emission. The PID controller adjusts the laser power in order to keep the temperature at a specific, pre-programmed temperature (the setpoint). A more in-depth review of this equipment can be found in references [38] and [139].^{38, 139}

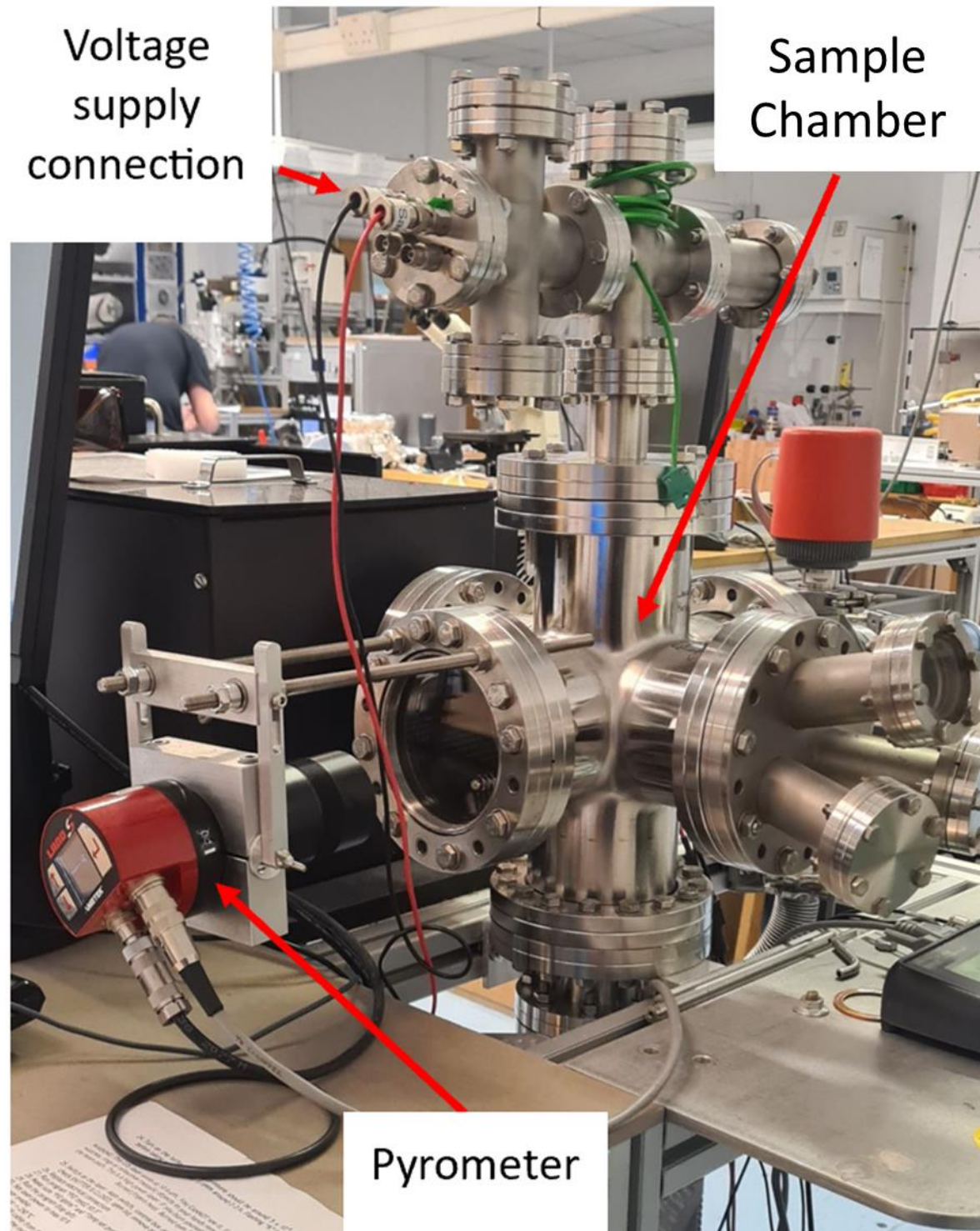


Figure 9.10: Labelled photograph of the homebuilt thermionic energy conversion simulator chamber.

9.2.4. Secondary Ion Mass Spectrometry (SIMS)

SIMS is slightly more destructive as a characterisation technique, in the sense that the sample is unusable for thermionic emission after characterisation. However, it can characterise, as well as determine, the spatial distribution of the elements that form a solid material. It occurs under high vacuum and can detect any element up to, and including, uranium. It works by bombarding the sample with a high energy ion beam (primary ions) resulting in the generation of charged species (secondary ions) that can be identified via their mass/charge (m/z) ratio. The technique is sensitive enough to determine the distribution of dopant atoms in thin films, providing valuable information about the sample uniformity. The spectrometer used can perform both positive (positively charged primary ions) as well as negative (negatively charged primary ions) spectroscopy. The energy of the ion beam is approximately 30 keV and is incident on the sample at 45°. The secondary beam current is measured using a picoammeter (Keithley Model 6482) with it being analysed in a Faraday cup. Spectra from this machine also allow determination of the dopant density, as well as the distribution with depth.

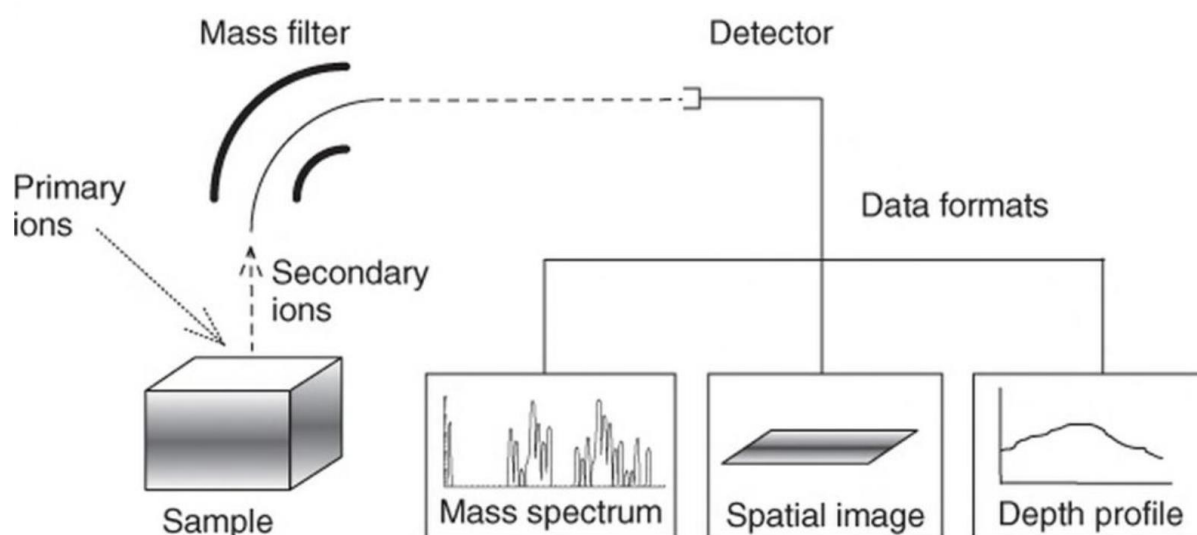


Figure 9.11: Pictorial representation of the secondary ion mass spectrometer and the types of data that can be obtained from it. Image from reference [229].

9.2.5. Photoelectron Spectroscopy

Photoelectron spectroscopy uses photons to investigate the properties of solid samples. The photon interacts with an electron in the sample, transferring energy to that electron and resulting in its emission. The information that photoelectron spectroscopy supplies depends on the energy of the emitted electron. X-ray photoelectron spectroscopy (XPS) uses soft x-rays with photon energies between 200 - 2000 eV to examine the core electrons. Ultra-violet photoelectron spectroscopy (UPS) uses ultraviolet photons with photon energies of 10 - 45 eV to examine only the valence electrons. For both cases, the analysis of the composition and electronic states of the atoms in the surface layer are done by looking at the kinetic energy (KE) of the emitted electrons. The KE of the emitted electron is related to the binding energy of each electron, which in turn relates to the work function of the

material. XPS and UPS are extensively reported and studied and so the characteristic peaks for every atom/bond are well known. XPS is able to examine core electrons meaning that its sensitivity decreases. It can detect any element between lithium and uranium, but hydrogen and helium have electron energies that are too low to be distinguishable.²²⁹ UPS does allow for the detection of hydrogen and helium in the gas phase, however. They are therefore often used in conjunction for samples that contain hydrogen.

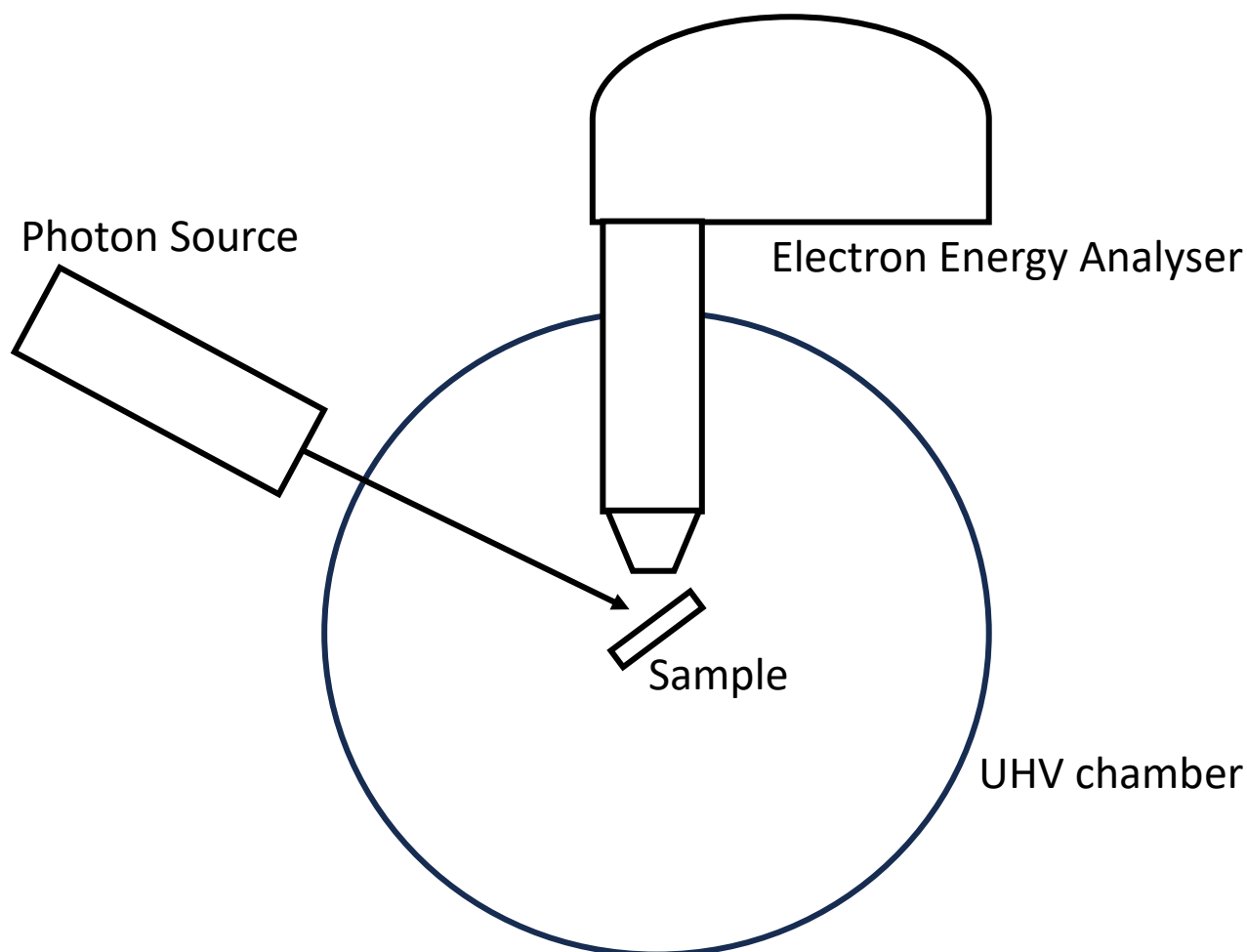


Figure 9.12: Simplified schematic of a photoelectron spectrometer.

Figure 9.12 shows a simplified schematic for generic photoelectron spectroscopy equipment. It is made up of a photon source, a high vacuum chamber, and an electron energy analyser. There are many different types of electron analyser but all of them disperse the emitted electrons according to their kinetic energy. This allows for the plotting of the flux of emitted electrons against their kinetic energy.

9.3. Additional Results, Analyses, and Raw Data

9.3.1. Raman Spectra

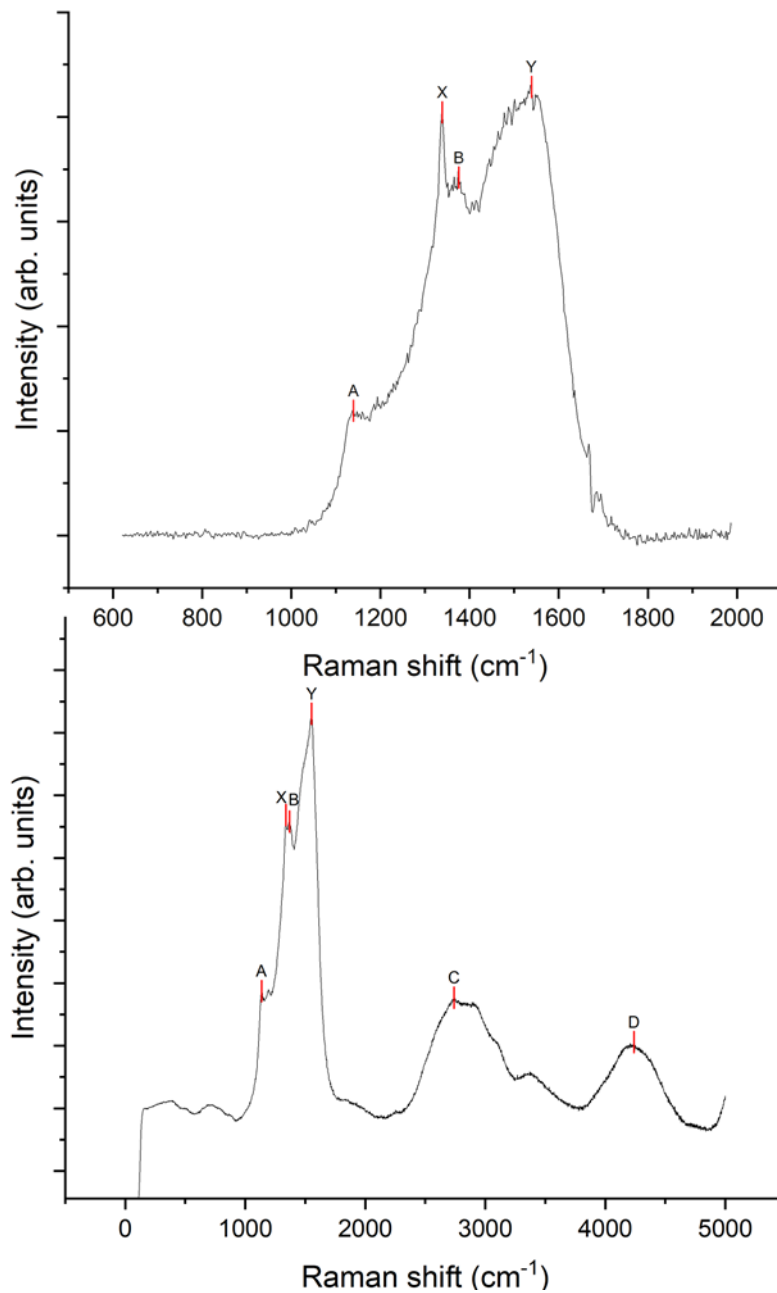


Figure 9.13: (top) Static Raman spectrum and **(bottom)** extended Raman spectrum for a PDD sample (N21136). **X** – diamond peak at c. 1338 cm^{-1} and **Y** – ‘G’ band at 1540 cm^{-1} . Characteristic peaks were also identified at 1370 cm^{-1} (**B**), 2800 cm^{-1} (**C**), and 4200 cm^{-1} (**D**). For details see main text.

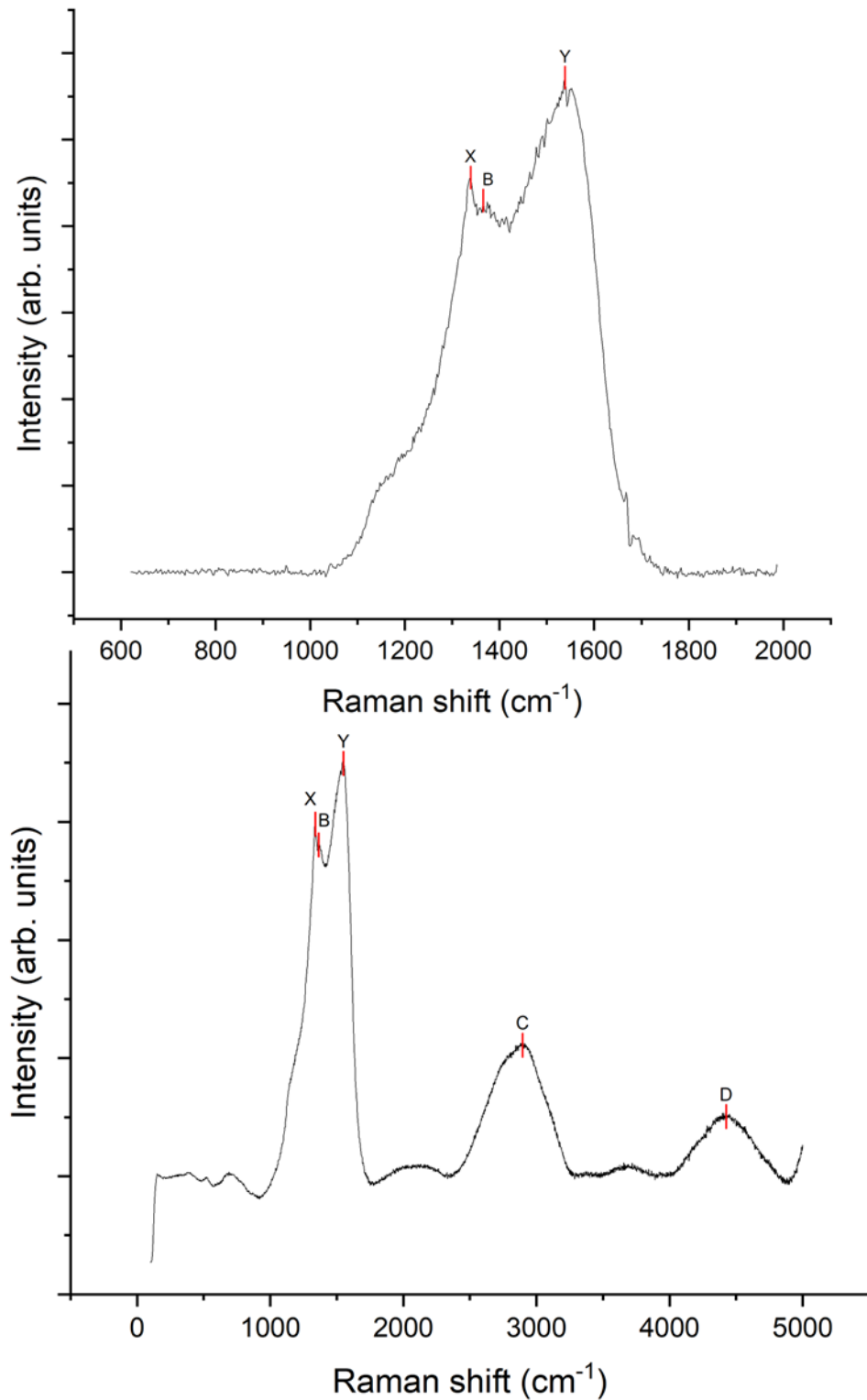


Figure 9.14: (top) Static Raman spectrum and **(bottom)** extended Raman spectrum for a PDD sample (N21139). **X** – diamond peak at c. 1338 cm⁻¹ and **Y** – ‘G’ band at 1540 cm⁻¹. Characteristic peaks were also identified at 1370 cm⁻¹ (**B**), 2900 cm⁻¹ (**C**), and 4400 cm⁻¹ (**D**). For details see main text.

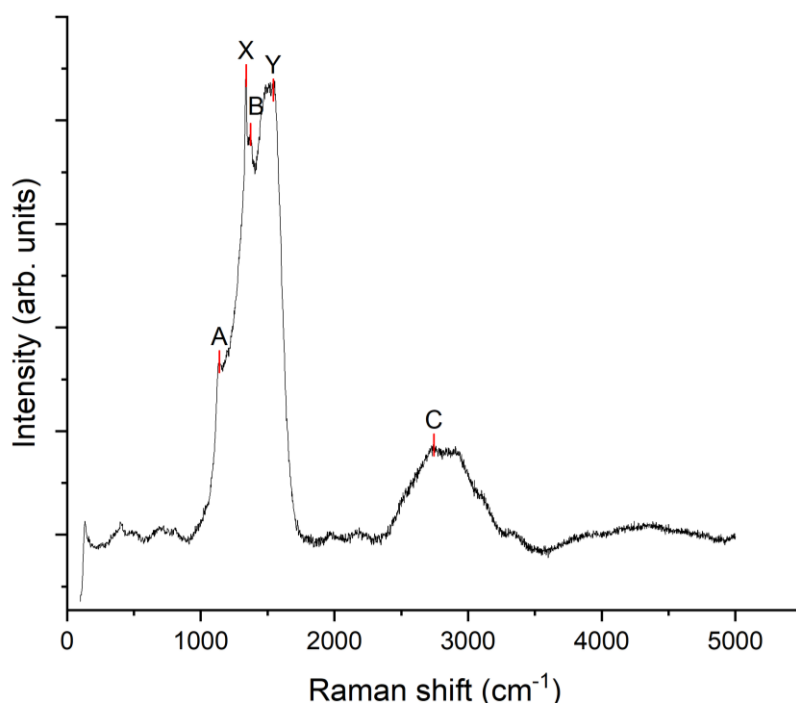


Figure 9.15: Extended Raman spectrum for a PDD sample (N21134) after thermionic analysis. **X** – diamond peak at c. 1338 cm⁻¹ and **Y** – ‘G’ band at 1540 cm⁻¹. Characteristic peaks are also observed at **A**, **B**, and **C**. For details see main text.

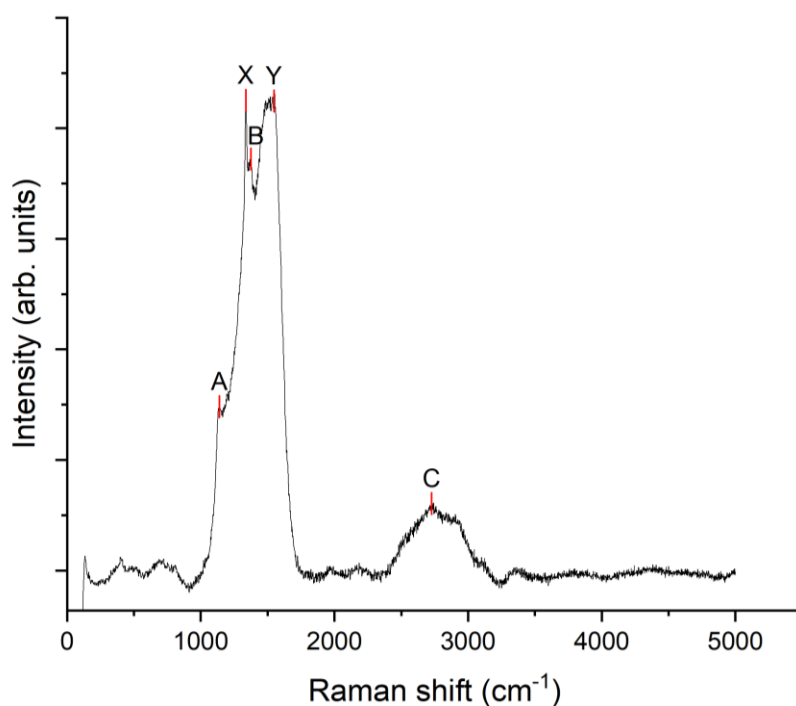


Figure 9.16: Extended Raman spectrum for a PDD sample (N21136) after thermionic analysis. **X** – diamond peak at c. 1338 cm⁻¹ and **Y** – ‘G’ band at 1540 cm⁻¹. Characteristic peaks are also observed at **A**, **B**, and **C**. For details see main text.

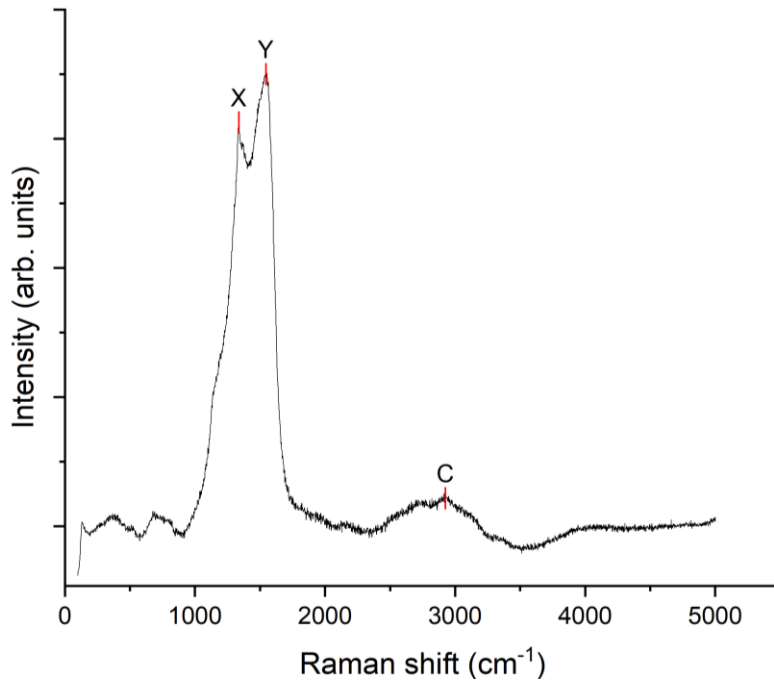


Figure 9.17: Extended Raman spectrum for a PDD sample (N21139) after thermionic analysis. **X** - diamond peak at c. 1338 cm^{-1} and **Y** – ‘G’ band at 1540 cm^{-1} . A characteristic peak is also observed at **C**. For details see main text.

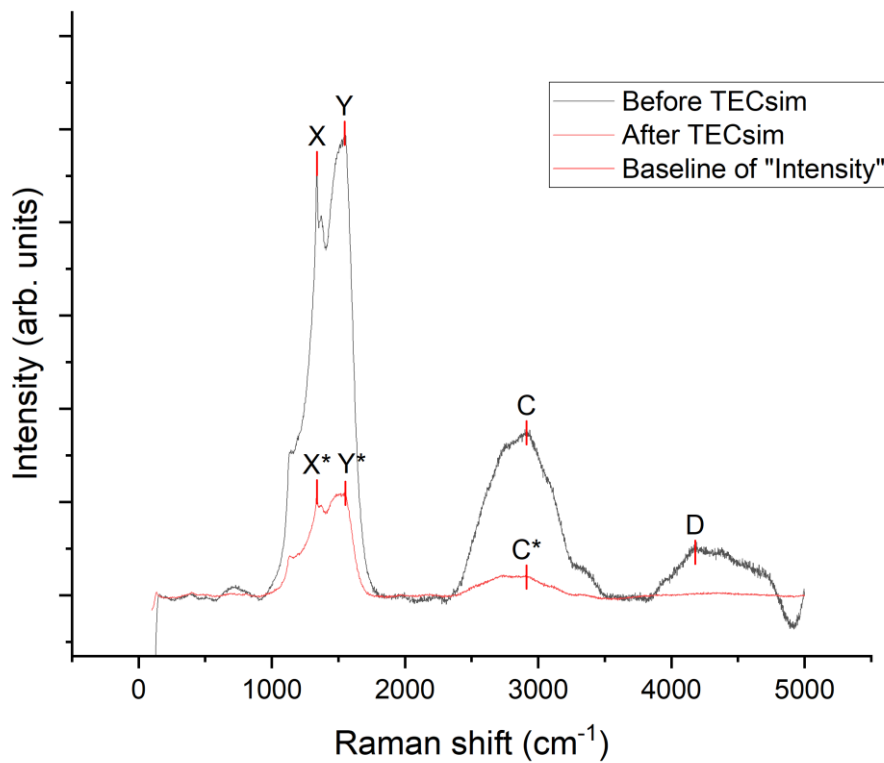


Figure 9.18: Extended Raman spectra for a PDD sample (N21134) before and after TECsim analysis. For details see main text.

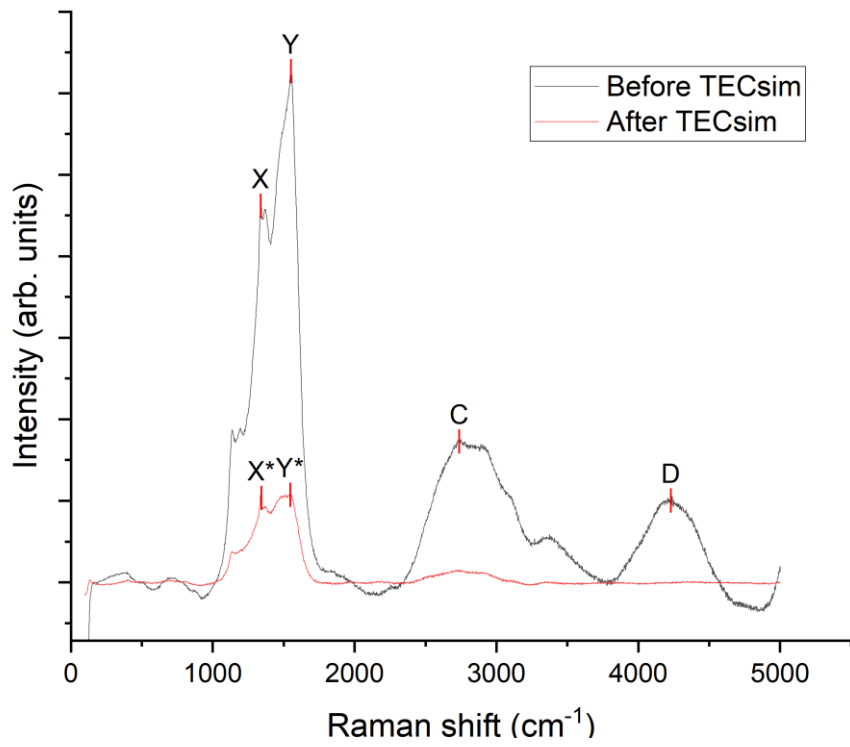


Figure 9.19: Extended Raman spectra for a PDD sample (N21136) before and after TECsim analysis. For details see main text.

9.3.2. SEM

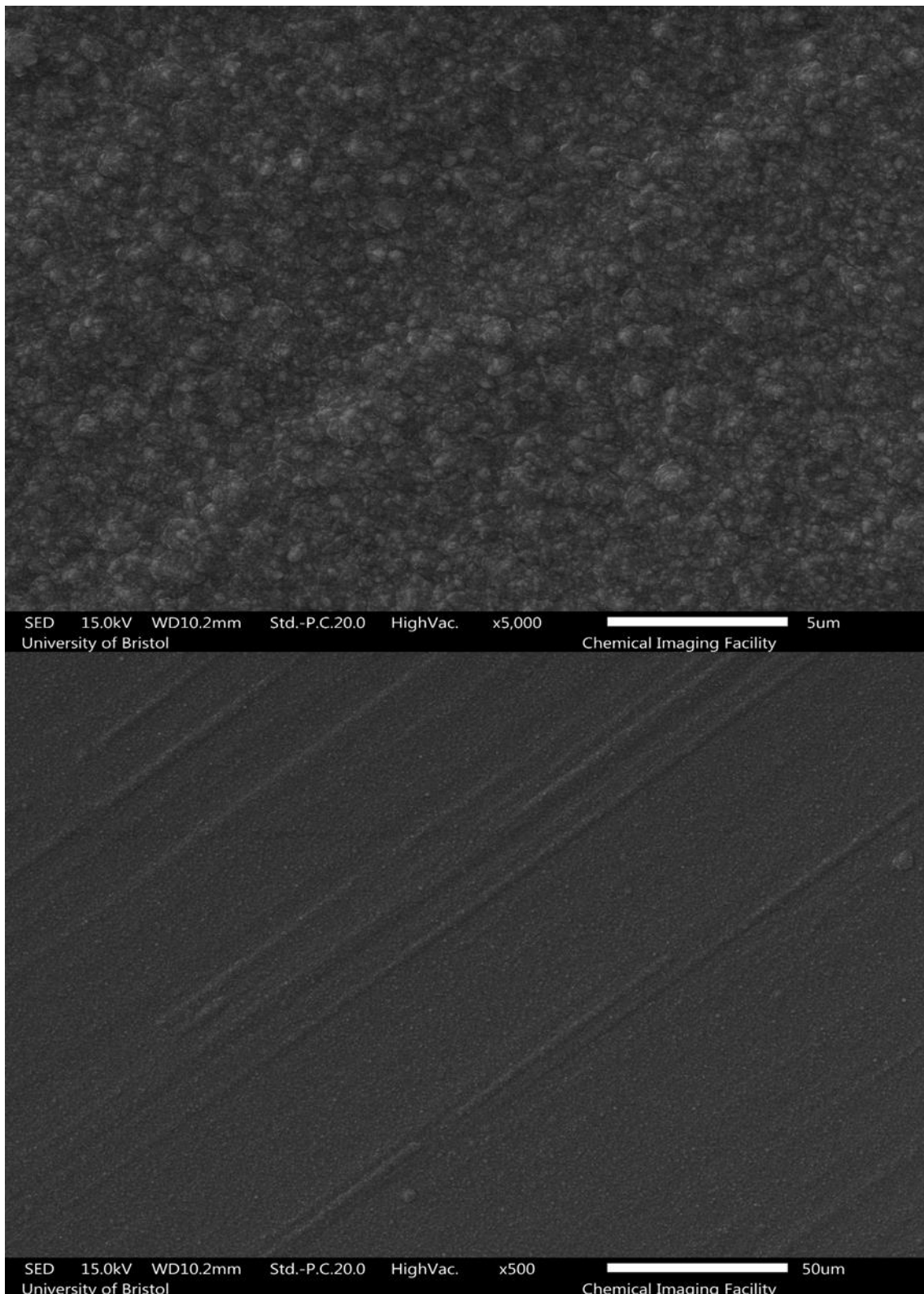


Figure 9.20: SEM images of a manually abraded P-doped sample (N21136) at **(top)** x5000 magnification and **(bottom)** x500 magnification. Striations can be seen through the diamond layer indicating a maximum film thickness of c. 1 μm .

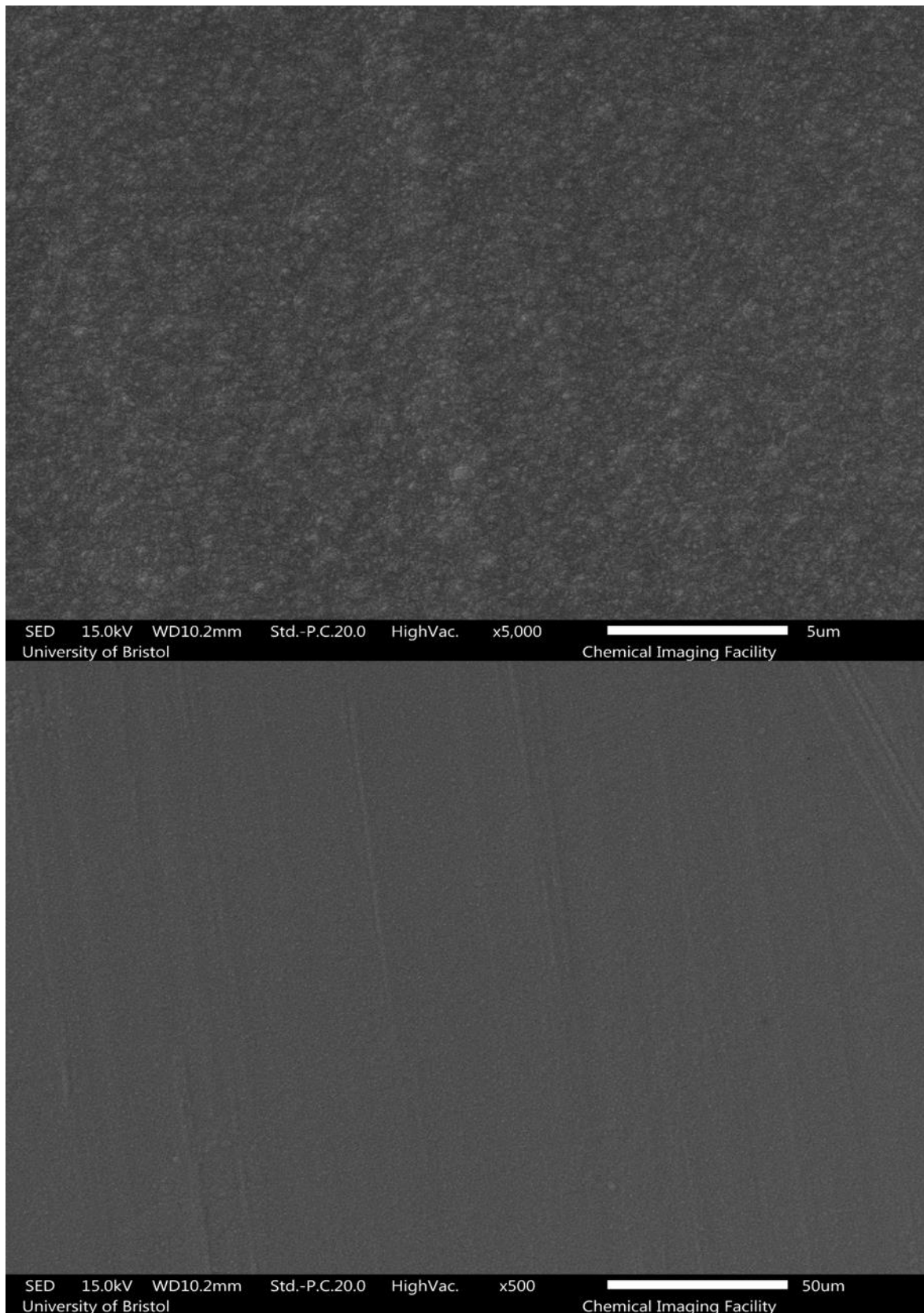


Figure 9.21: SEM images of a manually abraded P-doped sample (N21139) at **(top)** x5000 magnification and **(bottom)** x500 magnification. Striations can be seen through the diamond layer indicating a maximum film thickness of c. 1 μm .

9.3.3. Grain size analysis

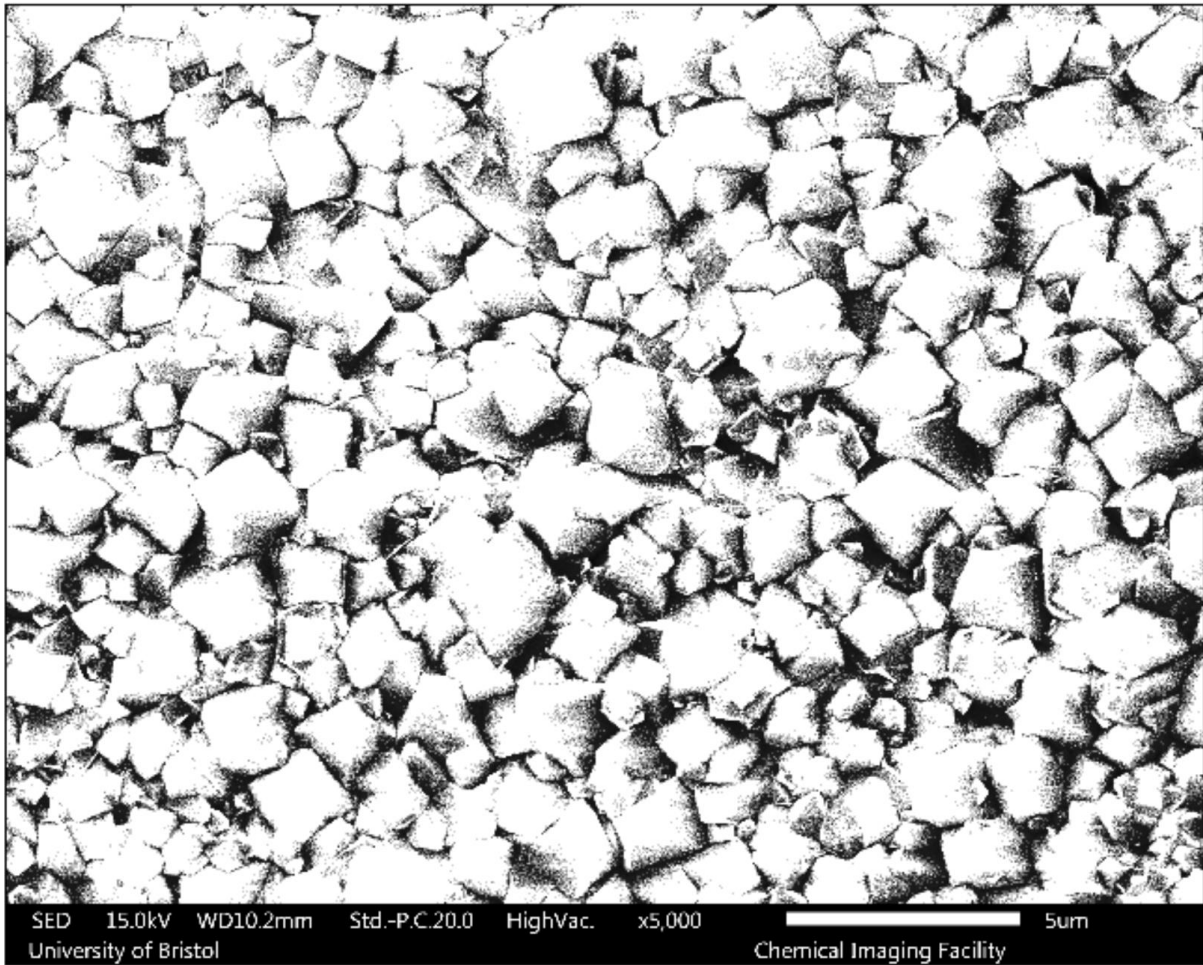


Figure 9.22: Contrast image for the grain size determination of the undoped sample.

Table 9.1: Calculated grain sizes and errors for the undoped diamond sample.

	Area (nm ²)	Average grain diameter (nm)
Mean	5005866.635	222.538
SD	15378254.747	16.996
Min	560035.495	184.562
Max	75440709.475	243.664

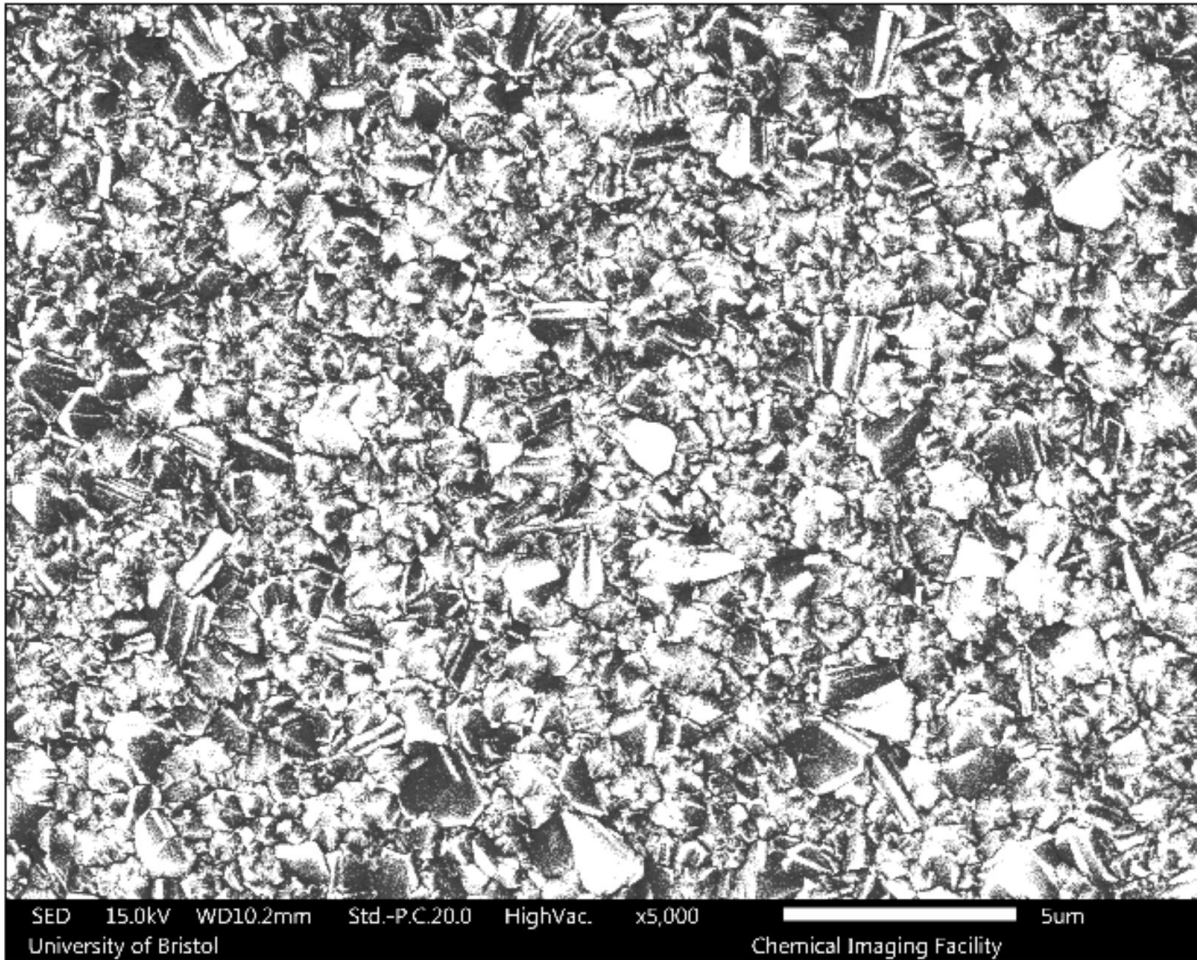


Figure 9.23: Contrast image for the grain size determination of the BDD sample.

Table 9.2: Calculated grain sizes and errors for the BDD diamond sample.

	Area (nm ²)	Average grain diameter (nm)
Mean	924.772	94.071
SD	103712.971	4.392
Min	25.022	90
Max	34864702.897	254.968

9.3.4. TECsim Spectra

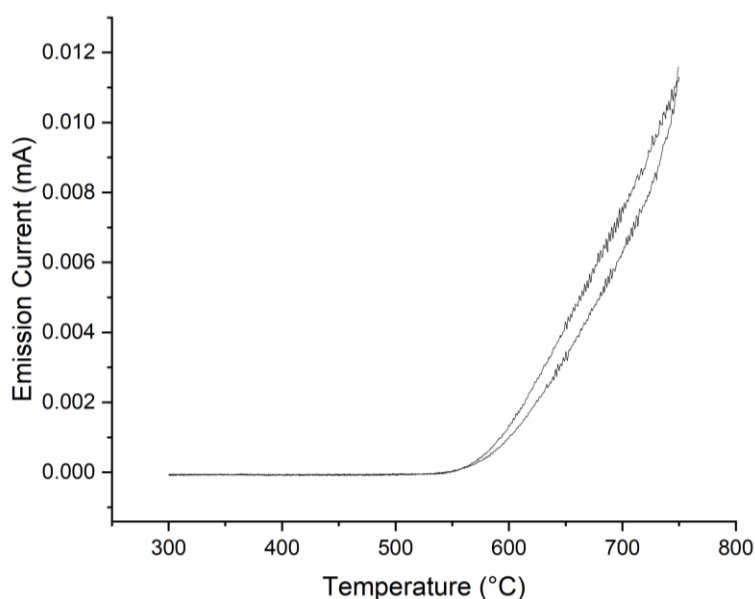


Figure 9.24: Third thermionic emission cycle between 300 – 750 °C for a PDD sample (N21134). Peak emission current of 0.012 mA at 750 °C. Threshold temperature of 525 °C. Note: only data for the third cycle were saved.

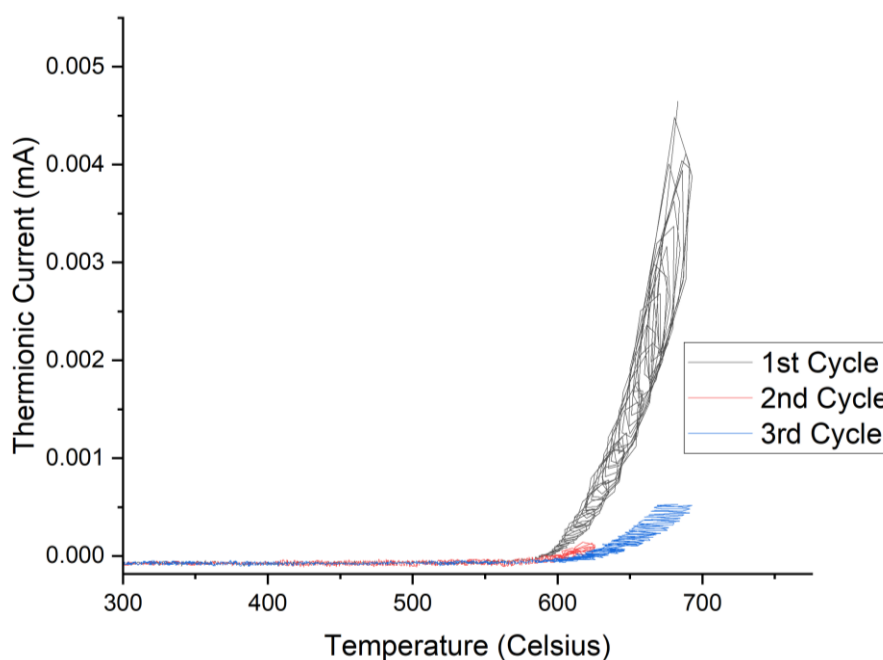


Figure 9.25: Thermionic emission cycles between 300 – 750 °C for a PDD sample (N21139). Peak emission current of 0.004 mA occurred at 660 °C prior to short-circuiting, threshold temperature measured at 570 °C for the 1st cycle. In the 2nd, peak emission current of 0.00015 mA occurred at 620 °C prior to short-circuiting, the threshold temperature was measured at 585 °C for the second cycle. Peak emission current of 0.007 mA at 680 °C prior to short-circuiting, the threshold temperature was measured at 590 °C for the third cycle. The threshold temperatures can be seen to increase for each consecutive profile.

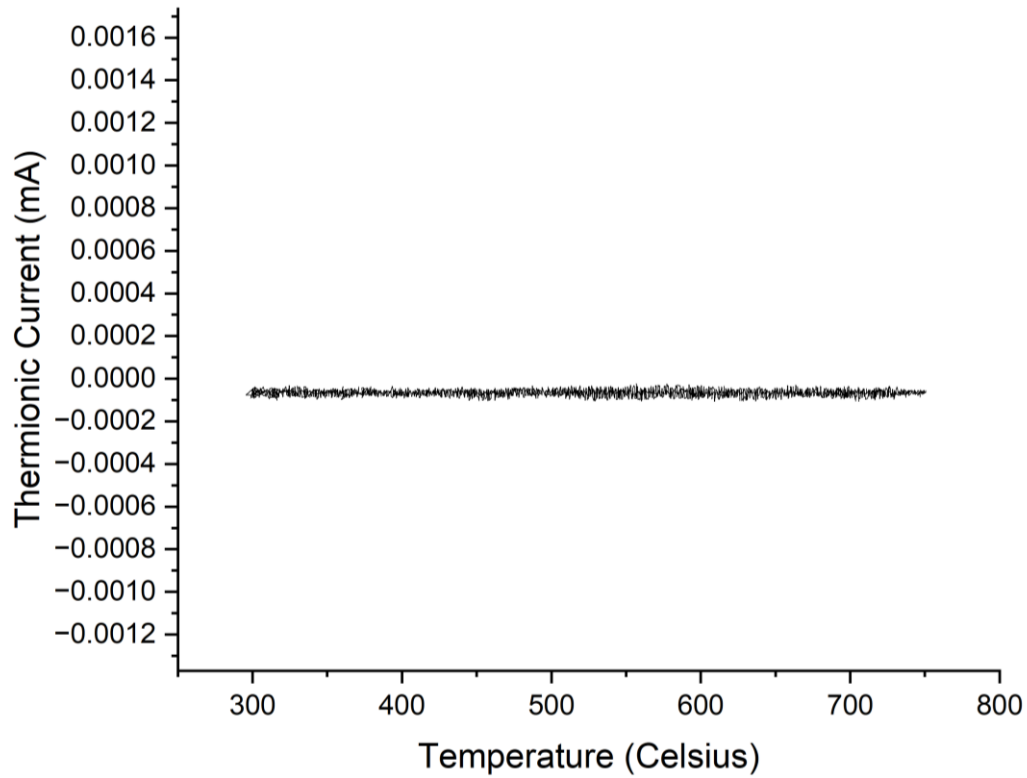


Figure 9.26: First thermionic emission cycle between 300 – 750 °C for a BDD sample (B1). No emission was observed.

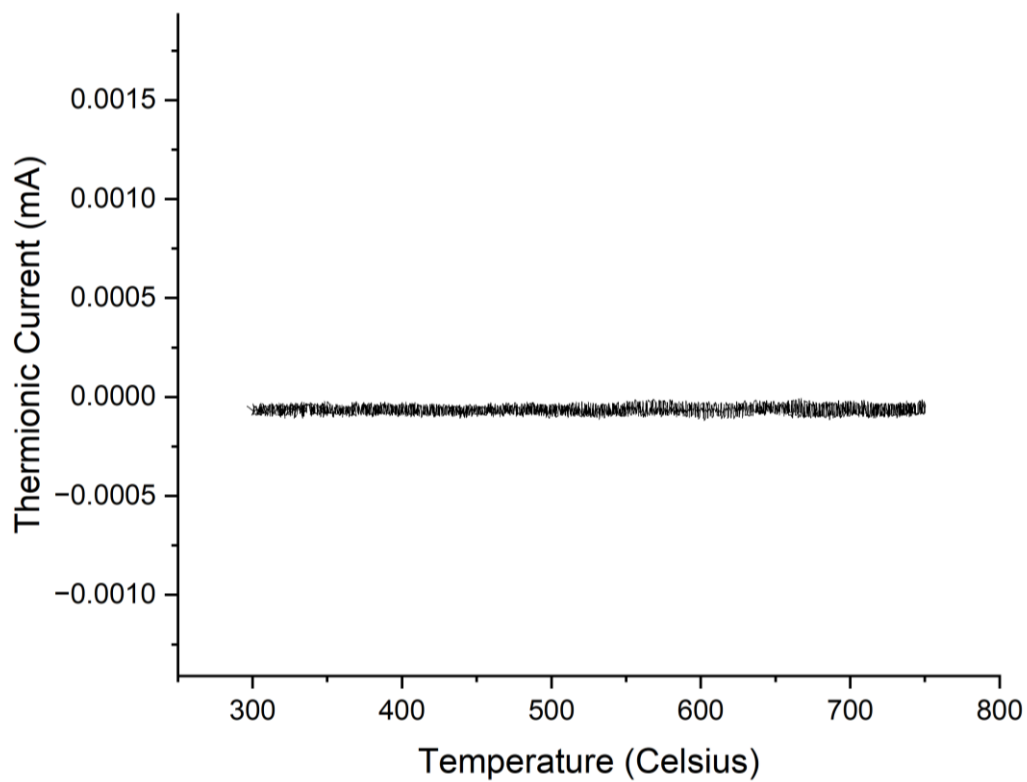


Figure 9.28: Second thermionic emission cycle between 300 – 750 °C for a BDD sample (B1). No emission was observed.